THESIS

FLOW RESISTANCE CORRECTIONS FOR PHYSICAL MODELS USING UNIT FLOWRATES

Submitted by

Cassidy B. Cote

Department of Civil and Environmental Engineering

In partial fulfillment of the requirements

For the Degree of Master of Science

Colorado State University

Fort Collins, Colorado

Spring 2024

Master's Committee:

Advisor: Christopher Thornton

Robert Ettema
Sara Rathburn

ABSTRACT

FLOW RESISTANCE CORRECTIONS FOR PHYSICAL MODELS USING UNIT FLOWRATES

Flow resistance is an essential aspect of evaluating flow behavior in open-channel hydraulic models. Flow resistance in open channels is commonly characterized by Manning's resistance equation, where a value of Manning's roughness coefficient *n*, indicates the magnitude of flow resistance. Physical hydraulic models are one method to estimate Manning's *n* values for prototype channel reaches. A physical hydraulic model evaluates prototype channel characteristics at the model scale. The scale for a given physical model may be characterized by length-scale factor, given by the relationship of prototype to model geometry.

Models that have a large length-scale factor are known to introduce errors associated with instrumentation, measurement, and scale effects, therefore minimization of the length-scale factor is an important consideration in the development of hydraulic models. Evaluating physical models using a scaled unit flowrate provides a method by which the length-scale factor may be minimized. In this way, a scaled design discharge per unit width of channel is applied to a channel that is less wide than the prototype design. Using this approach greatly improves the ability of laboratories to utilize available facilities, without being constrained by prototype design width, which can otherwise be a driving factor increasing the length-scale factor for a given model.

This thesis documents the construction and analysis of two physical models of a proposed rectangular canal along Rio Puerto Nuevo in San Juan, Puerto Rico. One model used a scaled unit flowrate and a reduced channel width at a lesser length-scale factor, and the other model accommodated the total

scaled design flowrate and design channel width at a larger-scale factor. Tests were conducted for three sidewall conditions to identify the impact associated with applying a unit flowrate physical modeling approach for models with different Manning's *n* values specific to the sidewalls.

The unit flowrate approach was found to result in larger estimates of flow depth and composite Manning's *n* compared to the model that accommodated the full prototype channel width. Insights regarding the variability of Manning's *n* as a function of channel width for each sidewall condition were identified by comparing results from the two models. A correction method was proposed for improving estimates of Manning's *n* derived from scaled unit flowrate models. Correction factors were identified as a function of two dimensionless parameters, relative prototype channel width (defined as the ratio of the width evaluated using a unit flowrate model to the design width of the channel), and relative flow resistance exerted by the individual boundary elements as determined from the unit flow rate model (defined as the ratio of Manning's *n* values between the sidewall and channel bed boundary elements).

Findings indicate that it becomes increasingly important to apply correction factors to flow resistance estimates on unit flowrate models when wall boundary elements exert a larger contribution to flow resistance than that of the channel bed (large relative roughness), and when the scaled unit flowrate approach results in a prototype channel width that is significantly smaller than the proposed design channel width (small relative channel width). Correction factors were developed for a range of relative channel width values from approximately 0.4 to 1.0, and a range of relative roughness values from approximately 0.5 to 3.0. Future physical models using unit flowrates with relative channel widths and relative flow resistance within the range evaluated may use the presented correction methods to improve estimates of flow resistance.

ACKNOWLEDGEMENTS

This research used data collected at the Colorado State University Hydraulics Laboratory for a project conducted in coordination with the U.S. Army Corps of Engineers, ATHENA Engineering-Environmental, and AECOM. The writer gratefully acknowledges the hydraulic modeling assistance given by the staff associated with Colorado State University's Hydraulics Laboratory, as well as the guidance and technical advice provided by the following engineers:

- Christopher Thornton, Ph.D., P.E.
- Robert Ettema, Ph.D., P.E.
- Jeff Ellis
- Yongqiang Lan, Ph.D., P.E.
- Dusty Barrett, P.E., P.M.P.
- Robert C. Tucker, P.E.
- Luan Esteban, P.E.

TABLE OF CONTENTS

LIST OF TABLES

LIST OF FIGURES

LIST OF SYMBOLS

Fr	Froude number, reach-averaged within the control volume
g	Gravity acceleration on earth
H_2, H_1	Total mechanical energy head at the upstream (1) or downstream (2) end of control volume
H_i	Total mechanical energy head at a given cross-section *i*
H_1^*	Energy head at the upstream end of the control volume based on the trial Manning's *n* value
L	Length
m	Subscript referring to model scale
n	Manning's roughness coefficient
n_b	Manning's roughness coefficient of the channel bed
n_c	Composite Manning's roughness coefficient of the channel cross-section
n_{exp}	The expected prototype scale Manning's roughness coefficient for percent error computation
n_i	Manning's roughness coefficient of a given channel boundary *i*
n_{obs}	The observed prototype scale Manning's roughness coefficient for percent error computation
n_w	Manning's roughness coefficient of the channel walls
P_i	Wetted perimeter for given model channel boundary *i*
P_{total}	Wetted perimeter of the entire model cross-section
p	Subscript referring to prototype scale
Q	Discharge (flowrate)
q	Unit discharge (unit flowrate), or discharge per unit width within a given cross-section
Re	Reynolds number, reach-averaged within the control volume
R_h	Hydraulic radius
r	Subscript indicating scale ratio (= prototype value/model value)
S_f	Friction slope
S_{f_1}, S_{f_2}	Friction slope at the upstream (1) or downstream (2) end of the control volume
$\overline{S_f}$	Reach-averaged friction slope within the control volume
V	Cross-section averaged flow velocity within the control volume
V_i	Average flow velocity at a given cross-section *i*
w	Channel width
w_Q	Prototype channel width applicable to the proposed channel design
w_q	Prototype channel width modeled using a scaled unit flowrate
Y	Cross-section averaged flow depth within the control volume
Y_i	Average flow depth at a given cross-section *i*
z_i	Elevation head at a given cross-section *i*
α_i	Kinetic energy correction factor at a given cross-section *i*
β	The exponent in a power relationship
Δx	Distance along channel within the control volume
δ	Percent error
Γ	Relative roughness of the channel walls to the channel bed (given by the ratio of n_w to n_b)
λ	Relative prototype channel width between the unit flowrate model and the proposed design channel width (given by the ratio of w_q to w_Q)
ϕ	Manning's conversion factor, equivalent to 1.486 for U.S. units and 1.0 for S.I units

LIST OF UNITS

cfs	cubic feet per second flowrate
ft	foot or feet
ft/s, fps	feet per second
in	inch(es)
^{o}F	Fahrenheit degree(s)
s	second

1 INTRODUCTION

1.1 Flow Resistance

Flow resistance is an essential aspect of characterizing flow behavior in open-channel hydraulic models. Flow resistance in open channels is commonly characterized by Manning's resistance equation, described in greater detail in Section 5, where a value of Manning's roughness coefficient *n*, indicates the magnitude of flow resistance. Numerical models use such characterizations, along with other analytical simplifications, to evaluate proposed channel designs, mitigate risk, provide cost-engineered solutions, and facilitate project goals. The accuracy of numerical models, however, is often reliant on an accurate estimation of flow resistance. The level of uncertainty in cross-sectionally averaged, depth-averaged, and three-dimensional numerical models can exceed 20 - 40% (e.g., Yen 2002 & Knight et al. 2018 as cited in Nikora, 2019). Physical hydraulic models developed in a laboratory setting are one method of evaluating flow resistance, thereby providing the means to calibrate and improve the accuracy of numerical models.

1.2 Physical Models of Open Channels

Physical hydraulic models are a method of obtaining insight into the complex nature of open-channel hydraulic problems. While generally more expensive than numerical modeling, physical modeling provides auxiliary advantages such as the ability to study phenomena that cannot be entirely explained by theory (Pinto, 2020). The proposed design of a given open-channel system is referred to as a prototype channel design. Physical hydraulic models evaluate prototype flow characteristics at the model scale by using concepts of similitude. Similitude provides the means to compute scale factors for which prototype channel geometry may be downsized to the selected scale of a given physical model. Subsequently, scale factors derived from similitude are then applied to flow characteristics measured within a physical model

(e.g., flow velocity), thereby providing the means to estimate flow characteristics prevailing at the prototype scale.

For the analysis described in this thesis, the dynamic scale of the physical model was based on Froude-number similitude. Froude-number similitude strives to evaluate properties at the model scale and convert them to prototype scale while keeping the model Froude-number acceptably close to that prevailing at the prototype scale. Additional details regarding Froude-number similitude are provided in Section 0.

The scale for a given physical model may be characterized by length scale ratio, given by the ratio of the model to prototype scale geometry (M:P), and length-scale factor, which is given by prototype to model scale geometry (P:M). For example, a physical model constructed at an eighth of the geometric scale as the prototype would have a length scale ratio of 1:8 and a length-scale factor of 8. Accordingly, attributes with a unit of length, such as diameter, would be an eighth of the size (smaller) in the physical model, compared to the full-scale prototype design.

1.3 Unit Flowrate

In many cases, physical models apply concepts of similitude to the design discharge Q (volumetric discharge). This thesis, however, discusses an alternate methodology in which physical models apply concepts of similitude to unit flowrate q. Unit flowrate is defined as the design discharge per unit width of channel cross-section ($q = Q/W$). Therefore, a prototype channel with flowrate Q and channel width W_Q has a unit flowrate $q = Q/W_Q$. A scaled unit flowrate is a value of q obtained from the prototype design condition and subsequently downsized (by the applicable scale factor), such that it applies to the given physical model (and the applicable length-scale factor of that model).

In laboratory settings, it can be advantageous to evaluate the hydraulic performance of a given channel using a scaled unit flowrate approach (SUFA). This approach is a tool used in physical modeling where it is desirable to evaluate hydraulic performance at a model width that is less than the corresponding width applicable to the prototype channel. In this way, a scaled flowrate per unit width of the channel is evaluated, though the model encompasses a channel width that, when scaled (by the applicable scale factor), is less than that of the proposed prototype channel design width. This approach is particularly useful for very wide prototype channels for reasons presented in Section 1.4.

Although concepts of similitude are used to ascertain the unit flowrate, SUFA models may result in an alteration of flow characteristics due to the reduction in channel width compared to the prototype channel. The body of work presented in this thesis describes one SUFA model and compares results to a second model of the same channel. The second model served as a control and used a length-scale factor that allowed the full width of a proposed prototype channel to be evaluated within the same external flume that was used for the initial model. Using the comparative results from these two models, a procedure was then developed for correcting estimates of Manning's *n* on similar physical modeling projects using SUFA. Appendix A provides a supplemental slideshow summarizing general concepts regarding unit flowrate, the limitations associated with this methodology, as well as a general comparison of results from the two models, and the flow resistance correction factors. The concepts and figures presented in Appendix A are described at length in the body of this thesis.

1.4 Motivation

Minimization of the length-scale factor results in a model that is geometrically closer in scale to that of the prototype channel and is an important consideration in the development of a physical model. Due to constraints associated with available facilities or equipment, is not always possible, however, to model

the full width of a proposed channel while simultaneously minimizing the length-scale factor such that model geometries are reasonably close to the prototype channel design. Physical hydraulic models with a large length-scale factor can also introduce errors associated with instrumentation, measurement, and scale effects.

Evaluating physical models using SUFA provides a method by which the length-scale factor may be minimized. In this way, a scaled design discharge per unit width of channel may be applied to a model that corresponds to a channel that is less wide than that of the prototype design. Using this approach greatly improves the ability of laboratories to utilize available facilities without being constrained by prototype design width, which can otherwise be a driving factor increasing the length-scale factor of a given model. The ability to minimize the length scale ratio, while not being directly constrained by the width of a given flume in a laboratory, greatly increases the flexibility of laboratories to evaluate a variety of prototype channel widths at a range of length-scale factors, which can then be optimized based on available facilities and the precision of available equipment needed in construction of physical models.

As an example, Colorado State University's Hydraulics Laboratory (CSU) has conducted numerous tests that characterize flow resistance of articulated concrete block (ACB) systems laid along the channel bed of a fixed-slope (2H:1V) steep flume with smooth walls. CSU's steep flume facility has a fixed width. Models using this facility would therefore need to employ SUFA or be directly constrained to select a length-scale factor that accommodates the flume width relative to the proposed width of a given prototype channel. Without applying SUFA to model very wide prototype channels, this could mean a length-scale factor that results in channel elements that are so small that they exceed the ability of available instrumentation used in the construction of physical models.

Models with large length-scale factors have the potential to magnify sources of instrument and measurement error. For example, a depth measurement error of 0.02 ft. at a length-scale factor of 10 would be equivalent to 0.20 ft. at the prototype scale; at a scale factor of 40, an error of this magnitude would be equivalent to 0.80 ft. at the prototype scale. Furthermore, machine accuracy limitations persist when constructing complex channel geometries for models that have large length-scale factors. One tool used in the development of model geometry at CSU is the Frogger 3D Hot-Wire Cutter, which uses a superheated wire to cut channel geometries from foam. This equipment has a kerf (radius of burn surrounding the wire) of 0.125 in. (0.0104 ft.). Therefore, within a foam element, the minimum cut width is 0.25 in. (0.0208 ft.). Using this equipment to simulate, for example, an ACB system at a length-scale factor of 40, would result in a minimum 10 in. spacing between rows of ACB at prototype scale, which may not accurately represent actual prototype conditions and could have severe implications on the accuracy of model results.

Minimization of the length-scale factor can improve constructability and reduce error magnification associated with machine precision on specific projects. Furthermore, minimizing the length-scale factor of a given Froude-scaled model can also minimize Reynolds-number scale effects associated with water viscosity on the channel's flow resistance performance, particularly in models that use water and do not vary the subject fluid viscosity to obtain Reynolds number similitude. Viscous effects and concepts of Reynolds number similitude are explored in greater detail in Section 2.1.

1.5 Scope and Objectives

A gap exists in the body of existing literature regarding rough-wall flows, Froude scaling applications, and empirical relations of flow resistance in open-channel flows. The principal objective of this research was to provide a method to correct estimates of flow resistance obtained on similar physical modeling

projects employing SUFA, such that they may be used to improve estimates of prototype Manning's *n* values applicable to the full prototype channel width. To accomplish this objective, this report documents the design, production, and analysis of two physical models used to evaluate flow resistance, one of which employed SUFA and the other which served as a control. A result comparison of these two models and their variations are presented. The case study forming the basis for the prototype channel described in this thesis consists of a proposed rectangular flood-control canal along the Rio Puerto Nuevo (RPN) in San Juan, Puerto Rico.

A SUFA model was initially developed for the RPN project, using scaled unit flowrate, though not the full-scaled design discharge. A supplemental model, at a length-scale factor that facilitated the entire prototype channel width to be accommodated (and therefore accommodating a scaled total design discharge), was then developed within the same flume, and used as a control for which the results of the SUFA model could then be compared. Model variations were conducted for three sidewall conditions to evaluate variability in flow resistance estimates using SUFA for channels with sidewalls that exert different magnitudes of flow resistance. Insights regarding the variability of Manning's *n* as a function of channel width for each sidewall condition were identified by comparing results between the two models. Flow resistance correction relationships were then developed to improve future estimates of Manning's *n* on similar physical modeling projects using SUFA.

To improve applicability of the corrections on future projects, a secondary objective of this research was establishing flow resistance correction factor relationships based on dimensionless parameters. Furthermore, investigations were conducted to evaluate the relative importance of applying correction factors for future SUFA models, using the results derived from this case study to indicate the conditions for which a given model is more or less likely to deviate from the flow resistance estimates obtained in

the control model. Prior to presenting the correction factors, some general background is needed regarding similitude concepts, used in the development and analysis of physical models, and specifics regarding the RPN project, which provided the case study project for which this research is based on.

2 SIMILTUDE

Physical hydraulic models are methods used to evaluate prototype scale flow characteristics at model scale by using concepts of similitude. An adequate comparison of the model to prototype scale is achieved when dimensionless parameters describing the geometric (form), kinematic (motion), and dynamic properties (forces) of the model are kept the same, or acceptably close, to those prevailing in the prototype (Chanson, 2004). For open-channel hydraulics, the following forces are dominant:

- Inertia force associated with the rate of change of flow momentum
- The gravitational force associated with Earth's gravity
- Viscous forces generated by water shearing

The relative magnitudes of these forces are expressed using two dimensionless numbers:

- Froude number (inertia/gravity forces)
- Reynolds number (inertia/viscous forces)

For this project, the dynamic scales of the physical models are based on Froude-number similitude. Froude similarity implies that gravitational effects are the most significant and that viscosity does not play a significant role (Pinto, 2020). Froude similitude occurs when the Froude number in the model is acceptably close to that prevailing at the prototype scale. Implications associated with potential scale effects due to viscous forces are discussed in the following section. The application of SUFA in this context, however, may result in deviations in the aspect ratio (width: depth) for a given channel reach due to the reduction in channel width compared to the prototype channel. This reduction in width may result in an increase in composite flow resistance due to a proportionally larger amount of flow in contact with

channel boundaries. These deviations resulting from application of SUFA are investigated in this thesis by comparing the results of the two physical models, as described in this report.

2.1 Viscous Effects

Scale effects are distortions introduced by scaled models due to forces (e.g., viscosity) other than the dominant one addressed by scaling (e.g., gravity). Scale effects are generally considered small, though not always negligible. If the same fluid is used in both the model and the prototype, it is not possible to keep both the Froude and Reynolds numbers the same in the model as the prototype channel. Thus, a main concern for Froude-number scaled models is the potential for scale effects due to differences in Reynolds number induced by viscous forces (Chanson, 2004).

Flow resistance characterized by Manning's equation relies on the assumption that values of Reynolds number are within the fully turbulent regime, such that values of Manning's *n* do not vary with Reynolds number. Reynolds numbers greater than approximately 4,000 are considered fully turbulent. In open channels, Reynolds numbers are often sufficiently large that the flow is fully turbulent (Sturm, 2001). However, physical models with large length-scale factors may introduce Reynolds-number scale effects if values of Reynolds number are not fully turbulent. Therefore, it can be desirable to minimize the length-scale factor such that model geometry matches as close as possible to prototype channel geometry. For Froude-scaled physical models that do not vary the subject fluid viscosity to obtain Reynolds number similitude (such as the RPN project), this measure minimizes Reynolds-number scale effects associated with water viscosity on the channel's flow resistance performance (Webb et al., 2011).

SUFA is a physical modeling method that improves the ability of a model to operate over a range of length-scale factors, thereby providing the means to facilitate the minimization of model length-scale

factors. This measure can minimize Reynolds-number scale effects for models that would otherwise result in Reynolds numbers that are not within the fully turbulent region. Minimizing a model's length-scale factor may mitigate substantial differences in Reynolds number (compared to prototype conditions) on some Froude-scaled models, particularly those that use water and do not vary the subject fluid viscosity to obtain Reynolds number similitude. SUFA is a tool that improves the ability of a model to not only minimize viscous scale effects but also improves the flexibility of a model to accommodate constraints associated with available facilities and instrumentation limitations that arise when a large length-scale factor would otherwise exceed the precision of equipment being utilized to construct a physical model.

Scale effects due to differences in Reynolds number should generally be investigated when comparing Froude-scaled models at different scale factors. While Reynolds number estimates are provided in the Section 7.1, a thorough evaluation of scale effects is well beyond the scope of this research and would require a supplemental study outside the scope of the present thesis. Considerations for a supplemental study should consider that viscosity of water in the subject RPN prototype channel at the design event may include suspended sediment, thereby increasing the viscosity of flow within the prototype channel beyond that of the water used in the RPN physical models. The estimates provided in Section 7.1 assume clear-water flow, absent of significant concentrations of suspended sediment. Evaluation of the extent and quantity of Reynolds number scale effects for physical models should be given further consideration in future research.

2.2 Flow Resistance Characterizations in Scaled Physical Hydraulic Models

There are multiple characterizations of flow resistance including Manning's n, Chezy, and Darcy-Weisbach. These coefficients represent a simplification of the combined effects, making them particularly convenient for practical applications of cross-sectionally averaged hydraulic models (Nikora, 2019).

Decompositions of the Darcy-Weisbach friction factor, however, have demonstrated that resistance encountered by flow in a channel can be split into five additive components: viscous stress, turbulent stress, dispersive stress (due to bed flow resistance and secondary currents), non-uniformity of flow (spatial heterogeneity), and flow unsteadiness (Nikora, 2019). These components account for the geometric effect of flow resistance, also termed form resistance, or form drag. The use of Manning's *n* to characterize channel resistance does not indicate explicitly the contributions from each component, because *n* inextricably mixes the components. Furthermore, the successful application of Manning's equation is dependent on sufficiently large Reynolds numbers such that values of *n* do not vary with Reynolds number (Sturm, 2001).

Dispersive stresses induced by channel geometry and resulting secondary currents play a significant role in generating flow resistance. This statement is especially true for dispersive stresses generated by transverse fluxes of momentum (Nikora, 2019). Dispersive stresses notably result from flow around the tangent walls and over the bed of regularly arrayed ACBs, as each block had individual form and gaps were present between rows of blocks. At high Reynolds numbers, dispersive stresses may play a more significant role in generating flow resistance. Turbulent stresses, however, are generally considered dominant (Nikora, 2019). Potential scale effects due to the turbulent stress component arise, therefore, in cases with a large-scale ratio, where model flow is not as turbulent as prototype flow (Chanson, 2004). This is another factor indicating that on some physical models, it can be advantageous to minimize the length-scale factor.

Many momentum-based roughness decompositions (e.g., Fukagata, et al., 2002; Peet & Sagaut, 2009; Bannier, et al. 2015; as cited in Nikora, 2019) place the primary focus on hydraulically smooth-wall flows without accounting for effects of dispersive stresses that emerge in flows at a high Reynolds

number. Tests conducted at a lesser-scale ratio, and therefore involving lesser values of Reynolds number, are expected to result in a dispersive stress component of flow resistance that should increase. However, research suggests that there may be interdependence between the contributions of the turbulent and dispersive stresses in which decreases in one stress component result in increases in the other (Nikora, 2019).

It is understood that a physical model, differing in length-scale factor and Reynolds number from the prototype, will result in alteration of the underlying stress components that drive the resulting flow resistance. The decomposition of stress components, and viscous scale effects associated with Reynolds number, however, are outside of the scope of the present study. The research presented herein specifically focuses on flow resistance estimates evaluated between the two models on the RPN project. Furthermore, all considerations in this paper characterize flow resistance as Manning's *n* due to the widely used nature in hydraulic modeling (e.g., HEC-RAS, SMS: SRH-2D), and prescribed specification specific to the subject RPN case study.

2.3 Analytical Assumptions

Various analytical assumptions were used in the implementation and analysis of this model. Most of the simplifying assumptions pertained to one-dimensional open-channel flow computations used to estimate flow resistance, characterized as Manning's *n*, as described in subsequent sections.

- The fluid was homogeneous and incompressible (constant density).
- The flow was steady in the control volume.
- The pressure distribution was hydrostatic at all cross-sections.

- Lateral and vertical flow were negligible compared to the flow component in the longitudinal direction. Energy is conserved in the longitudinal direction of flow except for losses due to flow resistance.

2.4 Geometric Similitude

A physical model of a channel's geometry is designed to be geometrically similar to prototype geometry. A summary of equations (Eq.) is provided in Appendix B. Eq. (1) describes the relationship between the characteristic scale length L, in which subscript r denotes the scale ratio for the quantity (e.g., length). The subscripts p and m refer respectively to prototype and model.

$$L_r = \frac{L_p}{L_m} \tag{1}$$

The basic requirement for dynamic similarity of free-surface flow over a fixed boundary is satisfied when the prototype and model have the same value of Froude number Fr, which expresses a balance of inertia forces relative to gravitational forces. Eq. (2) provides the relationship between model and prototype Froude number.

$$\mathrm{Fr}_m = \mathrm{Fr}_p \tag{2}$$

Eq. (3) describes how cross-section averaged values of flow velocity V, depth Y, and acceleration due to gravity g, determine Froude number.

$$\mathrm{Fr} = \frac{V}{\sqrt{gY}} \tag{3}$$

Eq. (2) and (3) lead to the scaling criteria for velocity, unit discharge $q = VY = QW$ (where W = channel width), and total discharge Q, shown by Eq. (4), Eq. (5), and Eq. (6), respectively.

$$V_r = L_r^{1/2} \tag{4}$$

$$q_r = V_r L_r = L_r^{\frac{3}{2}} \tag{5}$$

$$Q_r = q_r L_r = L_r^{\frac{5}{2}} \tag{6}$$

Eq. (7) describes how flow discharge is related to cross-section averaged values of flow velocity and depth in a rectangular channel by principles of continuity. Eq. (8) describes how flow discharge is related to flow resistance for a rectangular channel, expressed in Manning's equation. Here, $\phi = 1.49$ (U.S. customary units) or 1.0 (S.I. Units), where A = cross-sectional area of flow, $R = A/P$ = hydraulic radius of flow, n_c = the composite (effective) channel Manning's n, and S_f = friction slope, which is equivalent to the bed slope in the specific case of uniform flow.

$$Q = VA = V(Yw) \tag{7}$$

$$Q = \left(\frac{\phi}{n_c}\right) A\, R^{2/3} S_f^{1/2} = \left(\frac{\phi}{n_c}\right) (Yw) \left(\frac{Yw}{2Y+w}\right)^{2/3} S_f^{1/2} \tag{8}$$

Eq. (2), (3) and (8) lead to Eq. (9), the scaling criteria used here for the dimensional value of Manning's roughness coefficient.

$$n_r = L_r^{1/6} \tag{9}$$

Table 1 summarizes pertinent scale factors used for each of the two physical models. Results at the model scale (e.g., flow depth) can be multiplied by the applicable scale factor to obtain the associated

prototype-scale quantity. Conversely, the quotient obtained by dividing prototype-scale values (e.g., channel width) by the scale factor is the means that the scaled counterpart is obtained at the model scale.

Table 1. Scale factor summary

Parameter	**Scale Factors**	
	1:10 Length Scale Ratio	**1:24 Length Scale Ratio**
Froude number, Fr	1.00	1.00
Length, L_r	L_r = 10.0	L_r = 24.0
Velocity, V_r	$L_r^{1/2}$ = 3.16	$L_r^{1/2}$= 4.90
Total Discharge, Q_r	$L_r^{5/2} \approx$ 316	$L_r^{5/2} \approx$ 2,822
Unit Discharge, q_r	$L_r^{3/2} \approx$ 31.6	$L_r^{3/2} \approx$ 118
Manning's roughness coefficient, n_r	$L_r^{1/6}$ = 1.47	$L_r^{1/6}$= 1.70

3 RIO PUERTO NUEVO CASE STUDY

Colorado State University's Hydraulics Laboratory (CSU) in cooperation with the U.S. Army Corps of Engineers (USACE), AECOM, and ATHENA Engineering-Environmental has analyzed proposed flood control improvements the reach of the Rio Puerto Nuevo (RPN) project located in San Juan, Puerto Rico. The project reach, also known as Rio Piedras, extends approximately 5,400 ft. from the project start (18.402489, -66.064103) to the project end at (18.411903, -66.072867), as illustrated in Figure 1.

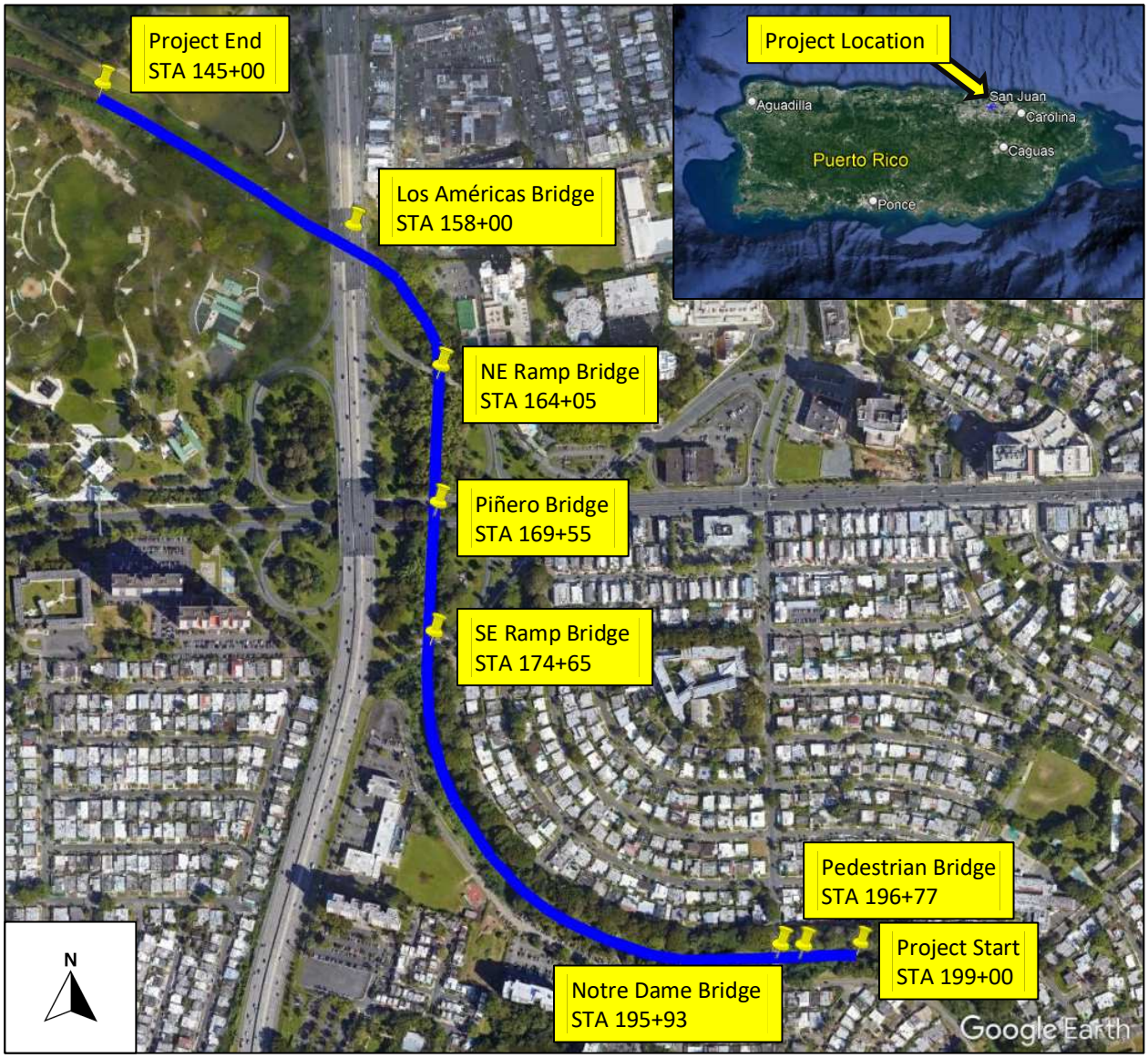

Figure 1. Project location

The primary objective of the USACE RPN project included 100-year flood hazard mitigation of areas adjacent to the Rio Puerto Nuevo floodplain and improvements to the scour resiliency of the channel bed. These objectives were proposed to be met by a prototype concrete-lined rectangular channel with ample flood-flowrate capacity and scour resiliency. CSU developed physical models to evaluate Manning's *n* values for the composite channel and sidewalls to facilitate numerical model calibration and assess channel bed lining alternatives that best satisfied the design criteria specified by USACE. The results of this case study form the basis for the research presented in this thesis.

The watershed for the project reach comprises approximately twenty-four square miles of predominantly urban area that drains into San Juan Bay, San Juan, Puerto Rico. The RPN basin is approximately 75% developed and encompasses a population of 250,000 (USACE, 2023). The existing reach is primarily a natural vegetated system with numerous bridge crossings. The area has a history of issues associated with rapid runoff and insufficient channel capacity, resulting in intense flooding in the highly developed floodplain, which is populated by over 3 billion dollars in public and commercial infrastructure and approximately 7,500 residents (Deya, 2022). USACE awarded an 8.75 million dollar dredging contract in 2019 to remove 240,000 cubic yards of material from the RPN channel that accumulated following Hurricane Maria (Carrasco, 2019).

USACE RPN flood-control work will provide 100-year flood hazard mitigation and over 125 million in average annual economic benefits to the surrounding area (Deya, 2022). The RPN project encompasses improvements to 11.2 miles of river corridor, including 1.7 miles of concrete-lined trapezoidal channel, 9.5 miles of concrete-lined rectangular channel, and 2,160 ft. of double-box culverts (USACE, 2022). The overall RPN project includes six segments that will be constructed by 2032 (Deya, 2022). CSU's involvement consisted of a portion of the project (one of six of the overall USACE RPN project segments),

shown in Figure 1 herein referred to as the project reach, which comprised a proposed 5,400 ft. concrete-lined rectangular channel.

Termination of the project reach (STA 145+00) was approximately 2.6 miles from the mouth of the RPN and San Juan Bay. Due to the proximity to the ocean and the low elevation of the proposed channel bed to mean sea level, a 100-year flood event in this area could be coupled with a storm surge. This pairing could alter the flow regime, resulting in a non-uniform, backwater flow condition in the project reach. Under the direction of USACE, physical modeling was performed for a design condition occurring under a free-flowing, 100-year return period event, independent of a backwater condition, to isolate the effects of proposed channel linings on flow resistance.

The RPN project employed hybrid modeling consisting of a Flow-3D numerical computational fluid dynamic model (CFD), developed by AECOM, to evaluate the reach-scale hydraulic performance of the proposed channel. This model was calibrated using estimates of flow resistance derived from the physical models presented in this thesis. An analysis of reach-scale channel geometry (including fluctuations in width and bends in the alignment) and a sensitivity analysis of boundary conditions (e.g., backwater due to storm surge) were completed using the numerical model as an effort outside of the scope of analysis. The focus of this thesis specifically pertains to the construction, testing, and analysis of the two physical models, and the development of a new procedure for correcting estimates of Manning's *n* on future physical models using SUFA, based on the comparative results from these two models.

3.1 Proposed Channel Design

USACE provided the proposed RPN channel reach design for evaluation. The proposed design included the installation of a concrete-lined rectangular channel at a specified gradient of 0.24%. The design required subcritical flow (Froude number < 1) at the 100-year design event to mitigate concerns associated with excessive channel bed shear stresses and energy dissipation. Construction of the proposed channel was specified as occurring either entirely or partially during low-flow conditions (USACE, 2022). Proposed channel widths vary from 95 ft. to 150 ft. within the project reach to accommodate constraints imposed by existing infrastructure, however, a design width of 120 ft. was specified to be used as the design condition for the present study.

3.1.1 Side Walls

Dimensions and composition of the sidewalls of the rectangular channel were predetermined by USACE and modifications were not investigated in the present study. Proposed channel sidewalls were specified as concrete drilled shafts, herein termed tangent walls. After construction, the proposed tangent walls created a continuous boundary of vertical cylinders, each with a 6.0 ft. in diameter, along both sides of the proposed project reach, an example of which is pictured in Figure 2 (USACE, 2022). This wall configuration presented a hydraulically rough boundary condition that resulted in an unknown flow-resistance behavior.

Figure 2. Drilled shaft tangent walls

3.1.2 Scour Protection Systems

The prescribed channel design specifies that a scour protection system (SPS) be installed across the full width of the channel bed along the proposed RPN project reach. The focus of this research pertains to SPS consisting of articulated concrete blocks (ACB). Consequently, the combination of the ACB SPS and the proposed tangent walls resulted in an unknown flow resistance behavior, and therefore required investigation, as this thesis describes. Available SPS options are limited by the significance of in-situ groundwater pressures and installation constraints. Gabions, reno-mattresses, high-performance turf reinforcement mats, impermeable liners, and ACB were evaluated as potential SPS by the design team. ACBs were identified as the most viable option for the RPN project due to considerations of pore pressure, the prevalence of wet conditions during installation, and the fact that ACB performance does not rely on vegetation within the channel bed for stability.

CSU's Hydraulics Laboratory has experience conducting tests on ACB SPS. Historical testing results were consulted to ascertain potential ACB SPS candidates for the RPN project. There is a distinction between two industry-standard manufacturing techniques of ACB blocks: a wet-cast unit and a dry-cast

unit, as shown in Figure 3 (NECA, 2023) and Figure 4 (Contech, 2023), respectively. Previous performance testing has shown that in supercritical flow on a slope of 2H:1V (Horizontal: Vertical), the wet-cast ACB SPS had a higher value of Manning's *n* than the dry-cast ACB SPS. Test data indicates that the wet-cast ACB SPS resulted in a Manning's *n* value of 0.039 for the 15.5 x 15.5 x 4.5 in. (length x width x depth) block size and a Manning's *n* value of 0.041 for the 15.5 x 15.5 x 5.5 in. block size (Morgan, 1999). Analysis of test data for the dry-cast ACB SPS resulted in a Manning's *n* value of 0.029 for the 17.4 x 15.6 x 4.6 in. block size (Thornton, 2018). These data, however, are representative of a supercritical steep slope condition and may not be indicative of the subcritical mild slope condition of the proposed RPN channel. The present study investigated the wet-cast ACB SPS in subcritical mild slope conditions applicable to RPN.

Figure 3. Wet-cast ACB SPS

Figure 4. Dry-cast ACB SPS

3.2 Objectives and Scope

The primary objective of the RPN study was selection of an SPS that met project constraints. An acceptable SPS was specified as one that facilitated the target hydraulic characteristics intended to mitigate adverse conditions such as floodplain inundation, supercritical flow, excessive shear stress, and strong secondary currents. A supplemental objective of the study was to isolate the hydraulic resistance specific to the selected SPS. This information was used in the calibration of the CFD numerical model developed by AECOM for further analysis of flow conditions along the proposed RPN project reach. Ensuing sections describe the means and methods used to evaluate the hydraulic performance of the proposed RPN channel, equipped with the wet-cast ACB SPS candidate, within the constraints of the proposed layout and design criteria. The design criterion detailed in the subsequent section pertains to the composite flow characteristics of the proposed 120 ft. wide design channel cross-section, which included both the SPS and the tangent wall channel linings and geometry along the project reach.

3.3 Design Criteria

Hydrologic and hydraulic modeling of the project reach were conducted by USACE before the present study. Based on these results, a 100-year recurrence design discharge of 29,300 cfs was provided. A 100-year recurrence is equivalent to a 1% annual exceedance probability (AEP). A design discharge of this magnitude was specified for the entire project reach, with no lateral inflow or outflow under consideration. Under these conditions, Table 2 summarizes the design criteria for the project reach, provided by USACE with the intent that the selected SPS provide sufficient roughness to mitigate supercritical flow, reduce secondary currents, and reduce shear stress along the channel bed.

Table 2. RPN design criteria

Applicability	Design Frequency	Design Criteria
Flow Resistance	100-year	Target value of composite Manning's *n:* 0.025 $\leq$ $n_c \leq$ 0.030
		Maximum value of composite Manning's *n:* $n_c \leq$ 0.035
Flow Regime	100-year	Flow remains stably subcritical along the channel
		Target Froude number[a], $\mathrm{Fr} \leq 0.80$
		Maximum Froude number, $\mathrm{Fr} \leq 0.85$
Bridge Capacity	100-year	Minimum 2.0 ft. of freeboard at the design discharge
		Target 3.0 ft. of freeboard at the design discharge
Scour Protection System	100-year	Stable at the design discharge
	Low-flow condition	Constructable in a wet low-flow condition

[a] For a cross-section, $\mathrm{Fr} = V/(gY)^{0.5}$, where V = average velocity and Y = average flow depth

Additional details about individual criteria elements were as follows:

1. Thresholds for channel roughness (flow resistance) were characterized in terms of Manning's *n* roughness coefficient values. A target effective (composite) Manning's *n* (n_c) in the range of 0.025 – 0.030 was specified. The maximum allowable value of n_c was 0.035.

    - Minimum n_c was specified to maintain subcritical flow through the project reach and achieve the target Froude number performance, described below in further detail.
    - Maximum n_c was specified to mitigate inundation of the channel's floodplain and facilitate minimum freeboard at bridge crossings, described in greater detail below.
    - Composite roughness of the proposed channel involved roughness contributions from both the tangent walls and the selected SPS. Alteration of the tangent wall geometry was not a consideration in this analysis. The primary objective was selecting an SPS that, in conjunction with the prescribed sidewalls, provided an acceptable value of n_c.

2. Criteria specified that the flow regime within the project reach remained stably subcritical to mitigate scour and reduce shear stress in the channel bed. In terms of Froude number, Fr, a target $\mathrm{Fr} < 0.80$ was specified at the 100-year design discharge. Based on USACE modeling, to achieve the target performance for Fr, it was further specified that $n_c \geq 0.025$.

3. A minimum of 2 ft. of freeboard was specified for all channel-spanning bridge crossings. A target freeboard of 3 ft. was specified for all such crossings. To achieve the minimum freeboard, it was specified that $n_c \leq 0.035$.

4. It was also specified that the selected SPS be stable at the design flow and constructable in wet (low-flow) conditions within the excavated channel. Investigations regarding constructability and stability of the SPS however, were not a matter of investigation within the present study.

3.4 Flowrates

Model-scale geometry and corresponding discharges (flowrates) were determined by applying Froude similitude to the proposed prototype channel characteristics, as specified in Table 1. A 100-year recurrence (1% AEP) design discharge of 29,300 cfs is applicable for the entire project reach with no lateral inflows or outflows. For the 120 ft. width of the channel, similitude resulted in a prototype channel unit flowrate of approximately 244 cfs per foot of prototype width ($q = Q/W$ = 29,300 cfs / 120 ft.) for the 100-year event. Recall that this study used two model length scale ratios, 1:10 and 1:24. Table 3 gives the model- and prototype-scaled discharges used in the evaluation of each model. The scaling criteria for q and Q are provided by Eq. (5) and (6), respectively. The 100-year unit flowrate (244 cfs/ft) is modeled for System A and B (1:10 scale) at a flowrate Q_m = 38.60 cfs and for System C and D (1:24 scale) at a flowrate of Q_m = 10.38 cfs.

Table 3. Model and prototype flowrates

Length Scale Ratio (M:P)	Model		Prototype	
	Q_m (cfs)	q_m (cfs/ft)	Q_p (cfs)	q_p (cfs/ft)
1:10	38.60 [a]	7.72 [a]	12,206 [a]	244 [a]
	32.50	6.50	10,277	206
	27.75	5.55	8,775	176
	18.50	3.70	5,850	117
	9.25	1.85	2,925	59
1:24	17.50	3.50	49,382	412
	15.60	3.12	44,020	367
	13.37	2.67	37,728	314
	10.38 [a]	2.08 [a]	29,290 [a]	244 [a]
	8.91	1.78	25,142	210
	5.19	1.04	14,645	122

[a] Corresponding to the 100-year design discharge applicable to the RPN case study project

4 METHODS

Physical models for the present study were conducted at CSU's Hydraulics Laboratory, with facilities at the Engineering Research Center in Fort Collins, Colorado. Two physical hydraulic models were built at two different length scale ratios: 1:10 and 1:24 (model to prototype). These models were used to evaluate the flow resistance of the composite channel, as well as the individual contributions of the proposed tangent walls and SPS. A length-scale factor of 10 or smaller was initially requested to model a 120-ft wide prototype channel. Available facilities at that time, however, were limited to a 6-ft. flume (not including further reductions to width by the assembled model walls). Therefore, an alternate approach was needed to deliver the project at the length-scale factor requested by the project partners.

To capitalize on available facilities and minimize potential scale effects and error magnification, physical modeling of the RPN project was initially conducted at a length scale ratio of 1:10 using SUFA. Upon review of initial results, however, it was surmised that the application of SUFA, which resulted in a prototype channel width less than the full design width, could have resulted in a non-negligible impact on the resulting flow resistance characterization, particularly given the unique geometry of the channel walls which were found to exert significant flow resistance. To investigate this hypothesis, a supplemental model was then conducted at a length scale ratio of 1:24 to accommodate the full prototype channel width within the 5 ft. wide assembled model. Model tests were conducted for three sidewall conditions to investigate the implications associated with SUFA for varying amounts of boundary element flow resistance. Using comparative results from these two models and their variations, this thesis presents a procedure to correct estimates of flow resistance on future SUFA models. A detailed comparison of the two RPN physical models and their variations are provided in the following sections.

4.1 Flume Layout and Dimensions

An existing flume, 6.0 ft. wide, 3.0 ft. deep, by 40.0 ft. long, housed the physical models. The flume was modified to include steel runners and toggle clamps to hold the walls in place and counteract buoyancy. Figure 5 shows the flume during modification and after modifications were complete.

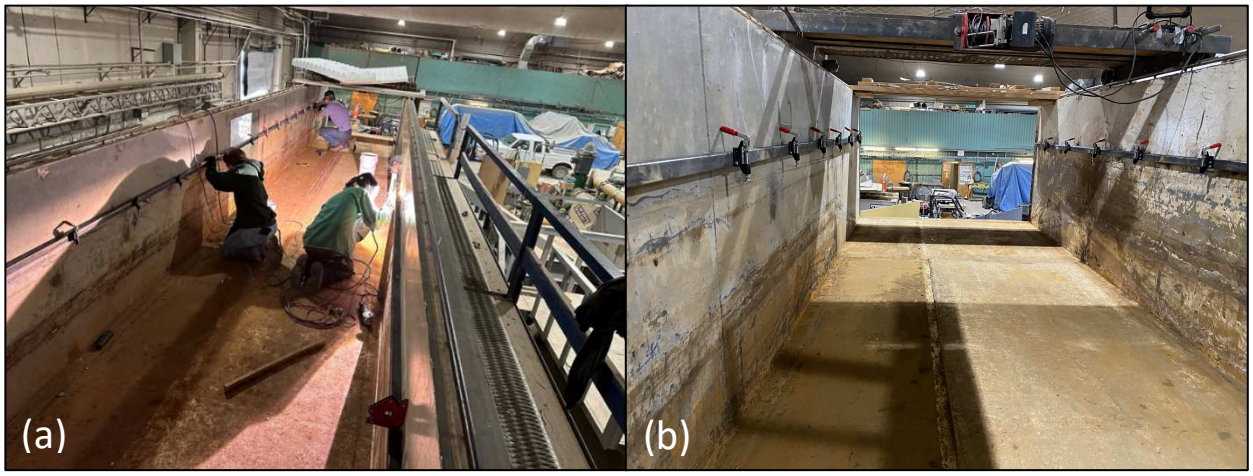

Figure 5. Photographs of CSU's 6-foot-wide flume: (a) during modification; and (b) after modification

4.2 System Descriptions

The test program involved a series of combinations of channel boundary elements for each of the two model scales. Channel bed composition (smooth, ACB) were combined with wall configurations (smooth, mixed, tangent) at two model length scale ratios (1:10, 1:24). As Table 4 indicates, a letter (A to D) was assigned to each combination of bed composition and length scale ratio. This combination is herein referred to simply as a system, with more detailed descriptions (e.g., System B) defined in Table 4.

Table 4. System descriptions

System	Length Scale Ratio (M:P)	Channel Bed Condition	Prototype Channel Width (ft.)	Note
A	1:10	Smooth	50	Used for calibration of System B
B	1:10	ACB SPS	50	Proposed design condition with width limitation
C	1:24	Smooth	120	Used for calibration of System D
D	1:24	ACB SPS	120	Proposed design condition at full design width

Each wall insert was 0.5 ft. wide, which resulted in a 5.0 ft. model width in the 6.0 ft. wide flume. Each system was evaluated using three wall configurations (smooth, mixed, tangent) over a series of flowrates. The smooth configuration indicates a test in which both the walls on LTC (channel left) and RTC (channel right) had the smooth wall side exposed to flow. A mixed configuration indicates a test in which the LTC had a smooth wall and RTC had a tangent wall exposed to flow. A tangent wall configuration indicates a test in which both the LTC and RTC sidewalls were set with tangent walls exposed to the flow, Figure 6 (a) and Figure 6 (b) give examples of the smooth wall configuration for System A and B, respectively. Figure 7 (a) presents the mixed wall configuration of System C. Figure 7 (b) presents the tangent wall configuration of System D. Additional photographs of each system and wall combination are provided in Appendix C.

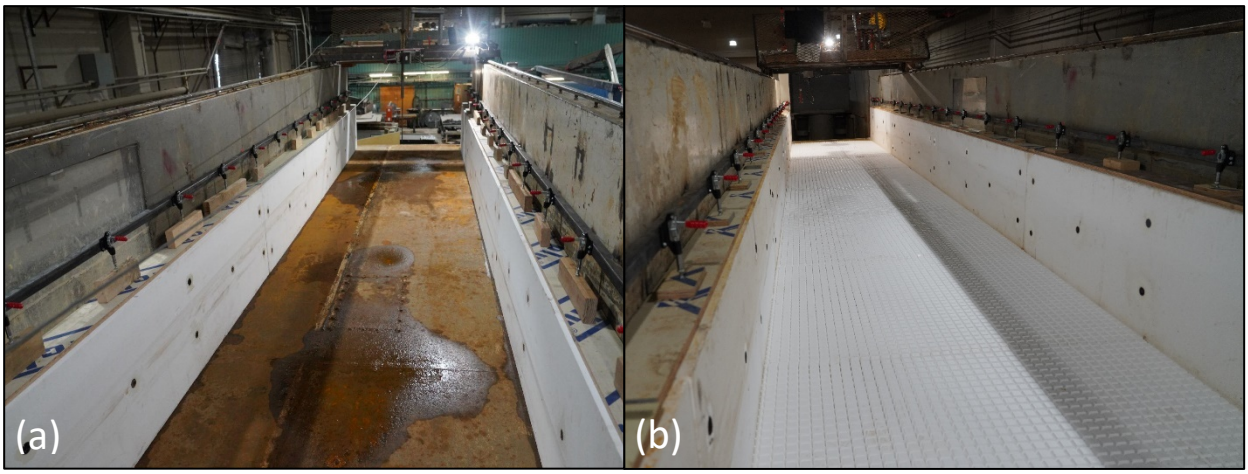

Figure 6. 1:10 scale model with smooth wall configuration: (a) System A; and (b) System B

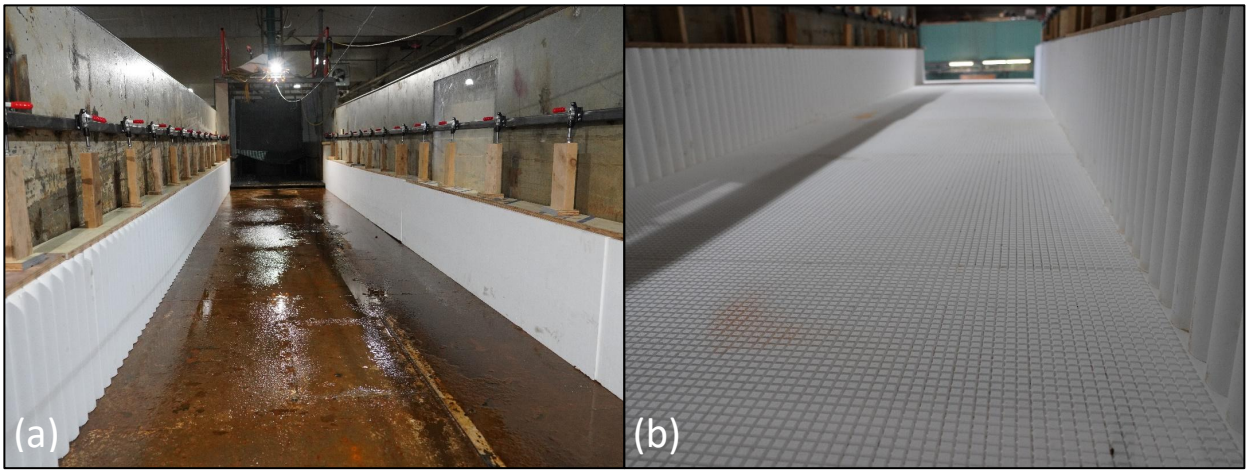

Figure 7. 1:24 scale model: (a) System C with mixed walls; and (b) System D with tangent walls

4.3 Program of Tests

Tests conducted for the 1:10 model (Systems A and B) were evaluated over five flowrates for each of the three wall configurations, resulting in a total of 15 tests per system. A summary of the test program for the 1:10 scale models is provided in Table 5.

Table 5. Program of tests for the 1:10 scale model

Flowrate (cfs)	System A			System B		
	Smooth Walls	Mixed Walls	Tangent Walls	Smooth Walls	Mixed Walls	Tangent Walls
38.6 [a]	1	6	11	16	21	26
32.5	2	7	12	17	22	27
27.8	3	8	13	18	23	28
18.5	4	9	14	19	24	29
9.3	5	10	15	20	25	30

[a] Corresponding to the 100-year design discharge applicable to the RPN case study project.

Tests conducted for the 1:24 scale model (Systems C and D) were evaluated at six flowrates for each of the three wall configurations, resulting in a total of 18 tests per system. A summary of the test program for the 1:10 scale models is provided in Table 6. Including both physical models, a total of 66 tests were conducted.

Table 6. Program of tests for the 1:24 scale model

Flowrate (cfs)	System C			System D		
	Smooth Walls	Mixed Walls	Tangent Walls	Smooth Walls	Mixed Walls	Tangent Walls
17.5	31	37	43	49	55	61
15.6	32	38	44	50	56	62
13.4	33	39	45	51	57	63
10.4 [a]	34	40	46	52	58	64
8.9	35	41	47	53	59	65
5.2	36	42	48	54	60	66

[a] Corresponding to the 100-year design discharge applicable to the RPN case study project

4.4 Model Production

Model SPS and tangent walls were manufactured with high-density foam using a Frog3D hot wire cutter. Figure 8 displays the hot-wire cutter that was used to produce the model scale ACB SPS from large foam blocks. The ACB SPS was scaled at appropriate dimensions to simulate an 8.5 in. wet-cast ACB SPS mattress. A 4-foot-long, 5-foot-wide section of the model ACB SPS is shown in Figure 9 (a). Each section was glued to interlocking wooden floorboards for ease of installation in the 40 ft. long flume. The glued sections of the model ACB SPS are pictured in Figure 9 (b).

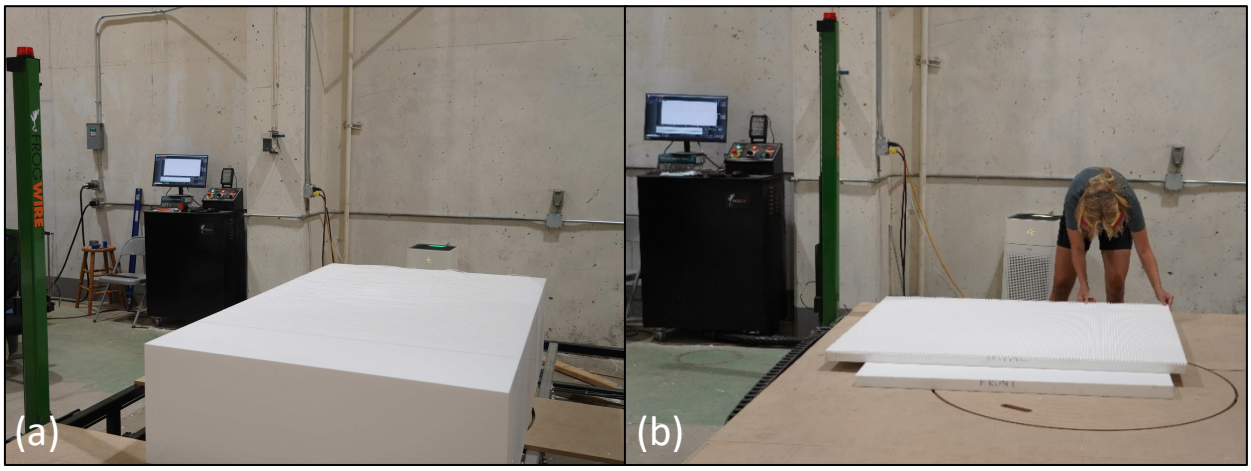

Figure 8. Production of model ACB SPS: (a) at initiation; and (b) mid-production

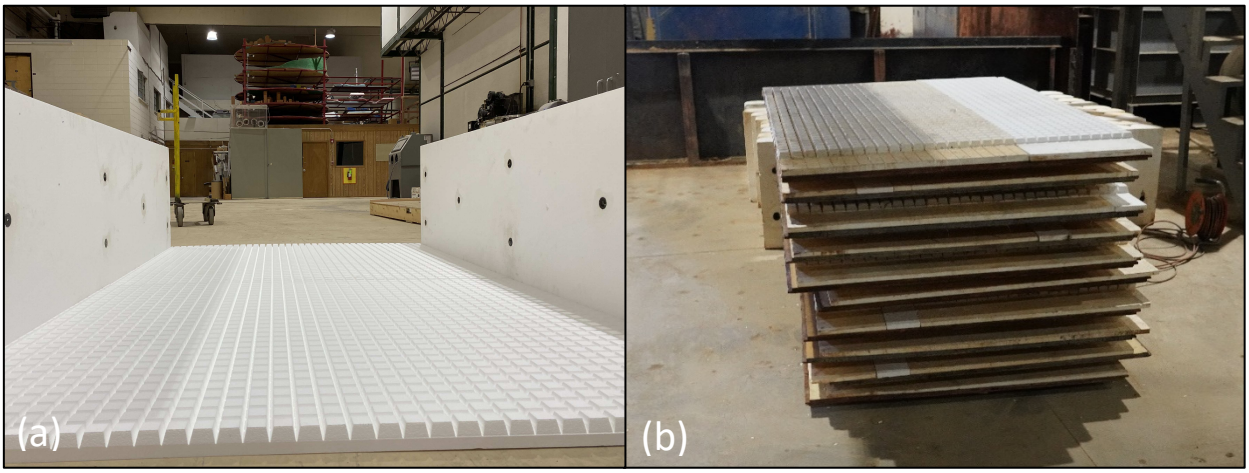

Figure 9. Views of the model SPS: (a) ACB with smooth walls; and (b) ACB glued to floorboards

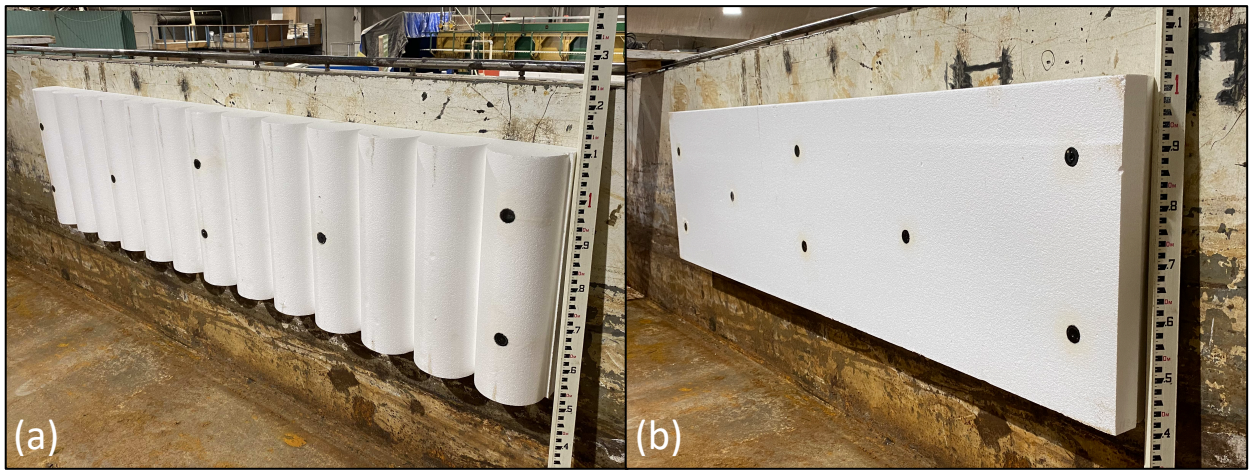

Figure 10. 1:10 scale model walls: (a) tangent walls; and (b) smooth walls on reverse side

Reversible walls were constructed for the physical models. Tangent wall geometry was cut on one face, shown in Figure 10 (a), and a smooth flat profile was cut on the opposite face, shown in Figure 10 (b). The 6.0 ft. prototype tangent wall diameter was scaled to 0.6 ft. (7.2 in.) to meet the length dimensions of the 1:10 scale model, and to 0.25 ft. (0.3 in.) to meet the length dimensions of the 1:24 scale model. Magnets were used in the 1:10 scale model walls to ensure that the walls remained stationary against the flume's steel boundary. However, clamps proved sufficient for this purpose, and the magnets were not used to counteract the buoyancy of the walls in the secondary 1:24 scale model.

4.5 Boundary Conditions

Figure 11 shows the boundary conditions that were present at each end of the physical model. Water entered the model through the headbox, as seen at the end of Figure 11 (a). The headbox was equipped with a diffuser to mitigate wave formation and undue flow dissipate energy. The downstream end (outlet) of the physical model consisted of a free outfall, shown in Figure 11 (b). The flume length (40 ft.) was not sufficiently long to establish uniform flow, therefore non-uniform gradually varied flow equations were used to characterize flow behavior, described in greater detail in Section 5.

Figure 11. Views of the model boundary conditions: (a) flume inlet; and (b) flume outlet

4.6 Measurements and Instrumentation

Water sourced to the model originated from the Horsetooth Reservoir and was at a temperature of approximately 47°F through the tests. Water temperatures were considered constant for each model. Water properties of significance (density and kinematic viscosity) were considered inconsequentially different than those pertaining to flows in the prototype channel. Measurements of lengths, flowrates, velocities, and flow depths were made using an extensive set of instrumentation for laboratory testing. Included were ADV velocimeters, various water-level and depth gauges, and flowrate meters. Discharges to the model were measured using an Endress + Hauser Promag L400 electromagnetic flowrate meter installed in the pipe supplying water to the headbox of the model. This flowrate meter was factory calibrated and had a maximum measurement error for discharge of ±0.2% of the reading quantity.

Water-surface elevations were measured using a point gauge. Measurement precision of the standard point gauge was $\pm 1.0 \times 10^{-3}$ in. with the gauge's major divisions set at 0.01 ft. increments. Velocity data for select tests were collected using an Acoustic-Doppler Velocimeter (Nortek Vectrino-Plus), whose

measurement precision was ±0.1% of the set reading. This instrument can be used for velocities less than 13.0 fps with a resolution of 0.0003 fps. ADV measurements reflect the velocity captured at 60% of the depth from the top of the water column as an approximate representation of the depth-averaged velocity. However, cross-section averaged velocity, computed using a continuity relationship ($Q = VA$), was used in the evaluation of flow resistance, discussed in greater detail in subsequent sections. Velocity estimates using both methods are provided in Appendix D.

4.7 Test Procedure

The flume was configured with Station 0 (STA 0) at the upstream end of the model, and STA 40 at the downstream end. Data were collected using the systematic grid illustrated in Figure 13. Five measurements were taken at each cross-section in which data were captured. Water-surface elevations (WSE) were collected every 5.0 ft. starting at STA 1, shown in Figure 13 in both red and blue. For Velocimeter tests, velocity was collected every 10.0 ft. starting at STA 11, shown in blue. WSE data were collected using a point gauge. Figure 12 (a) presents WSE data collection during testing. Figure 12 (b) presents bed elevation data collection. A local datum was used for the evaluation of elevations, such that the flume bed surface at STA 35 (the end location data were captured) was set to a 100.0 ft. elevation.

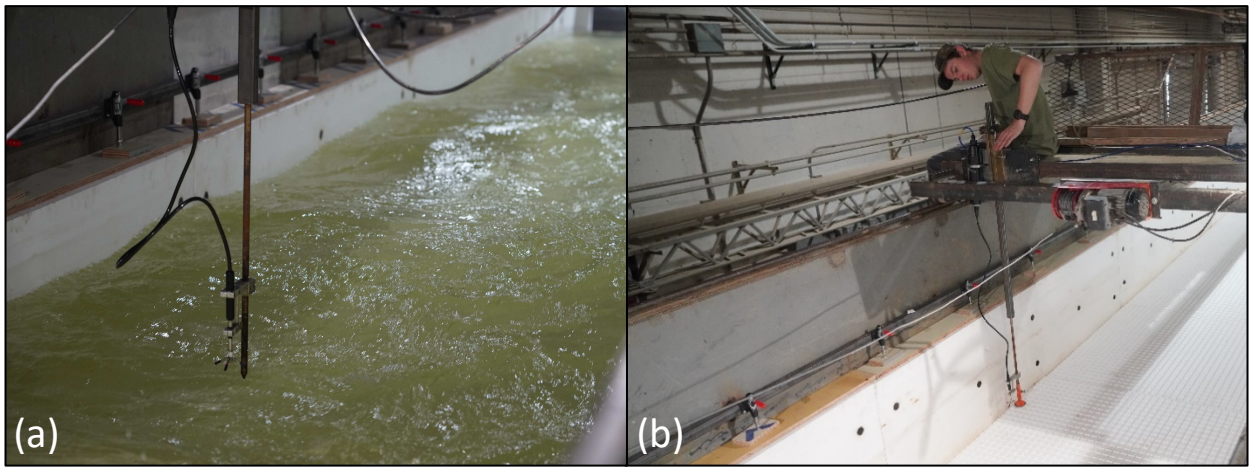

Figure 12. Data collection techniques: (a) during testing; and (b) prior to testing

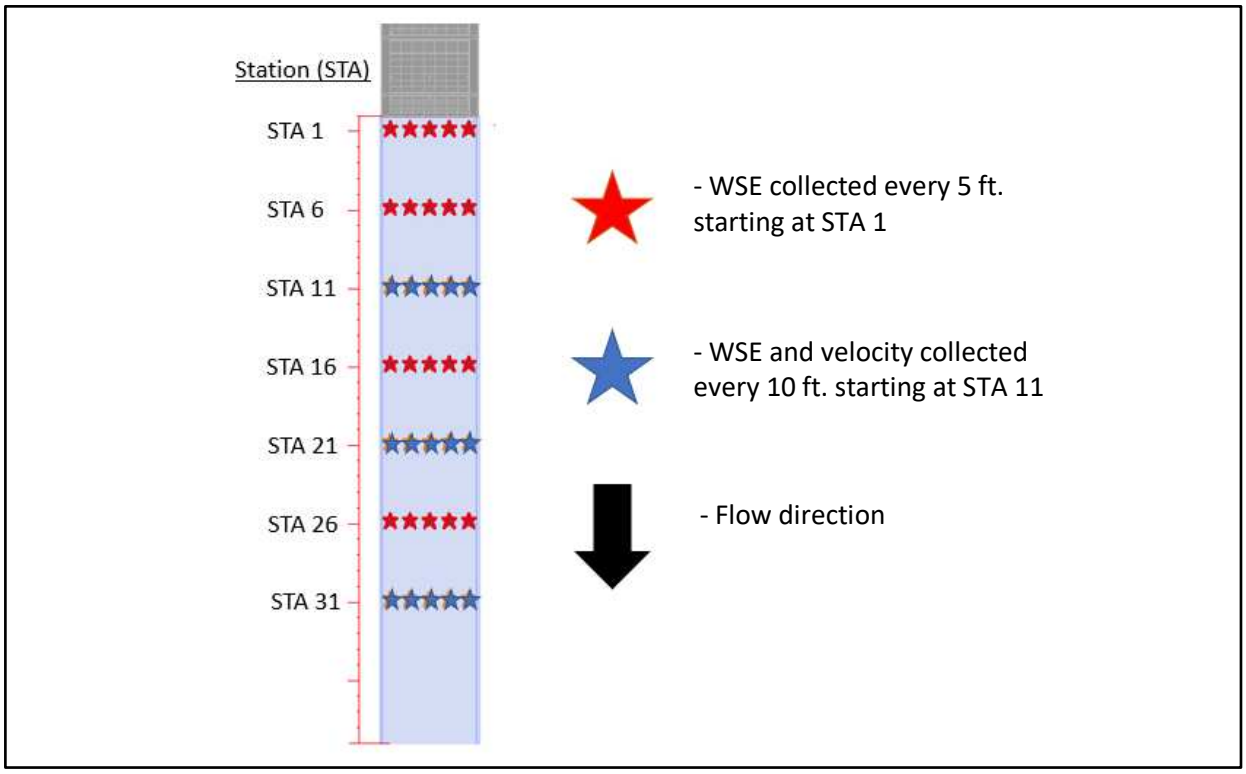

Figure 13. Data collection locations

5 ANALYSIS

Observed water-surface profiles are provided in Appendix E for each of the sixty-six tests performed. A control volume from STA 16 to STA 21 (near the STA 20 center of the flume), was selected for analysis. Linear trendlines were fitted to the observed data to obtain a representative water-surface slope through the selected control volume. Values for the reach-averaged flow depth Y within the control volume were obtained by using an arithmetic average as shown in Eq. (10). Values for the reach-averaged flow velocity V within the control volume, were obtained by applying Eq. (7) at flow depth Y. Reach-averaged Froude number Fr, was computed by combining Eq. (3), (7), and (10) to produce Eq. (11), applicable to the rectangular cross-section modeled. Eq. (12) presents a rearrangement of Manning's equation to solve for n_c, the composite Manning's *n* of the channel.

$$Y = \frac{Y_1 + Y_2}{2} \tag{10}$$

$$\mathrm{Fr} = \frac{V}{\sqrt{gY}} = \frac{Q/(Yw)}{\sqrt{gY}} = \frac{Q}{Y^{1.5} w \sqrt{g}} \tag{11}$$

$$n_c = \frac{\phi}{V} R_h^{2/3} S_f^{1/2} = \frac{\phi}{Q/(Yw)} \left(\frac{Yw}{2Y+w}\right)^{2/3} S_f^{1/2} \tag{12}$$

In the case of steady uniform flow, the friction slope, S_f, is equivalent to the bed slope. However, due to a short flume length (40.0 ft.), flow uniformity was not obtained within the control volume, such that values of S_f had to be assessed using a rearrangement of Manning's equation, as shown by Eq. (13). Estimates of cross-section averaged velocity V were estimated using Eq. (7). Hydraulic radius R_h was evaluated using the average flow depth measured for a given cross-section.

$$S_f = \frac{V^2 n_c^2}{\phi^2 R_h^{4/3}} \tag{13}$$

The reach-averaged value of S_f within the control volume, $\overline{S_f}$, was computed using an arithmetic average as shown in Eq. (14). The subscripts 1 and 2 correspond to the cross-sections STA 16 and STA 21, located at the upstream and downstream ends of the control volume, respectively.

$$\overline{S_f} = \frac{S_{f_1} + S_{f_2}}{2} \tag{14}$$

The total mechanical energy head at a given cross-section was approximated as the sum of the elevation head z_i, pressure head (or flow depth) Y_i, and velocity head, as given in Eq. (15). The kinetic energy correction factor α in Eq. (15) was approximated as 1.0 within the control volume.

$$H_i = z_i + Y_i + \frac{\alpha_i {V_i}^2}{2g} \tag{15}$$

Subcritical, non-uniform, steady gradually varied flow in the control volume was analyzed using the standard-step method. The total mechanical energy head at both ends of the control volume were first computed, using flow depth determined from observation trendlines. A trial value of Manning's *n* was then used to compute $\overline{S_f}$, which was inserted into Eq. (16), which describes H_1^*, the energy head at the upstream end of the control volume based on the trial value of *n* and the associated value of $\overline{S_f}$.

$$H_1^* = H_2 + \overline{S_f}\Delta x \tag{16}$$

The trial value of *n* became the solution for the roughness coefficient determined for the control volume when $H_1^* = H_1$. The solver function in Excel enabled an objective to be specified such that the cell containing H_1^* was set equivalent to H_1. This was accomplished by changing the trial roughness coefficient in the variable cell until a solution converged, thereby simultaneously satisfying Eq. (14), (15), and (16).

6 RESULTS

Measurements of water-surface elevations are provided graphically in Appendix E. These data include water-surface profiles and sample cross-section figures for each system-wall combination evaluated. Representative trendlines were fit to the observed water-surface profiles, which were then used to estimate flow depth and other parameters of interest presented in the following tables. Table 7 summarizes reach-averaged flow depth Y within the control volume at model and prototype scales.

Table 7. Estimates of reach-averaged flow depth

System & Description	Q_m (cfs)	Smooth Wall ($\bar{Y}$, ft.)		Mixed Walls ($\bar{Y}$, ft.)		Tangent Walls ($\bar{Y}$, ft.)	
		Model	Prototype	Model	Prototype	Model	Prototype
System A *1:10, Smooth Bed*	38.6 [a]	1.10	10.97	1.46	14.63	1.51	15.12
	32.5	0.98	9.75	1.29	12.90	1.42	14.16
	27.8	0.87	8.67	1.16	11.56	1.25	12.46
	18.5	0.71	7.12	0.90	9.03	0.96	9.64
	9.3	0.48	4.83	0.58	5.85	0.62	6.16
System B *1:10, ACB*	38.6 [a]	1.45	14.45	1.52	15.19	1.54	15.44
	32.5	1.28	12.78	1.36	13.62	1.40	13.99
	27.8	1.19	11.88	1.24	12.42	1.28	12.77
	18.5	0.89	8.86	0.98	9.82	0.99	9.86
	9.3	0.64	6.39	0.67	6.69	0.67	6.70
System C *1:24, Smooth Bed*	17.5	0.54	13.01	0.59	14.08	0.66	15.84
	15.6	0.50	11.96	0.53	12.74	0.60	14.46
	13.4	0.44	10.67	0.48	11.52	0.53	12.77
	10.4 [a]	0.38	9.19	0.42	10.10	0.47	11.19
	8.9	0.34	8.10	0.36	8.66	0.42	10.18
	5.2	0.24	5.68	0.25	6.02	0.28	6.74
System D *1:24, ACB*	17.5	0.78	18.72	0.80	19.24	0.83	19.97
	15.6	0.70	16.87	0.74	17.74	0.76	18.36
	13.4	0.65	15.59	0.67	16.02	0.72	17.18
	10.4 [a]	0.55	13.12	0.59	14.22	0.60	14.44
	8.9	0.50	11.89	0.53	12.84	0.57	13.57
	5.2	0.35	8.32	0.38	9.04	0.37	8.95

[a] Corresponding to the 100-year design discharge applicable to the RPN case study project

Table 8 summarizes reach-averaged Froude number Fr and reach-averaged friction slope $\overline{S_f}$. For the 1:10-scale model, the value Fr = 0.71 was found to be representative of the design condition (System B, tangent walls, 38.6 cfs). This condition corresponded to a 50 ft. prototype width and met the target criteria of $\mathrm{Fr} \leq 0.80$. For the 1:24-scale model, Fr = 0.78 was found to be representative of the design condition (System D, tangent walls, 10.4 cfs). This condition corresponded to the prototype channel width of 120 ft. and met the target criteria of $\mathrm{Fr} \leq 0.80$.

Table 8. Estimates of reach-averaged Froude number and friction slope

System & Description	Q_m (cfs)	Smooth Walls		Mixed Walls		Tangent Walls	
		Fr	$\overline{S_f}$	Fr	$\overline{S_f}$	Fr	$\overline{S_f}$
System A *1:10, Smooth Bed*	38.6 [a]	1.18	0.0043	0.77	0.0048	0.73	0.0068
	32.5	1.19	0.0054	0.78	0.0041	0.68	0.0066
	27.8	1.21	0.0046	0.79	0.0056	0.70	0.0063
	18.5	1.09	0.0041	0.76	0.0055	0.78	0.0060
	9.3	0.97	0.0021	0.73	0.0046	0.67	0.0046
	Mean	1.13	0.0041	0.77	0.0049	0.71	0.0061
System B *1:10, ACB*	38.6 [a]	0.78	0.0038	0.73	0.0058	0.71	0.0077
	32.5	0.79	0.0043	0.72	0.0062	0.69	0.0069
	27.8	0.76	0.0048	0.71	0.0064	0.68	0.0071
	18.5	0.78	0.0046	0.67	0.0053	0.67	0.0061
	9.3	0.64	0.0034	0.60	0.0045	0.59	0.0052
	Mean	0.75	0.0042	0.68	0.0056	0.67	0.0066
System C *1:24, Smooth Bed*	17.5	1.55	0.0079	1.37	0.0080	1.15	0.0063
	15.6	1.56	0.0077	1.42	0.0085	1.18	0.0064
	13.4	1.59	0.0077	1.42	0.0079	1.21	0.0069
	10.4 [a]	1.54	0.0071	1.34	0.0063	1.15	0.0050
	8.9	1.60	0.0074	1.45	0.0078	1.14	0.0047
	5.2	1.59	0.0079	1.46	0.0080	1.23	0.0055
	Mean	1.57	0.0076	1.41	0.0077	1.18	0.0058
System D *1:24, ACB*	17.5	0.90	0.0040	0.86	0.0048	0.81	0.0051
	15.6	0.93	0.0034	0.87	0.0046	0.82	0.0048
	13.4	0.90	0.0036	0.86	0.0050	0.78	0.0044
	10.4 [a]	0.91	0.0032	0.80	0.0039	0.78	0.0038
	8.9	0.90	0.0031	0.80	0.0040	0.74	0.0035
	5.2	0.90	0.0028	0.79	0.0031	0.80	0.0031
	Mean	0.91	0.0033	0.83	0.0042	0.79	0.0041

[a] Corresponding to the 100-year design discharge applicable to the RPN case study project

The composite value of Manning's roughness coefficient n_c was estimated using the relationships described in Section 5. Table 9 provides model and prototype-scale values of n_c, related by the scaling criteria established by Eq. (9). Trends suggest that the introduction of hydraulically rough walls has a large effect on flow resistance, particularly for the SUFA (1:10) model.

Table 9. Estimates of n_c at model and prototype scales

System & Descriptio	Q_m (cfs)	Smooth Wall (n_c)		Mixed Walls (n_c)		Tangent Walls (n_c)	
		Model	Prototype	Model	Prototype	Model	Prototype
System A *1:10, Smooth Bed*	38.6 [a]	0.012	0.017	0.018	0.027	0.023	0.034
	32.5	0.013	0.019	0.017	0.025	0.025	0.036
	27.8	0.012	0.017	0.020	0.029	0.023	0.034
	18.5	0.012	0.018	0.020	0.030	0.023	0.034
	9.3	0.010	0.014	0.019	0.028	0.021	0.031
	Mean	0.012	0.017	0.019	0.028	0.023	0.034
System B *1:10, ACB*	38.6 [a]	0.016	0.024	0.021	0.031	0.025	0.037
	32.5	0.017	0.025	0.023	0.033	0.025	0.036
	27.8	0.019	0.028	0.023	0.034	0.026	0.038
	18.5	0.018	0.027	0.023	0.033	0.025	0.036
	9.3	0.019	0.028	0.024	0.035	0.025	0.037
	Mean	0.018	0.026	0.023	0.033	0.025	0.037
System C *1:24, Smooth Bed*	17.5	0.012	0.020	0.014	0.023	0.014	0.024
	15.6	0.012	0.020	0.013	0.023	0.014	0.024
	13.4	0.011	0.019	0.013	0.022	0.014	0.024
	10.4 [a]	0.011	0.019	0.012	0.021	0.013	0.021
	8.9	0.011	0.018	0.012	0.021	0.012	0.021
	5.2	0.011	0.018	0.012	0.020	0.012	0.020
	Mean	0.011	0.019	0.013	0.022	0.013	0.022
System D *1:24, ACB*	17.5	0.015	0.025	0.017	0.028	0.018	0.031
	15.6	0.013	0.022	0.016	0.028	0.018	0.030
	13.4	0.014	0.024	0.017	0.029	0.018	0.030
	10.4 [a]	0.013	0.022	0.016	0.027	0.016	0.028
	8.9	0.013	0.022	0.016	0.028	0.017	0.028
	5.2	0.012	0.020	0.014	0.024	0.014	0.024
	Mean	0.013	0.022	0.016	0.027	0.017	0.029

[a] Corresponding to the 100-year design discharge applicable to the RPN case study project

As previously mentioned, due to the relatively short flume length (40 ft.), flow uniformity was not obtained within the subject models. Due to the influence of the downstream boundary condition, water depths may be subject to change for the prototype channel. By using non-uniform gradually varied flow equations, however, results from this model are sufficient for computing estimates of Manning's *n*.

Results indicate that at narrower channel widths the tangent walls exert a larger impact on n_c. For the 1:24 scale model, which corresponded to a 120 ft. prototype channel width, the value n_c = 0.028 was found to be representative of the prototype design condition (System D, tangent walls, 10.4 cfs). For the 1:10 scale model, which corresponded to a 50 ft. prototype channel width, the value n_c = 0.037 was found to be representative of the prototype design condition (System B, tangent walls, 38.6 cfs). Each system was assessed with three wall configurations (smooth, mixed, tangent) as described in Section 4.3. The resulting values of n_c for a given system-wall configuration depended on representative values of Y, and the $\overline{S_f}$ computed for a given water-surface profile. Prototype values of n_c, Y, and $\overline{S_f}$ are presented graphically in the following sections as a basis of comparison for the systems evaluated in this study.

6.1 System A

System A consisted of a smooth metal channel bed and cylindrical foam walls built at a length scale ratio of 1:10. Observed water-surface profiles and cross-sections are shown in Appendix E Figures E1 – E6. Figure 14 provides depth trendlines for each wall configuration at the 100-year design discharge. At this flowrate, smooth walls were the only configuration that resulted in supercritical flow (Fr = 1.18). Five discharges were evaluated for each arrangement of the System A walls. A comparison of the resulting mean prototype n_c values, averaged over all flowrates evaluated, is provided in Figure 15 for each wall configuration. The use of smooth walls on both sides of the channel resulted in a 63% decrease in the mean values of the prototype n_c compared to the mixed condition.

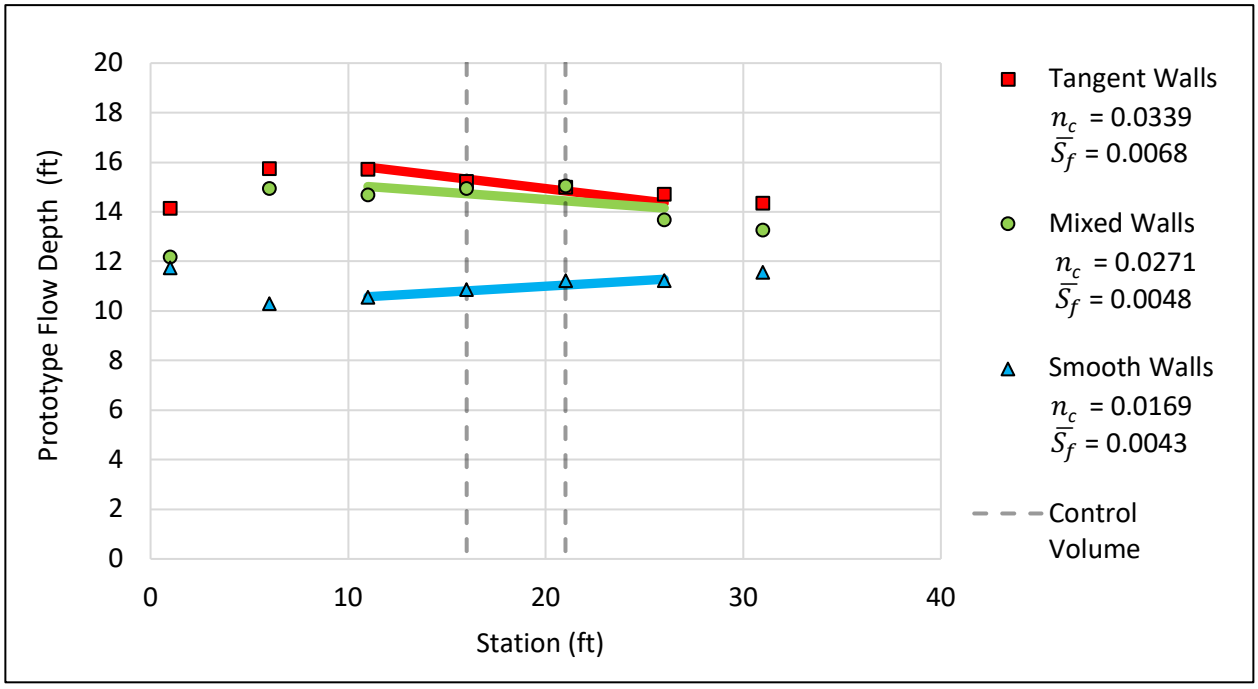

Figure 14. System A prototype flow-depth trendlines at the 100-year design discharge

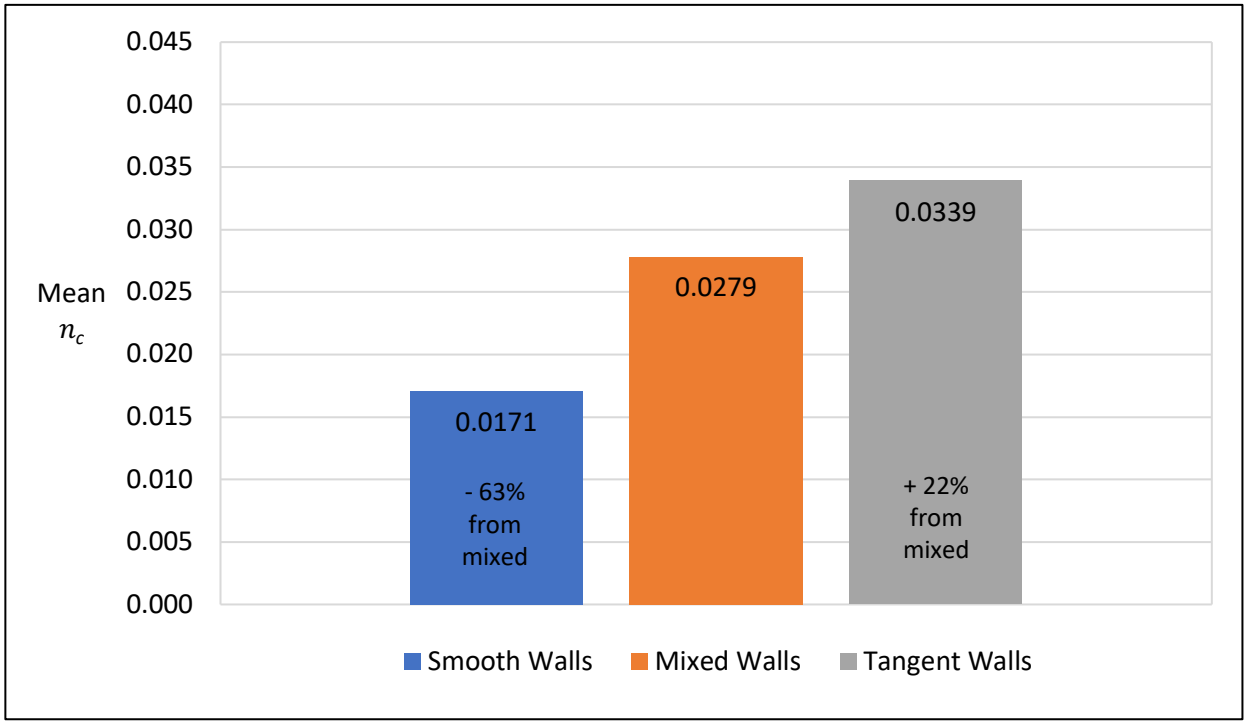

Figure 15. System A prototype n_c values, averaged over all flowrates evaluated

6.2 System B

System B consisted of a foam ACB channel bed and cylindrical walls built at a length scale ratio of 1:10. Observed water-surface profiles and cross-sections are shown in Appendix E Figure E7 – E12. Figure 16 provides flow depth trendlines for each wall configuration at the 100-year design discharge. As summarized in Table 8, each test for System B resulted in subcritical flow. Five flowrates were evaluated for each arrangement of the walls. A comparison of the mean n_c values, averaged over all flowrates evaluated, is provided in Figure 17 for each wall configuration.

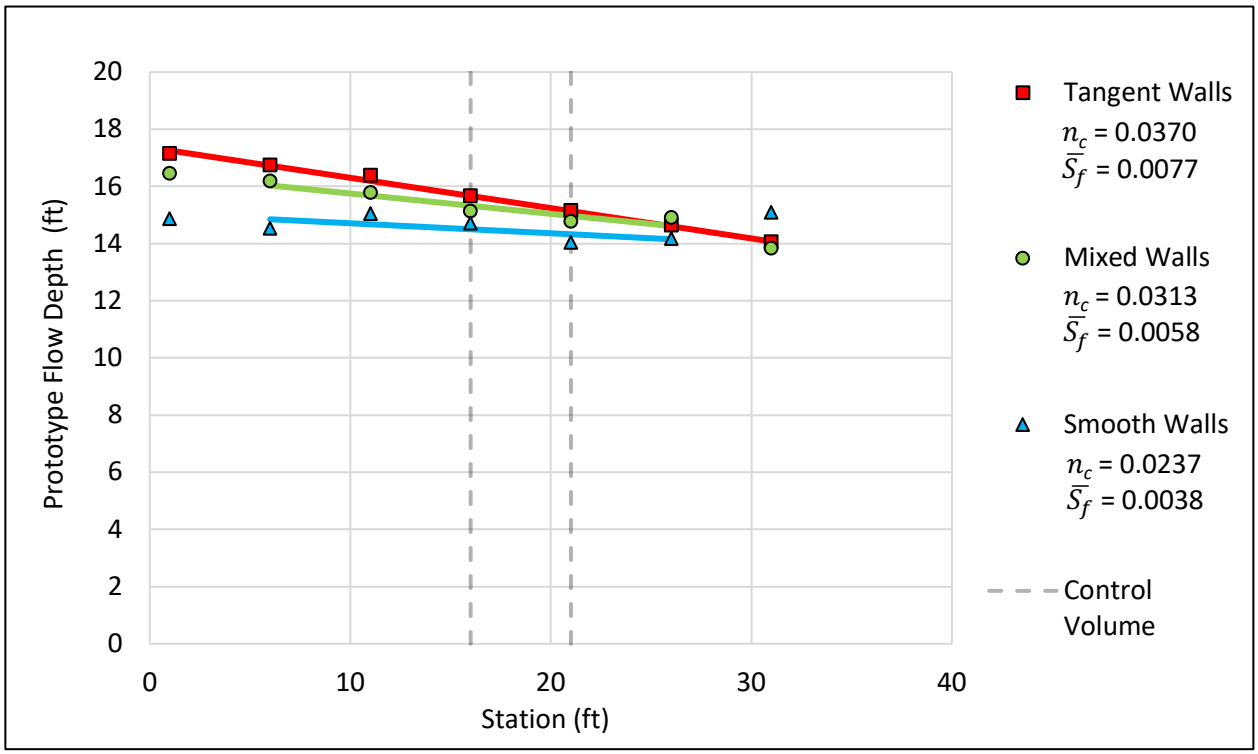

Figure 16. System B prototype flow-depth trendlines at the 100-year design discharge

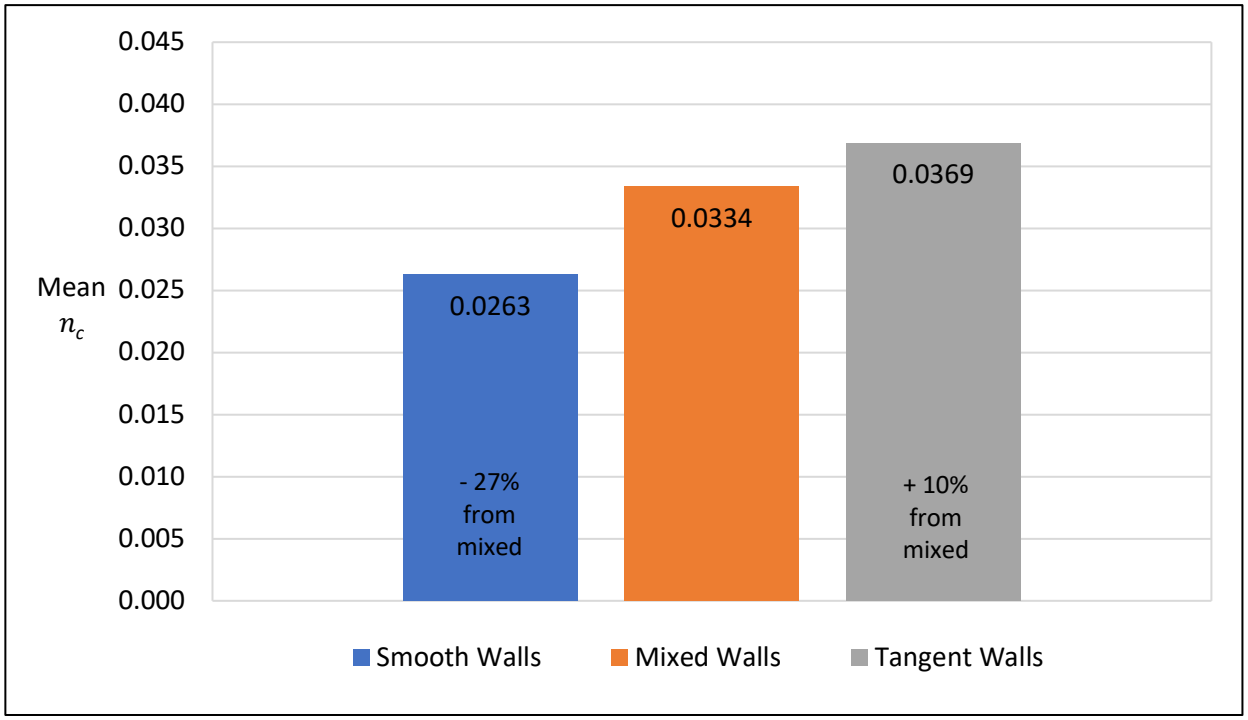

Figure 17. System B prototype n_c values, averaged over all flowrates evaluated

6.3 System C

System C consisted of a smooth metal channel bed and cylindrical foam walls built at a length scale ratio of 1:24. Observed water-surface profiles and cross-sections are shown in Appendix E Figures E13 – E18. Figure 18 provides flow depth trendlines for each wall configuration at the 100-year design discharge. As summarized in Table 8, each test for System C resulted in supercritical flow. Six discharges were evaluated for each arrangement of the System C walls. Figure 19 compares the resulting values of mean n_c, averaged over all flowrates evaluated, for each wall configuration.

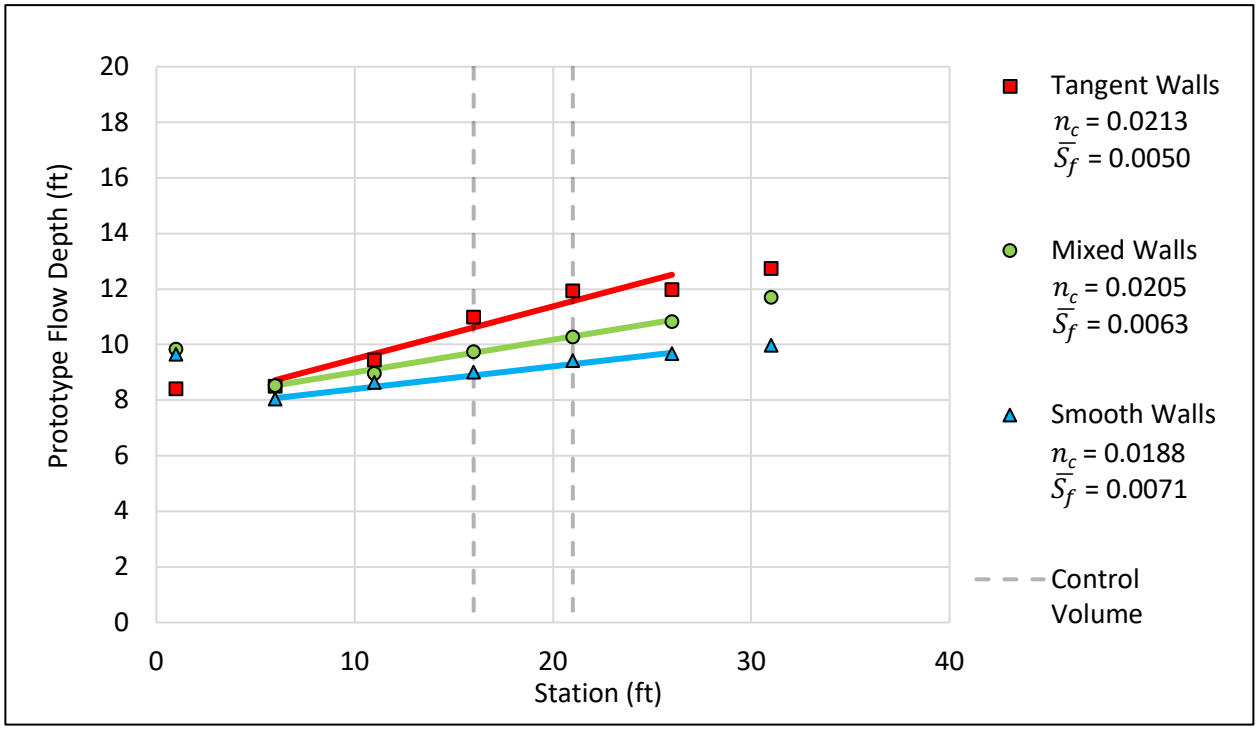

Figure 18. System C prototype flow-depth trendlines at the 100-year design discharge

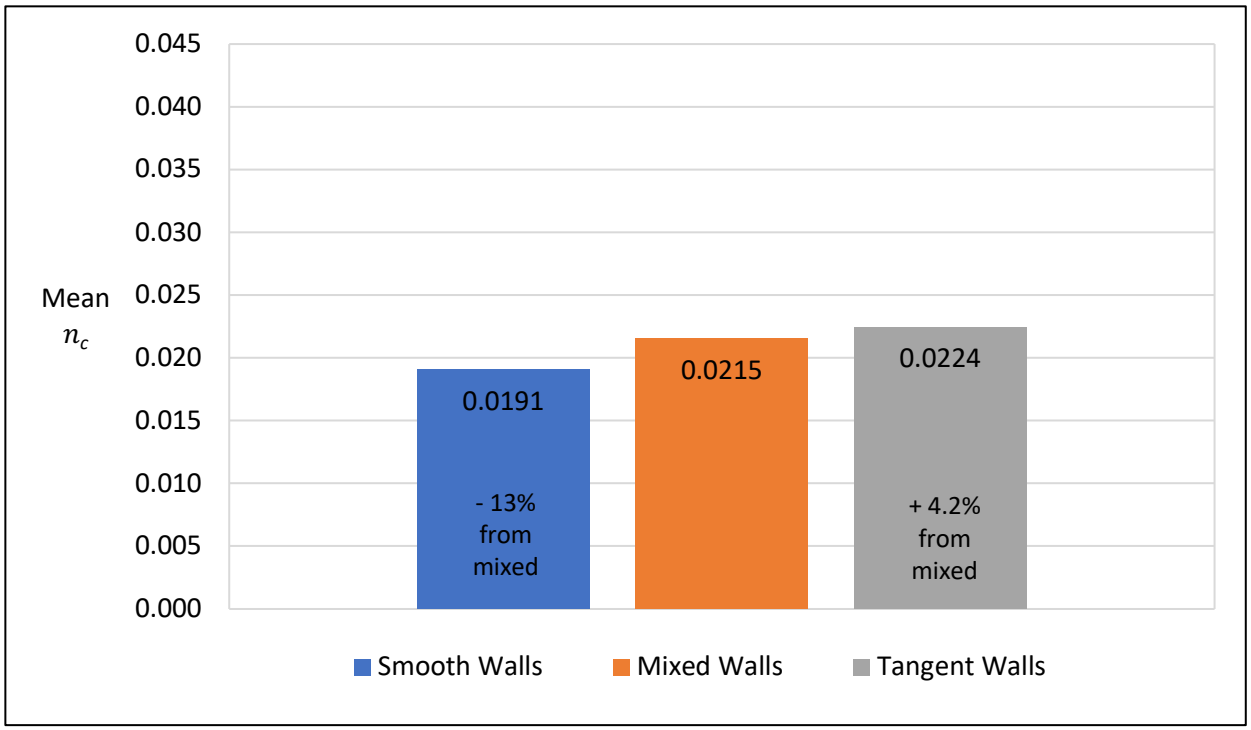

Figure 19. System C prototype n_c values, averaged over all flowrates evaluated

6.4 System D

System D consisted of a foam ACB channel bed and cylindrical walls built at a length scale ratio of 1:24. Observed water-surface profiles and cross-sections are shown in Appendix E Figures E19 – E24. Figure 20 provides flow depth trendlines for each wall configuration at the 100-year design discharge. As summarized in Table 8, each test for System D resulted in subcritical flow. Six discharges were evaluated for each arrangement of the System D walls. Figure 21 compares the resulting values of mean n_c, averaged over all flowrates evaluated, for each wall configuration.

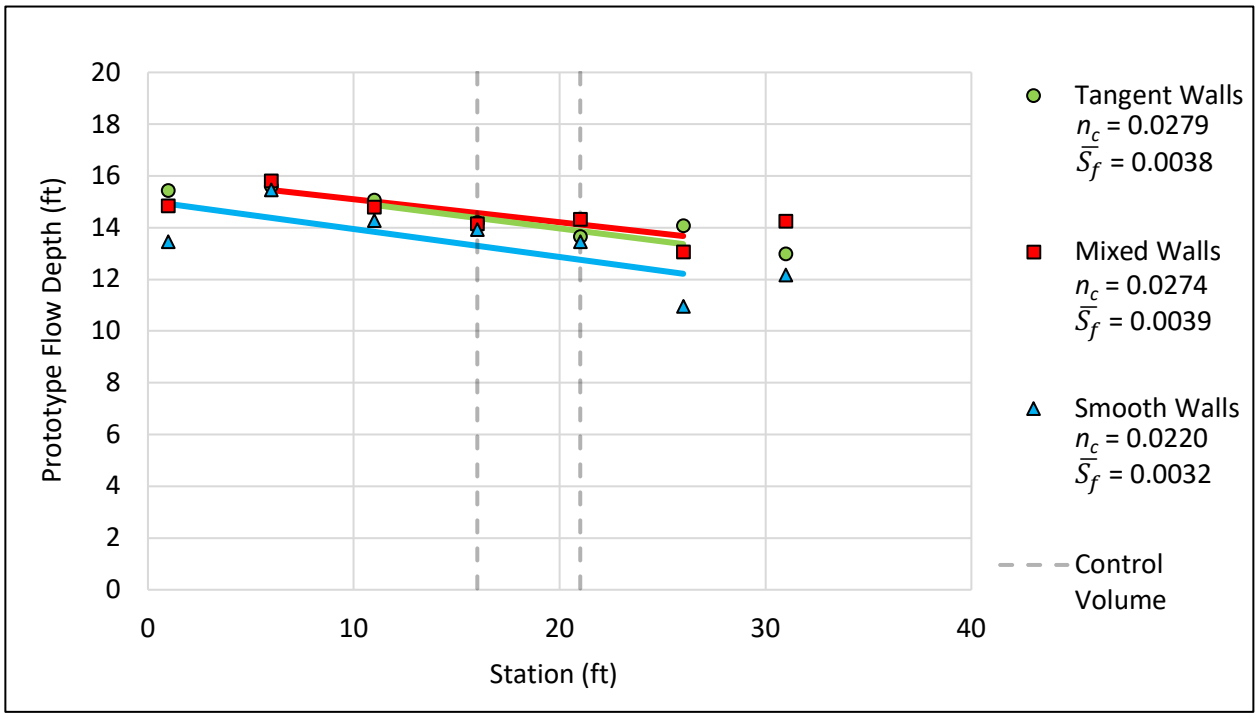

Figure 20. System D prototype flow-depth trendlines at the 100-year design discharge

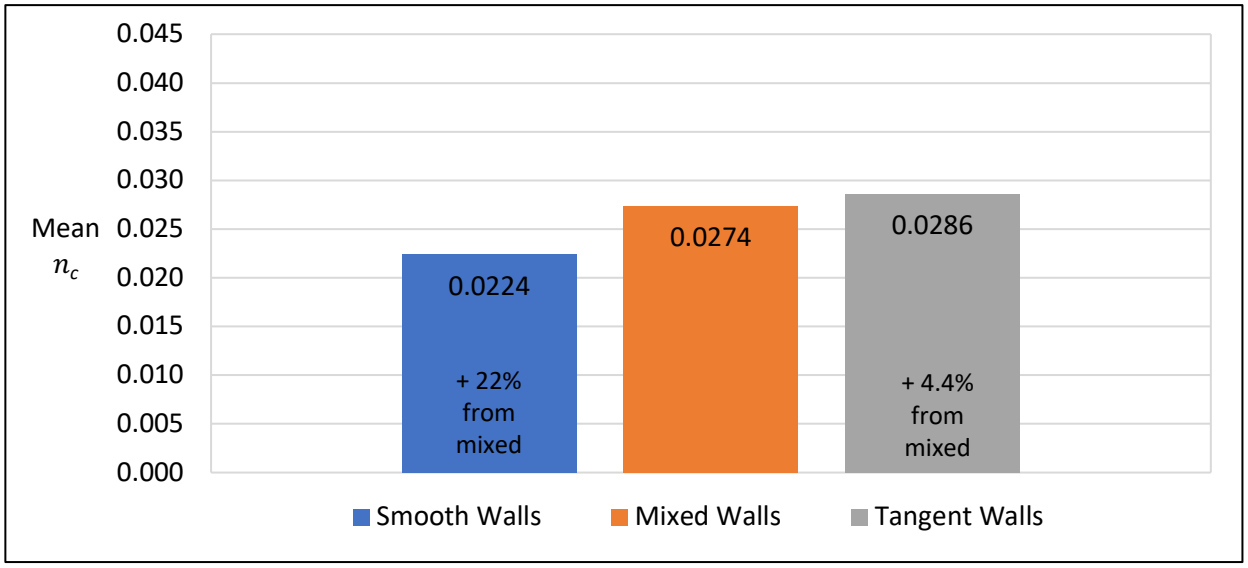

Figure 21. System D prototype n_c values averaged over all flowrates evaluated

6.5 Summary

Figure 22 presents a summary of mean n_c values averaged for all flowrates evaluated. This figure indicates that the addition of rough boundary elements has a greater effect on n_c values at 1:10 scale. Additionally, n_c values were found to be generally larger at 1:10 scale than their 1:24 scale counterpart.

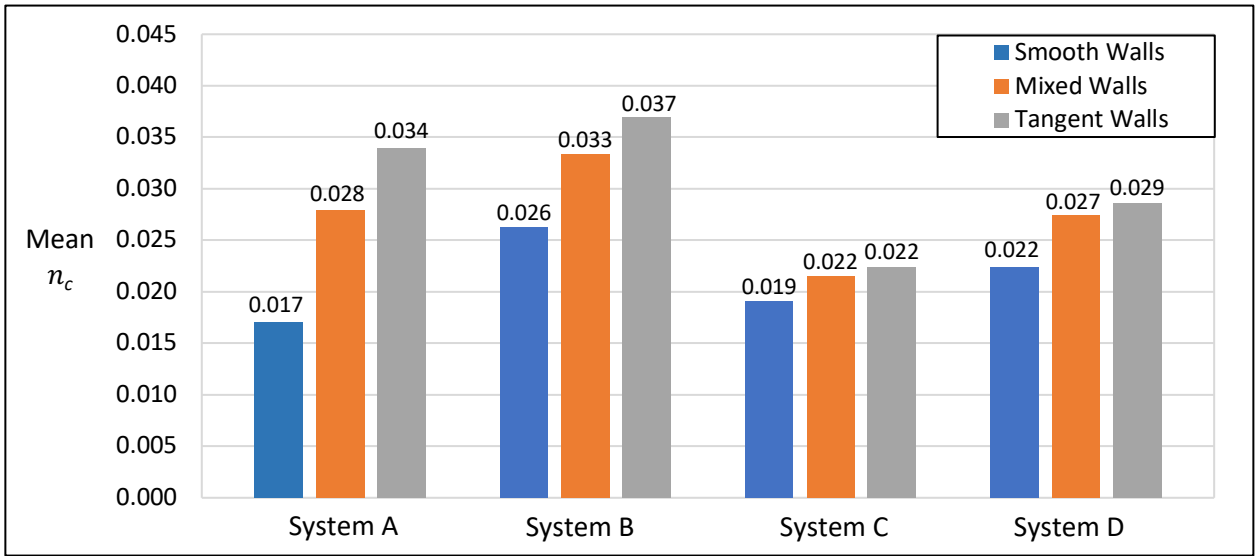

Figure 22. Summary of prototype n_c values averaged over all flowrates evaluated

7 DISCUSSION

7.1 Reynolds Number Estimates

Viscous effects are generally considered negligible for the open-channel flows operating within the fully turbulent region (Sturm, 2001). Flow field variations within the water column, and near boundary layers, however, can generate variability in the Reynolds number. It is necessary, therefore, to estimate Reynolds number for a physical model, to demonstrate that flow is operating within the fully turbulent region ($\mathrm{Re} > 4000$).

The force effects of water viscosity may be characterized in terms of bulk Reynolds number (VY/υ) for open-channel flow; where, V = bulk average velocity, Y = flow depth and υ = kinematic viscosity of water at a given temperature. Reynolds number, however, varies with elevation within a water column, due to variations in flow velocity. Additionally, the effects of Reynolds number due to tangent wall diameter may not be completely negligible (VD/υ); where D = diameter. The same issue concerns the ACB boundary layer.

Estimates of Reynolds number for the 100-year design event on the RPN project are provided in Table 11. Here, the kinematic viscosity of water was estimated as $\upsilon = 1.48 \times 10^{-6}$ ft^2/s at a temperature of 47^{o}F. Cross-section averaged velocity, computed using a continuity relationship, was used to estimate the bulk Reynolds number. ADV measurements were not captured for the 1:24 scale model as they were for the 1:10 scale model. Therefore, Re specific to the tangent walls, estimated using the ADV measurement of velocity closest to the wall boundary layer within the control volume, were only estimated for System B. Estimates reported in Table 10 indicate that the Re is operating within the fully turbulent region at the

design discharge, both within the bulk averaged cross-section, as well as along the tangent walls. Scale effects due to viscous forces were therefore considered negligible for the purposes of this thesis.

Table 10. Reynolds number estimates at the 100-year design discharge

System	B	D
Length Scale Ratio	1:10	1:24
Velocity (from continuity, fps)	5.01	3.46
Velocity (from ADV at walls, fps)	4.73	-
Flow depth (ft.)	1.54	0.60
Diameter (tangent walls, ft.)	0.60	0.25
Re (bulk, cross-section averaged)	521,809	140,404
Re (tangent walls)	191,737	-

ADV measurements on the RPN project reflect the velocity captured at 60% of the depth from the top of the water column as an approximate representation of the depth-averaged velocity. Future physical models employing ADV velocimeter instrumentation should strive to also capture velocity estimates near the channel bed such the Re can be estimated for the bottom boundary layer (e.g., ACB) in addition to the wall boundary layer.

Evaluation of the Reynolds number at lower flowrates, or alternate channel boundary configurations, may result in estimates of the Reynolds number below those reported in Table 10. Further evaluation of Reynolds number and associated scale effects due to viscous forces, however, would require a supplemental effort outside the scope of the subject thesis.

7.2 Comparison of Prototype Results for Two Models Developed at Different Length-scale factors

To mitigate potential sources of error (due to magnification, instrumentation precision limitations, or scale effects) it is generally desirable to minimize the length-scale factor such that model geometry matches as closely as possible to prototype channel geometry. Recall that the scale for a given physical model may be characterized by length scale ratio, given by the ratio of the model to prototype scale geometry (M:P), and length-scale factor, which is given by prototype to model scale geometry (P:M). The present study used two length scale ratios to investigate the effect of the model scale on values of n_c: 1:24 and 1:10. The 1:24 model enabled the full width of the prototype channel to be simulated and led to decreased values of flow resistance, compared to the 1:10 length scale ratio that employed SUFA.

A 1:10 length scale ratio (and associated SUFA) was initially selected for the RPN project due to available facilities and the desire to minimize the length-scale factor. At this scale, a channel width of 50 ft. was modeled using a 5.0-foot-wide internal width in the assembled model. A scaled unit flowrate was selected using concepts of Froude similitude, as summarized in Table 3. Results from the 1:10 model (Systems A and B) indicated that the tangent walls were the primary boundary element contributing to the overall flow resistance, and therefore, increased values of n_c. Secondary currents induced by the walls were observed to interact with one another in the center of the channel, particularly in the case of the SUFA model, which had larger diameter walls at the model scale, and a smaller channel width at the prototype scale. Mixed wall tests indicated that secondary flow currents extended beyond the center of the channel. These currents were believed to have increased values of flow resistance due to the addition of dispersive stresses that consumed flow energy.

A supplemental length-scale factor was used to evaluate the flow resistance performance at the full design width of the prototype channel. The goal of this model was to investigate n_c values at a lesser

length scale, such that the full 120.0 ft. design width of the prototype channel could be accommodated. Therefore, a length scale ratio of 1:24 was selected for System C and D. A length-scale factor of 24 enabled the full 120.0 ft. prototype channel to be modeled within the 5.0 ft. internal width of the assembled model.

Relationships between prototype values of n_c and channel width were developed using the results from the two models developed at different length-scale factors. A comparison of the prototype flow depth trendlines and values of prototype n_c are presented in the following figures for the two models including ACB SPS at the 100-year design flow. Figure 23, Figure 24, and Figure 25 present results for the smooth, mixed, and tangent wall tests, respectively. For each wall configuration, the 1:10 scale model (System B) resulted in larger flow depths and estimates of n_c than the 1:24 scale model (System D).

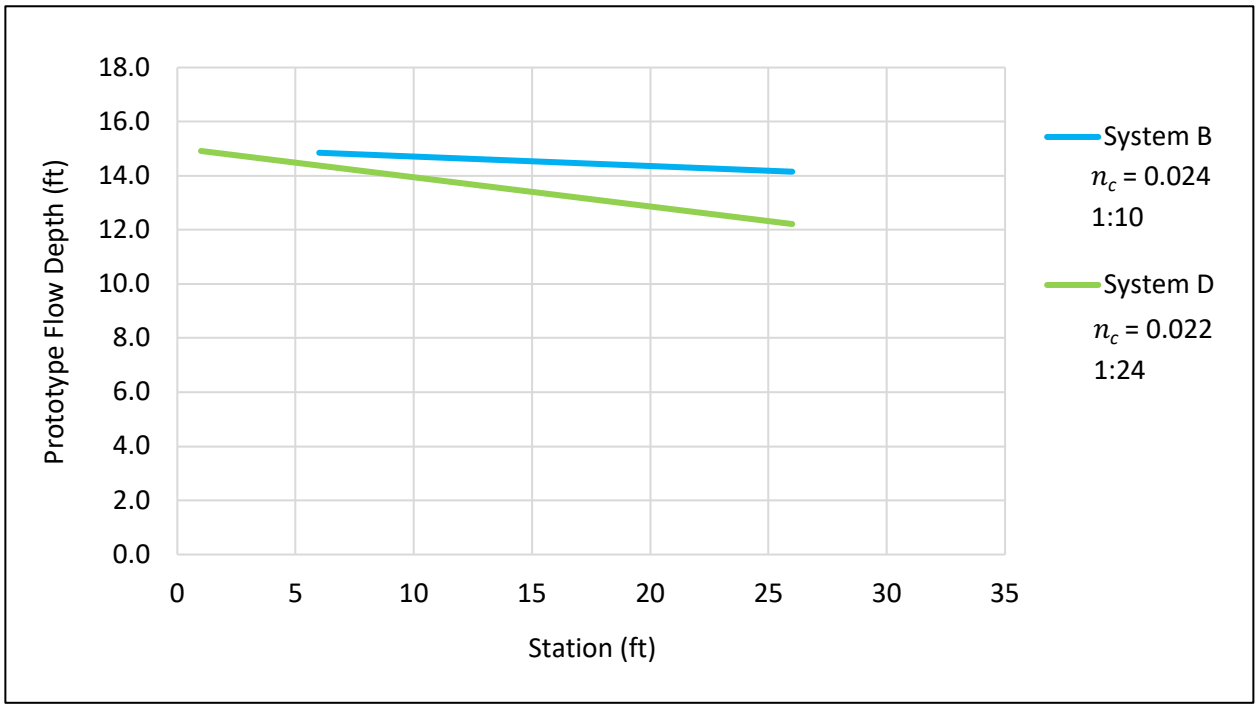

Figure 23. Smooth-wall prototype flow depth trendlines for 100-year flowrate

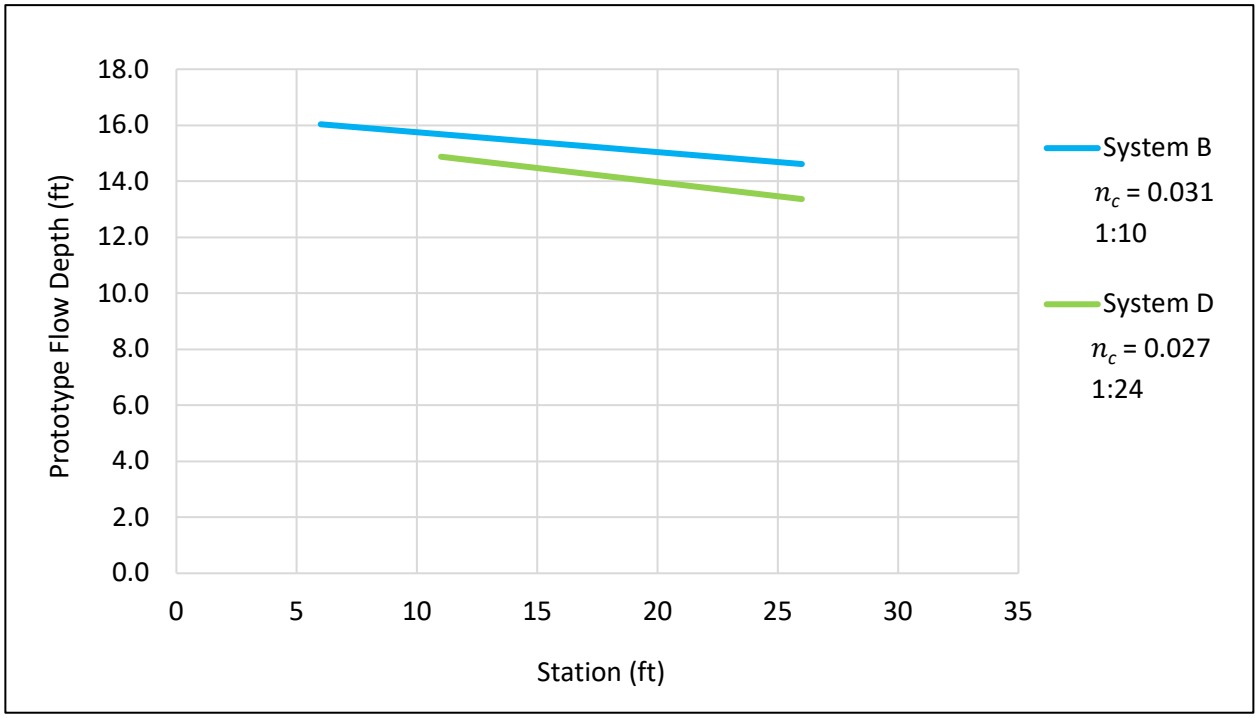

Figure 24. Mixed-wall prototype flow depth trendlines for 100-year flowrate

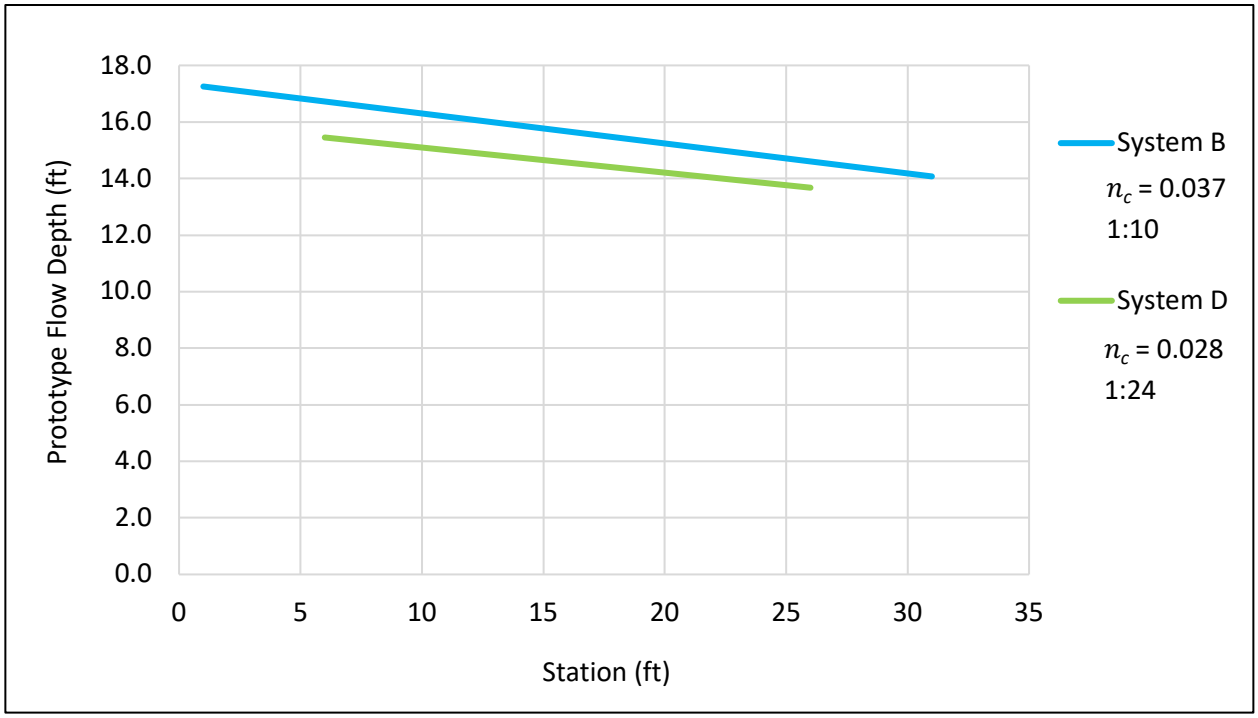

Figure 25. Tangent-wall prototype flow depth trendlines for 100-year flowrate

7.3 Unit Flowrate Comparisons

Three data sets were obtained for the ACB channel bed condition (smooth, mixed, tangent) for which tests were conducted at two model scales. The 1:10 model implemented SUFA and did not accommodate the full prototype channel width. The 1:24 model implemented a scaled design discharge and accommodated the full 120 ft. prototype channel width. Results comparison for these two model scales provided a case study for which insights were gleaned regarding implications associated with using a scaled unit flowrate, and how that differs from using a scaled design discharge, at various degrees of relative roughness between boundary elements.

Prototype flow depth was found to be consistently larger for System B (50 ft. prototype channel width) than System D (120 ft. prototype channel width) at the 100-year prototype unit flowrate of 244 cfs/ft, as shown by Figure 23, Figure 24, and Figure 25 for smooth, mixed and tangent walls, respectively. Flow depth and n_c are related by Eq. (12). For a given flowrate and friction slope, a larger flow depth results in a larger n_c. Conversely, Fr, described by Eq. (11) and summarized in Table 8, has an inverse relationship with Y. For a given flowrate, a larger flow depth results in a smaller value of Fr. The interrelation of these variables is essential for understanding the implications of applying SUFA results to a prototype channel with a greater channel width than modeled.

Figure 26, Figure 27, and Figure 28 provide a comparison results for n_c at prototype scale on Systems B and D, for the case of smooth, mixed, and tangent wall configurations, respectively. These depictions highlight that SUFA, as illustrated by prototype scale estimates from System B, resulted in larger estimates of n_c compared to the prototype results of System D. This finding is consistent with the relationship of depth and n_c described by Eq. (12), wherein System B results in larger depths and larger estimates of n_c compared to System D.

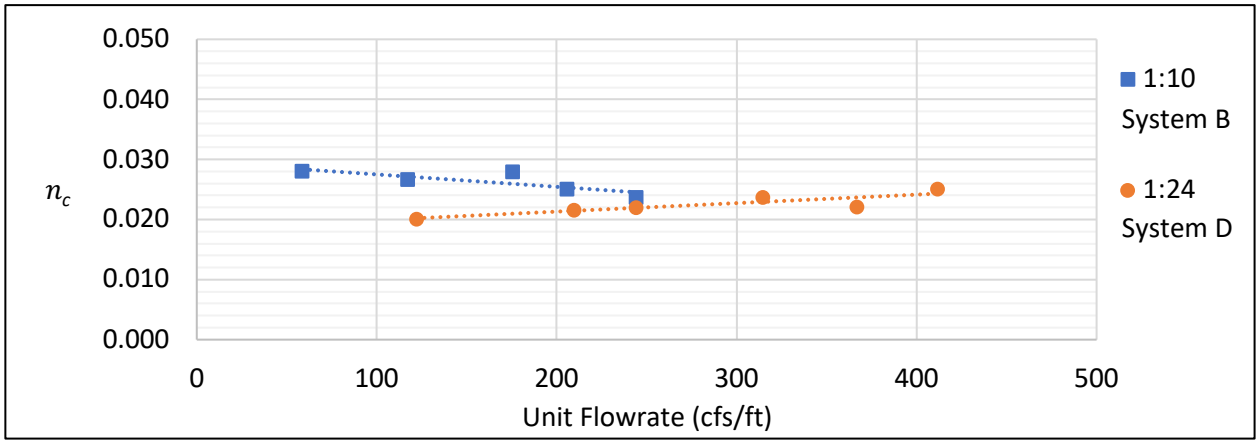

Figure 26. Prototype Manning's coefficient vs unit flowrate for ACB bed – smooth wall tests

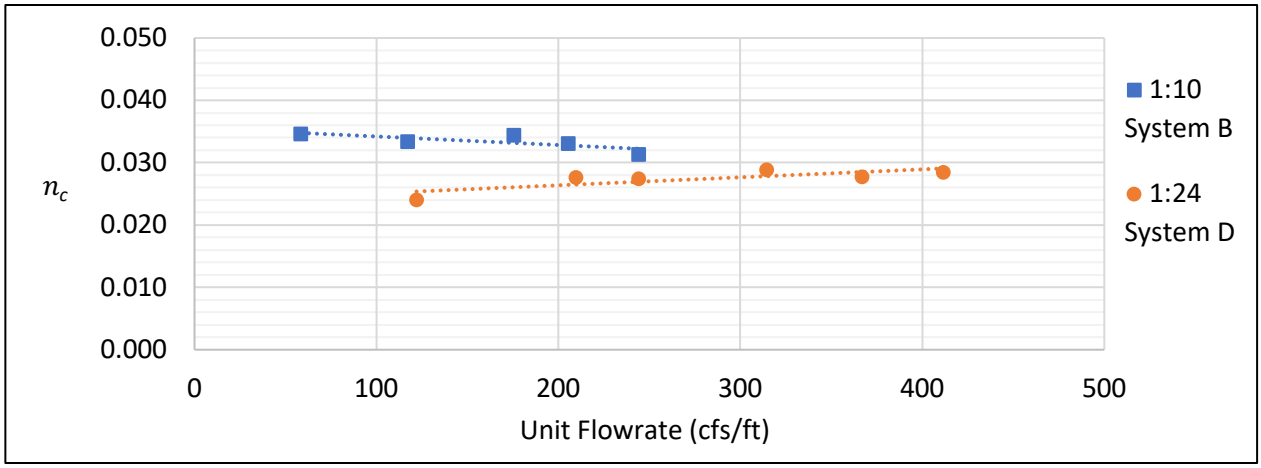

Figure 27. Prototype Manning's coefficient vs unit flowrate for ACB bed – mixed wall tests

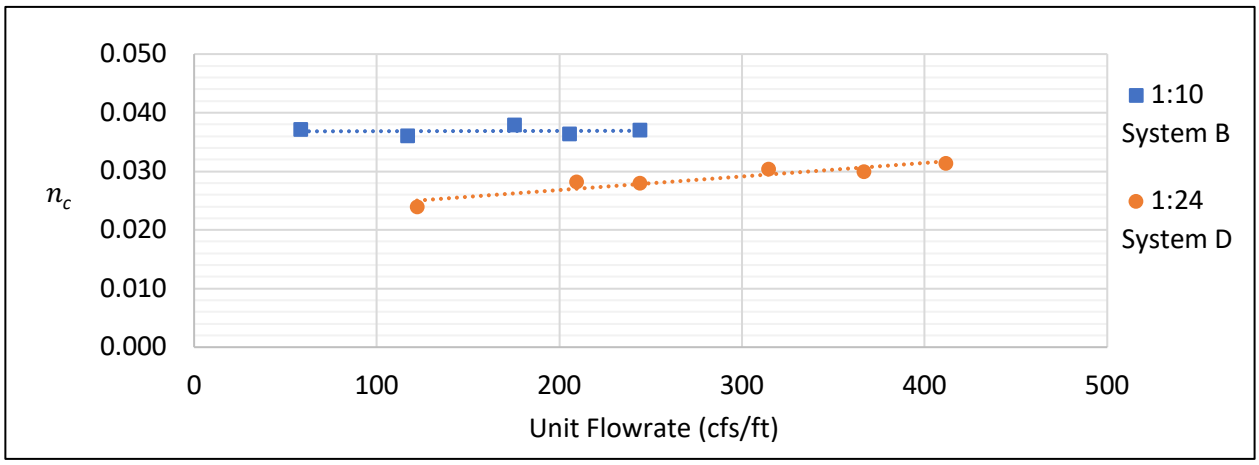

Figure 28. Prototype Manning's coefficient vs unit flowrate for ACB bed – tangent wall tests

Figure 29, Figure 30, and Figure 31 provide a comparison of results for Fr on Systems B and D, for the case of smooth, mixed, and tangent wall configurations, respectively. These depictions highlight that SUFA, as illustrated by estimates from System B, resulted in lower values of Fr compared to the prototype results of System D. This finding is consistent with the relationship of Y and Fr described by Eq. (11), wherein System B results in larger depths and lower estimates of Fr compared to System D. It is generally understood that for a given flowrate, a larger water depth indicates a lower velocity and Fr, and a larger value of Manning's *n* (Aqueel, Al-Adili, 2016).

Prototype scaling of Manning's roughness coefficient in this analysis is predicated on concepts on Froude-similitude, described by Eq. (9). Therefore, the applicable Froude number should be the same at model scale as it is at prototype scale, as described by Eq. (2). However, SUFA, as illustrated by results from System B, results in lower estimates of Fr, and higher estimates of n_c, compared to a scaled design discharge, as illustrated by results from System D. Therefore, because Eq. (2) is unsatisfied by SUFA, a correction is needed to adjust SUFA estimates of n_c such that flow resistance estimates apply to the prototype channel width condition.

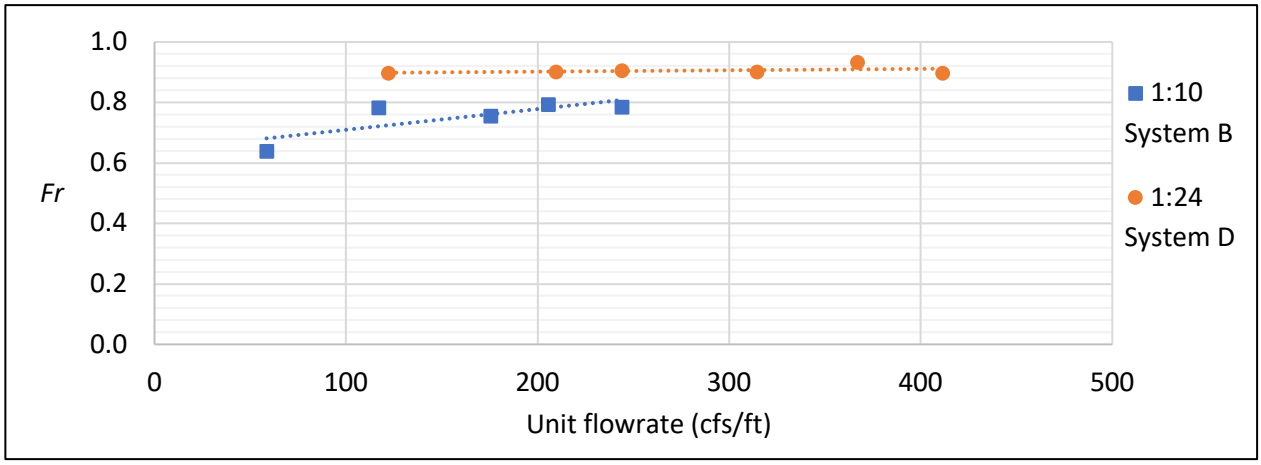

Figure 29. Froude number vs unit flowrate for ACB bed – smooth wall tests

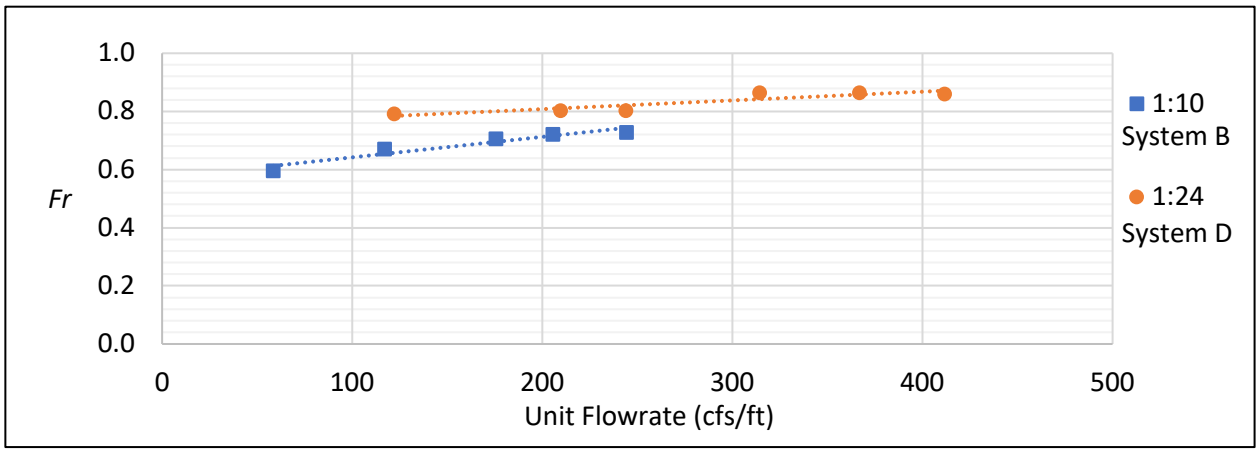

Figure 30. Froude number vs unit flowrate for ACB bed – mixed wall tests

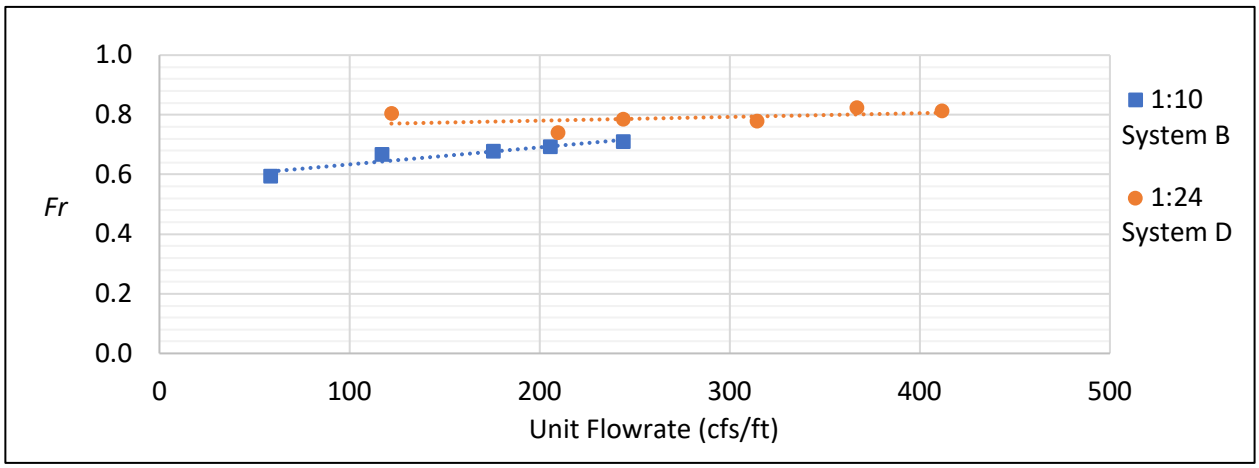

Figure 31. Froude number vs unit flowrate for ACB bed – tangent wall tests

7.4 Manning's Roughness Coefficient Decompositions

Values of composite Manning's *n* (n_c) at the model scale were broken into contributing components specific to each boundary element (n_i). Eq. (17) presents the Horton method and applicable variation for the subject rectangular channel, using the relationship between the total wetted perimeter P_{total}, the wetter perimeter of a given channel boundary P_i, and the associated Manning's *n* of that channel boundary n_i (Chow, V.T., 1959). The Horton method employs the simplifying assumptions that the velocities of each wetted perimeter subsection are equivalent to the mean velocity of the composite cross-section (Sturm, 2001). Here, n_b indicates a value for n_i pertaining to the channel bed. Similarly, a value for n_i pertaining to the channel walls is given variable designations n_w. Rearranging Eq. (17) to solve for n_i produced the model-scale estimates of Manning's roughness coefficient specific to each boundary element. The resulting values of n_i were then adjusted using Eq. (9) to prototype scale.

$$n_c = \left(\frac{\sum_{i=1}^{n}(P_i\, n_i^{1.5})}{P_{total}}\right)^{2/3} = \left(\frac{2hn_w^{1.5}+wn_b^{1.5}}{2h+w}\right)^{2/3} \quad (17)$$

Data were collected for three wall variations (smooth, mixed, and tangent) and two channel bed variations (smooth and ACB) at two model scales (1:10 and 1:24). The smooth wall-smooth bed test was used as a control, establishing a basis for smooth boundaries. By approximating the n_c obtained in this test as the n_i of smooth boundary elements, estimates for other wall and bed elements were then able to be isolated. Similarly, the mixed-wall smooth-bed tests served as a control for which the mixed-wall n_w could be isolated, and the tangent-wall smooth-channel bed tests served as a control for which the tangent-wall n_w could be isolated. In this way, computations for n_i for 1:10 scale data used values of n_c obtained from tests on Systems A and B; and computations for the 1:24 scale data used values of n_c obtained from tests on Systems C and D.

Eq. (18) presents the ratio of Manning's *n* obtained from the channel wall and bed material, hereafter termed relative roughness, and given the variable designation Γ. By Eq. (18), values of Γ > 1 indicate a channel in which walls exert a larger flow resistance value than the channel bed ($n_w > n_b$), and values of Γ < 1 indicate a channel in which the bed exerts a larger flow resistance value than the channel walls ($n_w < n_b$).

$$\Gamma = \frac{n_w}{n_b} \tag{18}$$

Table 11, Table 12, and Table 13 provide the results for n_w and n_b, and the associated n_c values (previously provided in Table 9), at both model and prototype scale, for smooth, mixed, and tangent walls, respectively. Additionally, estimates for relative roughness Γ are provided for each test condition.

Table 11. Values of n_i and n_c for ACB SPS, smooth walls and composite channel

Length Scale Ratio (M:P)	Q_m (cfs)	Composite (n_c)		Smooth Walls (n_w)		ACB (n_b)		Γ
		Model	Prototype	Model	Prototype	Model	Prototype	
1:10	38.6 [a]	0.016	0.024	0.012	0.017	0.018	0.027	0.62
	32.5	0.017	0.025	0.013	0.019	0.019	0.028	0.68
	27.8	0.019	0.028	0.012	0.017	0.022	0.032	0.53
	18.5	0.018	0.027	0.012	0.018	0.020	0.029	0.61
	9.3	0.019	0.028	0.010	0.014	0.021	0.031	0.46
	Mean	0.018	0.026	0.012	0.017	0.020	0.030	0.58
1:24	17.5	0.015	0.025	0.012	0.020	0.016	0.027	0.76
	15.6	0.013	0.022	0.012	0.020	0.013	0.023	0.87
	13.4	0.014	0.024	0.011	0.019	0.015	0.025	0.78
	10.4 [a]	0.013	0.022	0.011	0.019	0.013	0.023	0.83
	8.9	0.013	0.022	0.011	0.018	0.013	0.022	0.82
	5.2	0.012	0.020	0.011	0.018	0.012	0.020	0.90
	Mean	0.013	0.022	0.011	0.019	0.014	0.023	0.83

[a] Corresponding to the 100-year design discharge applicable to the RPN case study project

Table 12. Values of n_i and n_c for ACB SPS, mixed walls and composite channel

Length Scale Ratio	Q_m (cfs)	Composite (n_c)		Mixed Walls (n_w)		ACB (n_b)		Γ
		Model	Prototype	Model	Prototype	Model	Prototype	
1:10	38.6 [a]	0.021	0.031	0.028	0.041	0.017	0.025	1.66
	32.5	0.023	0.033	0.024	0.035	0.022	0.032	1.07
	27.8	0.023	0.034	0.033	0.049	0.018	0.026	1.86
	18.5	0.023	0.033	0.038	0.055	0.015	0.023	2.44
	9.3	0.024	0.035	0.047	0.068	0.015	0.023	3.02
	Mean	0.023	0.033	0.034	0.050	0.017	0.026	2.01
1:24	17.5	0.017	0.028	0.020	0.033	0.016	0.027	1.24
	15.6	0.016	0.028	0.021	0.035	0.015	0.025	1.40
	13.4	0.017	0.029	0.020	0.034	0.016	0.028	1.23
	10.4 [a]	0.016	0.027	0.017	0.029	0.016	0.027	1.09
	8.9	0.016	0.028	0.021	0.036	0.015	0.026	1.40
	5.2	0.014	0.024	0.020	0.035	0.013	0.022	1.56
	Mean	0.016	0.027	0.020	0.034	0.015	0.026	1.32

[a] Corresponding to the 100-year design discharge applicable to the RPN case study project

Table 13. Values of n_i and n_c for ACB SPS, tangent walls and composite channel

Length Scale Ratio	Q_m (cfs)	Composite (n_c)		Tangent Walls (n_w)		ACB (n_b)		Γ
		Model	Prototype	Model	Prototype	Model	Prototype	
1:10	38.6 [a]	0.025	0.037	0.038	0.055	0.016	0.023	2.38
	32.5	0.025	0.036	0.040	0.059	0.014	0.020	2.96
	27.8	0.026	0.038	0.041	0.060	0.016	0.024	2.53
	18.5	0.025	0.036	0.044	0.065	0.014	0.021	3.17
	9.3	0.025	0.037	0.051	0.075	0.016	0.024	3.17
	Mean	0.025	0.037	0.043	0.063	0.015	0.022	2.84
1:24	17.5	0.018	0.031	0.022	0.038	0.017	0.029	1.30
	15.6	0.018	0.030	0.023	0.039	0.016	0.027	1.45
	13.4	0.018	0.030	0.025	0.042	0.016	0.027	1.56
	10.4 [a]	0.016	0.028	0.019	0.033	0.016	0.027	1.23
	8.9	0.017	0.028	0.020	0.034	0.016	0.027	1.28
	5.2	0.014	0.024	0.020	0.033	0.013	0.022	1.48
	Mean	0.017	0.029	0.021	0.036	0.016	0.026	1.38

[a] Corresponding to the 100-year design discharge applicable to the RPN case study project

In all three cases, estimates of mean prototype n_c based on 1:10 scale results exceed associated estimates based on 1:24 scale model results. This indicates that the SUFA results in an overestimate of flow resistance values n_c. Thus, a reduction is needed to correct SUFA estimates of n_c such that they apply to the design prototype channel width. Furthermore, a more significant difference in resulting estimates of n_c is observed at larger values of Γ. Using mean prototype n_c values, a percent difference between the prototype results from each scale is computed as 16% for smooth walls, 20% for mixed walls, and 25% for tangent wall configurations, suggesting that a larger correction is needed for models with increased values of Γ.

7.5 Variable Channel Width

The 1:10 and 1:24 scale datasets in the 5 ft. wide assembled model corresponded to a prototype channel width of 50 ft. and 120 ft., respectively. Power trendline relationships were applied to prototype values of n_c, n_b, and n_w as a function of prototype channel width for each of the datasets compiled in Table 11, Table 12, and Table 13 as presented in Figure 32, Figure 33, and Figure 34, respectively. Solid lines represent the power relationship trendlines, derived by interpolating between known data points. Dashed lines represent extrapolations of these relationships, highlighting the potential trajectory of n values at prototype channel widths both smaller and larger than 50 ft. and 120 ft. data points, respectively.

The relationship between q and n_c was presented graphically in Figure 26, Figure 27, and Figure 28 for smooth, mixed, and tangent wall tests, respectively. While most unit flowrates were not the same in the 1:10 scale model as in the 1:24 scale model, there was not a consistent relationship between q and n_c, with which values of n_b, and n_w were derived from. Additional research would be needed to evaluate this relationship; therefore, an adjustment was not used to adjust n_c values to similar values of q.

Figure 32 provides a representation of the data compiled in Table 11, which pertains to a smooth wall-ACB channel bed condition with a mean relative roughness of Γ = 0.58 computed using the SUFA results. These data comprise the only test condition evaluated for which the bed Manning's *n* value exceeded that of the wall.

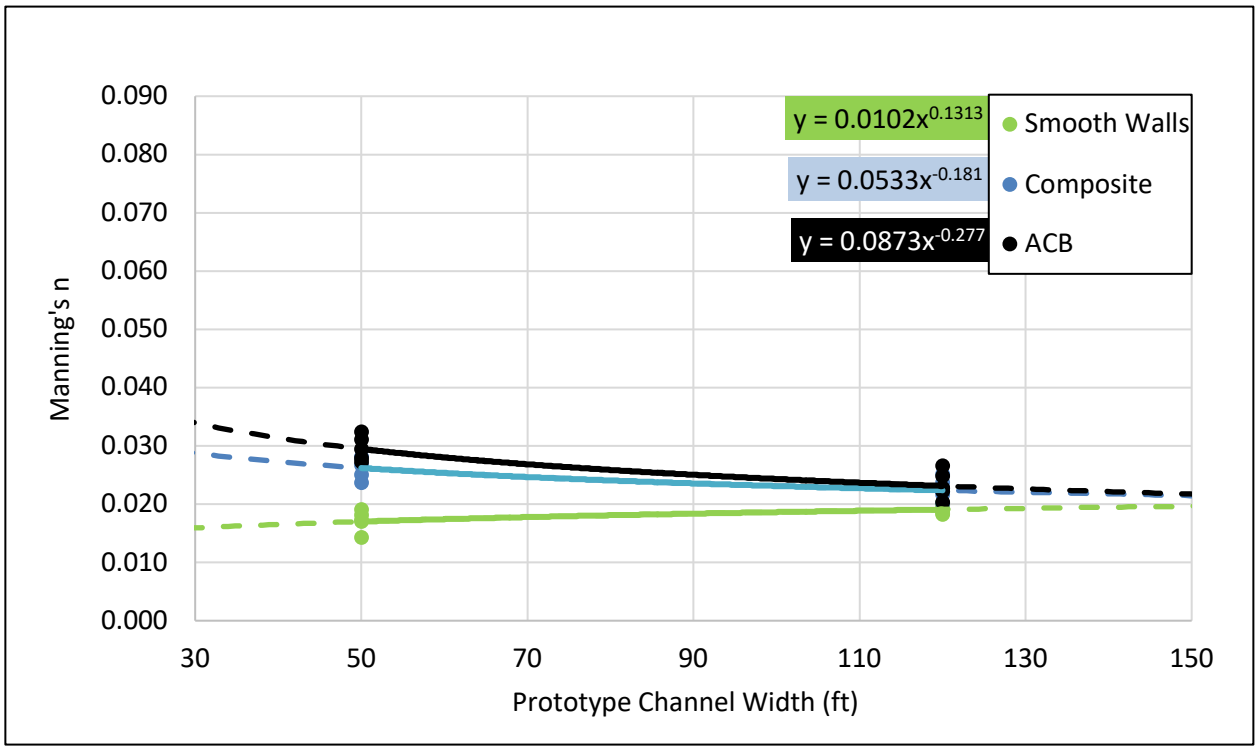

Figure 32. Prototype values of n_i and n_c versus channel width for ACB bed – smooth wall tests

Figure 33 provides a representation of the data compiled in Table 12 which pertains to a mixed wall-ACB channel bed condition with a mean relative roughness of Γ = 2.01 computed using the SUFA results. Figure 34 provides a representation of the data compiled in Table 13, which pertains to a tangent wall-ACB channel bed condition with a mean relative roughness of Γ = 2.84 computed using the SUFA results. The tangent walls were found to have significantly larger values of n_i than the ACB channel bed material. Increases to the prototype channel width were found to decrease estimates of n_c. This finding highlighted the significance of the sidewall roughness on composite flow resistance values.

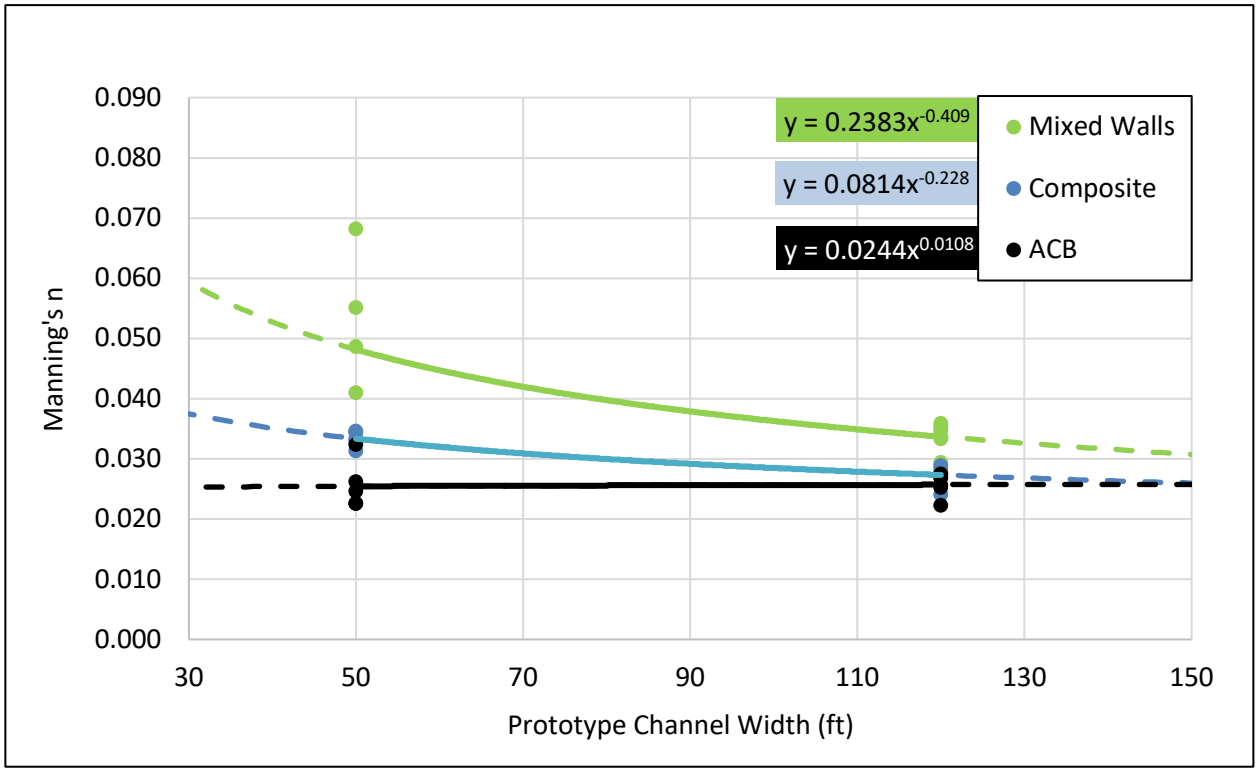

Figure 33. Prototype values of n_i and n_c versus channel width for ACB bed – mixed wall tests

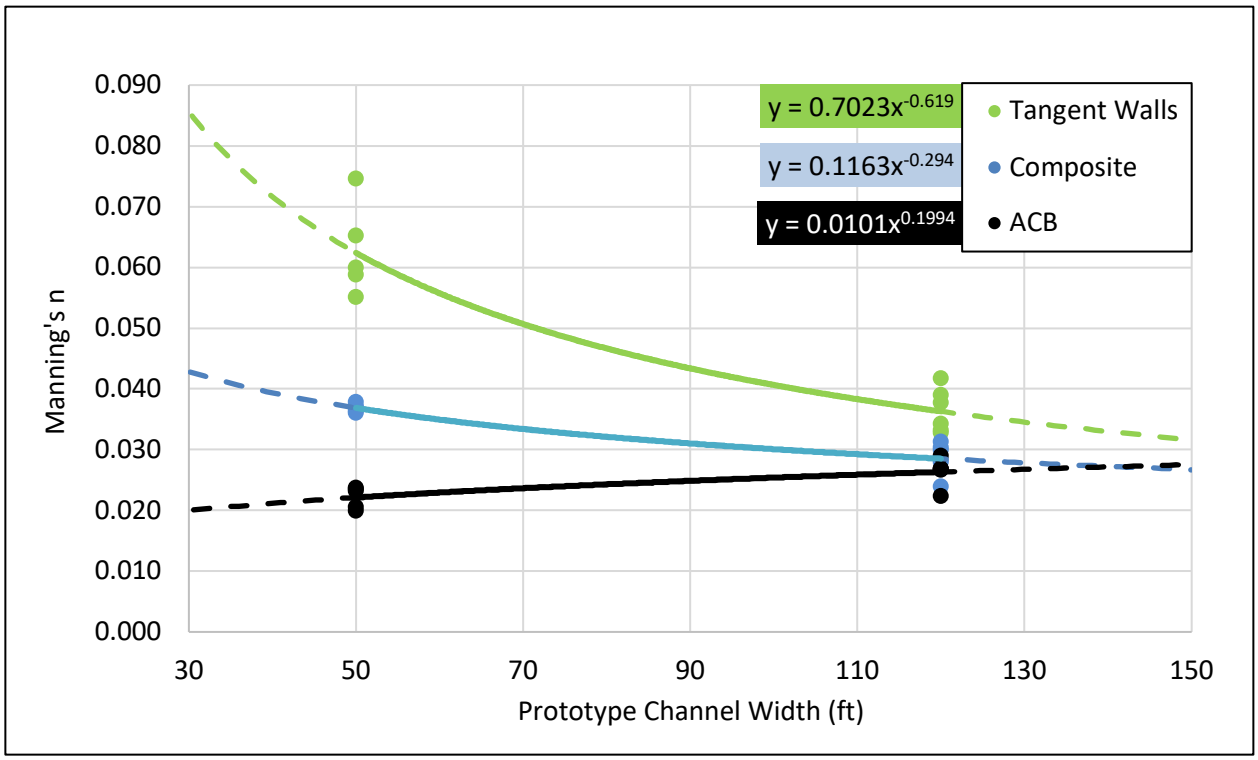

Figure 34. Prototype values of n_i and n_c versus channel width for ACB bed – tangent wall tests

These relationships illustrate the relationship that as prototype width deviates from the design width, applications of the SUFA deviate from the n_i and n_c that would be obtained for a model that accommodates the full prototype design channel width. Furthermore, these data indicate that estimates of n_i and n_c deviate more drastically for channels with larger values of Γ. The subsequent sections provide insights, adapting relationships specific to this project and generalizing such that they can be implemented on future projects that accommodate variable Γ and channel widths.

8 CORRECTION FACTORS

Approaches to account for the effects of sidewalls within a channel are referred to as sidewall corrections. Sidewall correction methods are essential for experiments in narrow laboratory channels with smooth metal or plexiglass sidewalls (Julien, 2010). Einstein used Manning's roughness coefficient to differentiate flow resistance components associated with the bed and wall, presented previously by Eq. (17). A sidewall correction using this equation was presented by Meyer-Peter and Mueller (1948) in their bedload derivation. Vanoni and Brooks also presented a sidewall correction using the Darcy-Weisbach friction factor instead of the Manning coefficient. While these approaches present corrections for sidewall effects, these correction factors were investigated specifically in studies involving bed shear stress computations to evaluate sediment transport in open channels (Cheng, 2005). A gap persists in the empirical evaluation of correction factors specific to flow resistance, specifically regarding rough-wall flows and Froude scaling applications. The research presented in this thesis uses data obtained in the RPN study to address the gap in the body of existing literature, proposing a new correction procedure based on empirical relations of flow resistance in open-channel flows.

8.1 Roughness Coefficient Correction Factors for Tested Values of Γ

A series of n_i and n_c corrections factors as a function of prototype channel width were established for various values of Γ based on the power relationships identified in Section 7.5. To improve applicability for future applications, channel width was normalized as a ratio. Relative channel width λ is given by Eq. (19). Here, w_q represents the prototype channel width modeled using SUFA and w_Q represents the total proposed prototype channel width. For the Rio Puerto Nuevo project, $\lambda = w_q / w_Q$ = 50 ft. / 120 ft. = 0.42.

$$\lambda = \frac{w_q}{w_Q} \tag{19}$$

By comparing the prototype results from the 1:10 model (SUFA) to the prototype results from the 1:24 model (accommodating the entire prototype design channel width), a correction factor as a function of λ was obtained. This correction factor is given the designation ψ, with sub designations ψ_c, ψ_w, and ψ_b, pertaining to the correction factors for n_c, n_w, and n_b, respectively. The subscripts *q* and *Q* refer respectively to the prototype-scale values obtained using the SUFA, and the associated prototype-scale estimate applicable to the full prototype channel width (w_Q). This leads to Eq. (20), Eq. (21), and Eq. (22), which establishes a means of applying the respective correction factor (ψ) to the prototype Manning's *n* value obtained in SUFA testing (n_q) to obtain an estimate for the related Manning's *n* value applicable to the full prototype channel width (n_Q).

$$n_{c,Q} = \psi_c n_{c,q} \tag{20}$$

$$n_{w,Q} = \psi_w n_{w,q} \tag{21}$$

$$n_{b,Q} = \psi_b n_{b,q} \tag{22}$$

The following figures present correction factors for interpolated values of λ (0.42 to 1) corresponding to the range of relative channel widths obtained from the power relationships shown by solid lines in Figure 32, Figure 33, and Figure 34, for the smooth wall-ACB model (mean Γ_q = 0.58), mixed wall-ACB model (mean Γ_q = 2.01), and tangent wall-ACB model (mean Γ_q = 2.84). Figure 35 provides estimates for correction factor ψ_c, which is applied to SUFA estimates of n_c as shown in Eq. (20). Figure 36 provides estimates for the correction factor ψ_w, which is applied to SUFA estimates of n_w as shown in Eq. (21). Figure 37 provides estimates for the correction factor ψ_b, which is applied to SUFA estimates of n_b as shown in Eq. (22).

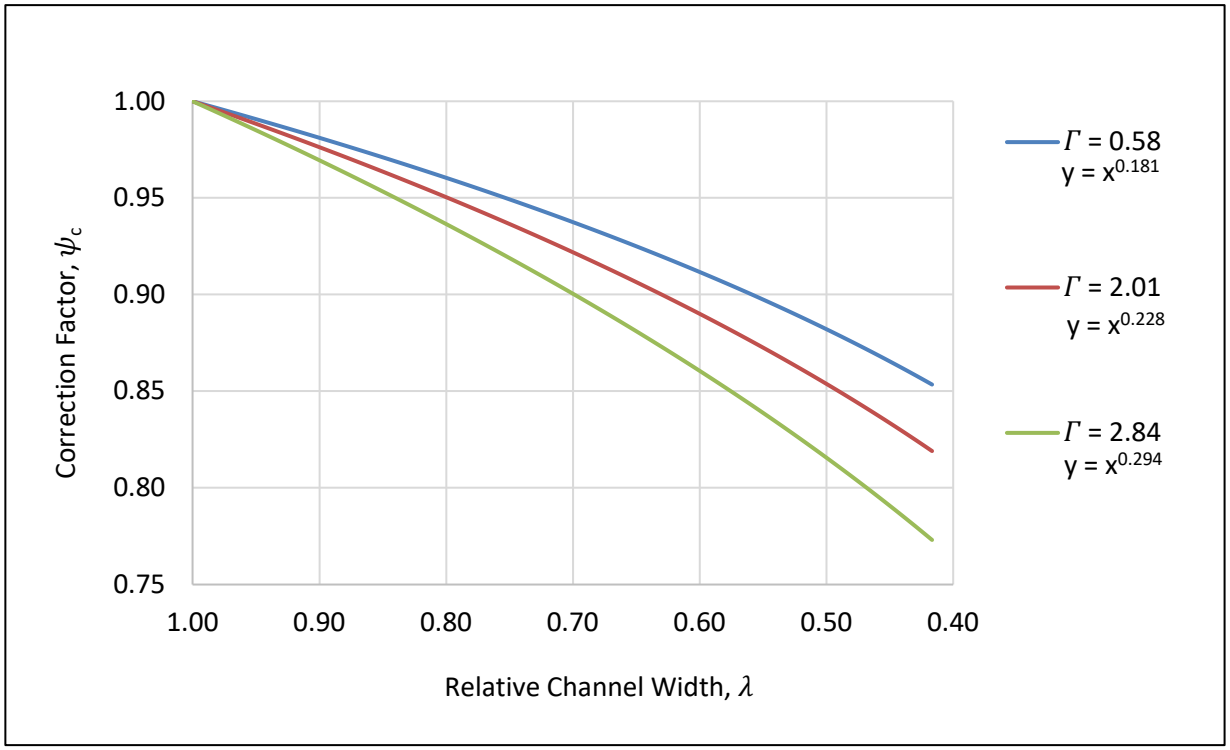

Figure 35. Correction factors for n_c versus relative channel width for tested values of Γ

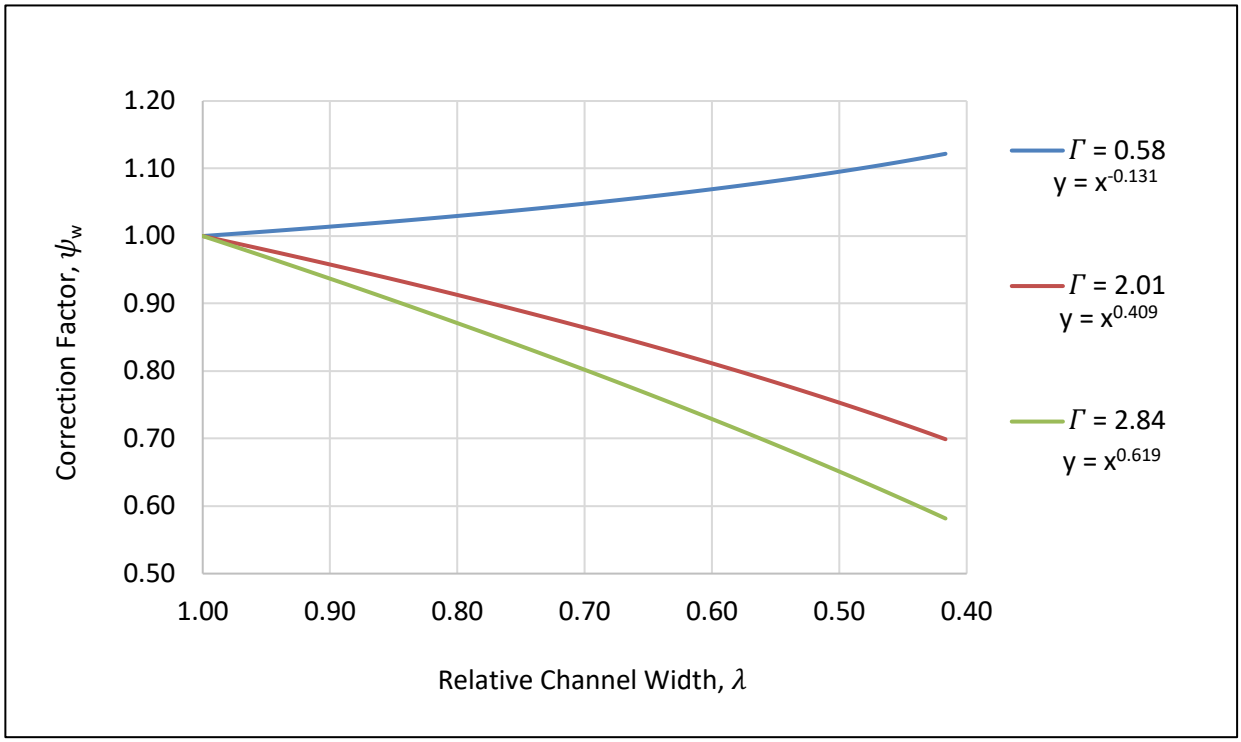

Figure 36. Correction factors for n_w versus relative channel width for tested values of Γ

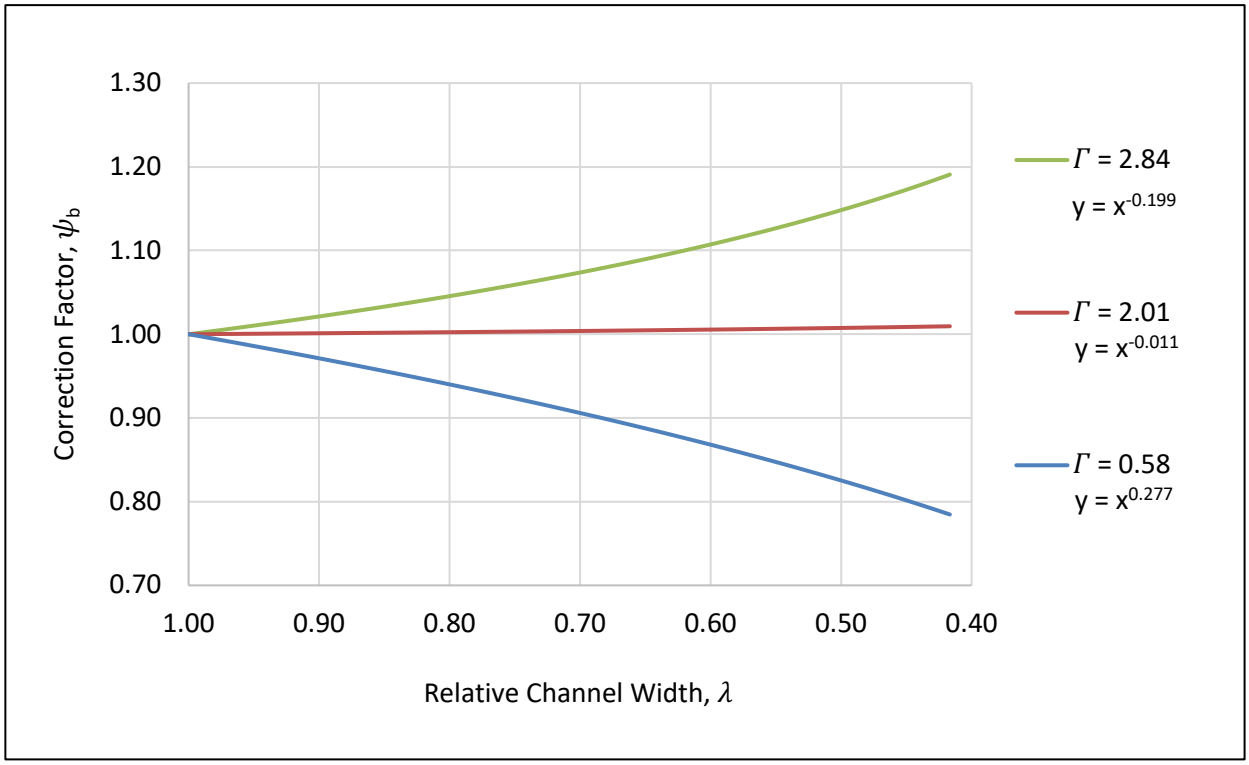

Figure 37. Correction factors for n_b versus relative channel width for tested values of Γ

8.2 Evaluating Estimated Roughness Coefficients for Tested Values of Γ

Relationships presented in Section 8.1 provide a method to estimate prototype values of n_c, n_w, and n_b by applying a correction factor to prototype Manning's *n* values computed using SUFA. This correction is based on empirical relations and is intended to correct SUFA values that would otherwise be relative to a lower prototype channel width, a larger depth, and a lower Froude number. Results presented in this thesis indicate that applicable correction factors vary based on Γ and λ.

Table 14 summarizes prototype-scale Manning's *n* values computed for the 100-year design event (q_p = 244 cfs/ft), and mean Manning's *n* values, averaged over all flowrates evaluated for a given system-wall combination. Each row is given a unique identifier (I.D.). Rows with an I.D. of 'A,' present results from

1:10 scale tests, which correspond to a 50 ft. prototype channel width. Rows with an I.D. of 'B,' present results from 1:10 scale tests with the applicable correction factor ψ applied such that the corrected results correspond to the 120 ft. prototype channel width (here, $\lambda = w_q / w_Q = 50/120$). Rows with an I.D. of 'C,' present results from the 1:24 scale tests, which were adequately modeled at a model width (5 ft.) and length scale ratio (1:24) that directly corresponds to the 120 ft. proposed prototype channel width.

Table 14. Comparison of test results with and without correction factors

Row I.D.	Basis	w (ft.)	q_p (cfs/ft)	ACB bed – smooth walls (Γ = 0.58)			ACB bed – mixed walls (Γ = 2.01)			ACB bed – tangent walls (Γ = 2.84)		
				n_c	n_w	n_b	n_c	n_w	n_b	n_c	n_w	n_b
A	1:10 tests	50	244	0.024	0.017	0.027	0.031	0.041	0.025	0.037	0.055	0.023
			Mean[a]	0.026	0.017	0.030	0.033	0.050	0.026	0.037	0.063	0.022
B	1:10 with ψ	120	244	0.020	0.019	0.021	0.026	0.029	0.025	0.029	0.032	0.028
			Mean[a]	0.022	0.019	0.023	0.027	0.035	0.026	0.029	0.036	0.026
C	1:24 tests	120	244	0.022	0.019	0.023	0.027	0.029	0.027	0.028	0.033	0.027
			Mean[a]	0.022	0.019	0.023	0.027	0.034	0.026	0.029	0.036	0.026

[a] Applicable to the mean value averaged over all flowrates evaluated

The key objective of the present paper is to improve estimates of prototype Manning's *n* obtained using SUFA such that they may be used to estimate prototype Manning's *n* values applicable to the full prototype channel width. To demonstrate the usefulness of these corrections for RPN data, an analysis of the error is summarized in Table 14 presented herein. This is achieved by applying Eq. (23); here δ is the percent error, n_{obs} is the observed (or estimated) value of Manning's *n*, and n_{exp} is the expected (or accepted) value of Manning's *n*. In this case, n_{exp} is determined from the 1:24 scale tests, which accommodated the full prototype channel width. Percent error was computed for two conditions; one in which the correction factor was not applied; and another in which expected results were compared to corrected.

$$\delta = \left|\frac{n_{obs} - n_{exp}}{n_{exp}}\right| * 100\% \quad (23)$$

Table 15 presents the percent error associated with the data presented in Table 14, compared to the expected values as determined from the prototype scale results from the 1:24 scale model. Row I.D. in the n_{obs} column in Table 15 corresponds with the applicable row of comparison in Table 14. The rows with n_{obs} I.D. 'A,' presents the percent error obtained by directly comparing the prototype-scale results from the 1:10 scale model to the prototype-scale results of the 1:24 scale model, thereby not implementing any correction, and thus not accounting for the difference in prototype channel width, depth, and Froude number. While both results are at prototype scale, there is a substantial error associated with not accounting for such a significant difference in prototype channel width (and therefore a relatively small value of λ for the RPN case study). For this comparison, the error associated with n_c is found to increase significantly with increasing Γ. This indicates that the expected error associated with applying SUFA is relatively low in cases in which Γ is small (e.g., testing ACB systems in a flume with smooth walls), and conversely, that error in n_c is relatively high in cases in which Γ is large (e.g., testing systems in a flume with walls that exert a substantial flow resistance).

Table 15. Percent error with and without correction factors

n_{obs} (I.D.)	n_{exp} (I.D.)	q_p (cfs/ft)	ACB bed – smooth walls (Γ = 0.58)			ACB bed – mixed walls (Γ = 2.01)			ACB bed – tangent walls (Γ = 2.84)		
			$\delta(n_c)$	$\delta(n_w)$	$\delta(n_b)$	$\delta(n_c)$	$\delta(n_w)$	$\delta(n_b)$	$\delta(n_c)$	$\delta(n_w)$	$\delta(n_b)$
A	C	244	7.6%	10%	20%	14%	39%	8.5%	33%	68%	13%
		Mean[a]	17%	10%	27%	22%	47%	0.3%	29%	72%	16%
B	C	244	8.2%	1.0%	6.1%	6.4%	2.6%	7.6%	2.5%	2.2%	3.3%
		Mean[a]	0.0%	0.4%	0.1%	0.1%	2.6%	0.7%	0.4%	0.1%	0.1%

[a] Applicable to the mean value averaged over all flowrates evaluated

The rows with n_{obs} I.D. 'B,' present the percent error obtained by comparing the prototype-scale results from the 1:10 scale model, adjusted by the respective correction factor (thus adjusting for the difference in prototype channel width), to the prototype-scale results of the 1:24 scale model. For this comparison, the error associated with mean values of n_c is found to be significantly improved as relates to the direct comparison between row I.D. 'A,' and 'C,' as described previously. Furthermore, in cases in which Γ is large, it is found that δ is drastically reduced for n_c, n_w, n_b, by applying a correction, further indicating the increased need to apply these correction factors at larger values of Γ.

The following figures provide graphical representations of δ comparisons compiled in Table 15. Values of δ without the correction factor pertain to data with a n_{obs} I.D. of 'A.' Values of δ with the correction factor pertain to data with a n_{obs} I.D. of 'B.' Figure 38, Figure 39, and Figure 40 present a comparison of the error associated with Manning's *n* values computed at the 100-year design event for values of Γ = 0.58, Γ = 2.01 and Γ = 2.84, respectively. Figure 41, Figure 42, and Figure 43 present a comparison of the error associated with mean Manning's *n* values computed, for values of Γ = 0.58, Γ = 2.01, and Γ = 2.84, respectively.

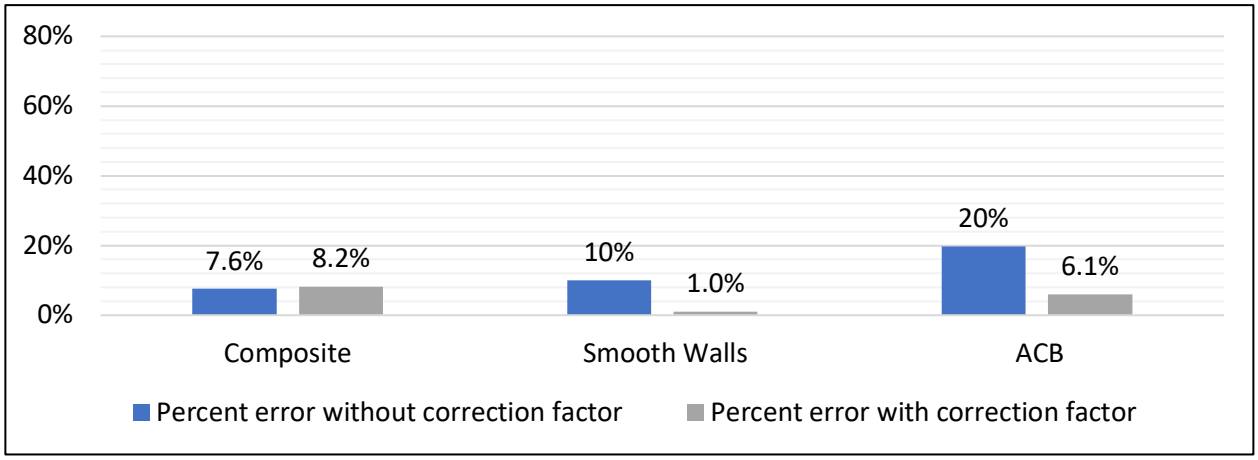

Figure 38. Percent error of Manning's *n* values computed at the 100-year design event for Γ = 0.58

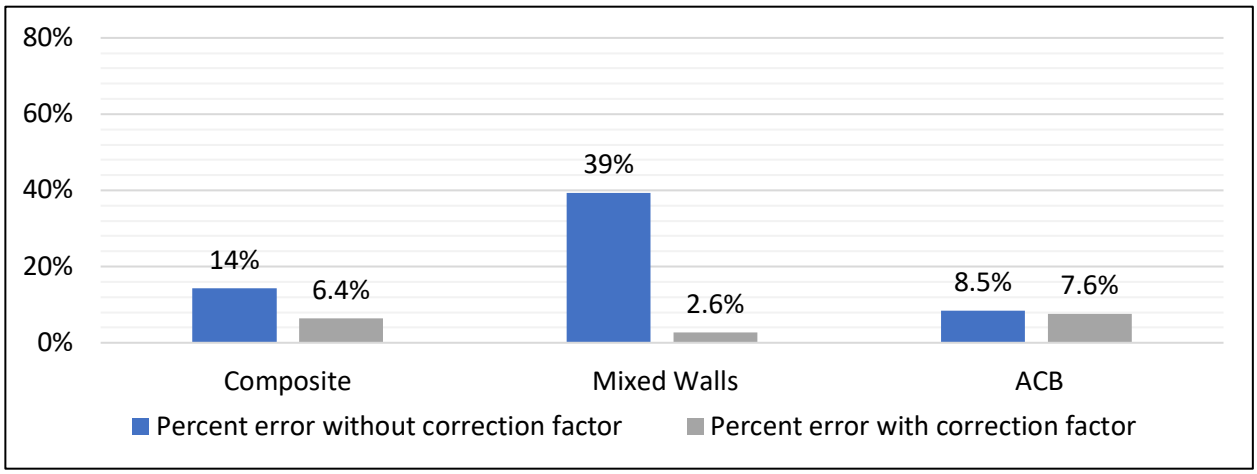

Figure 39. Percent error of Manning's *n* values computed at the 100-year design event for Γ = 2.01

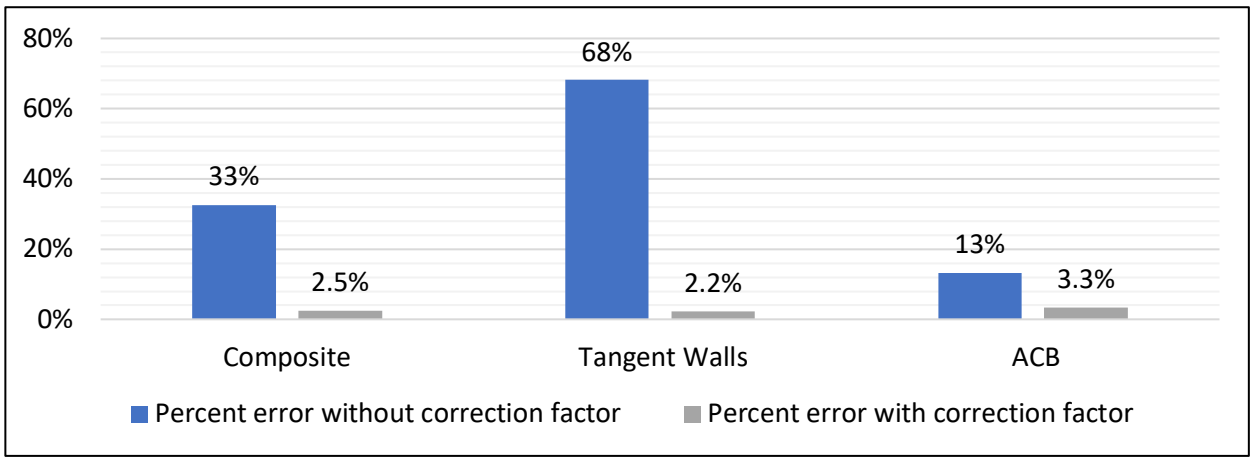

Figure 40. Percent error of Manning's *n* values computed at the 100-year design event for Γ = 2.84

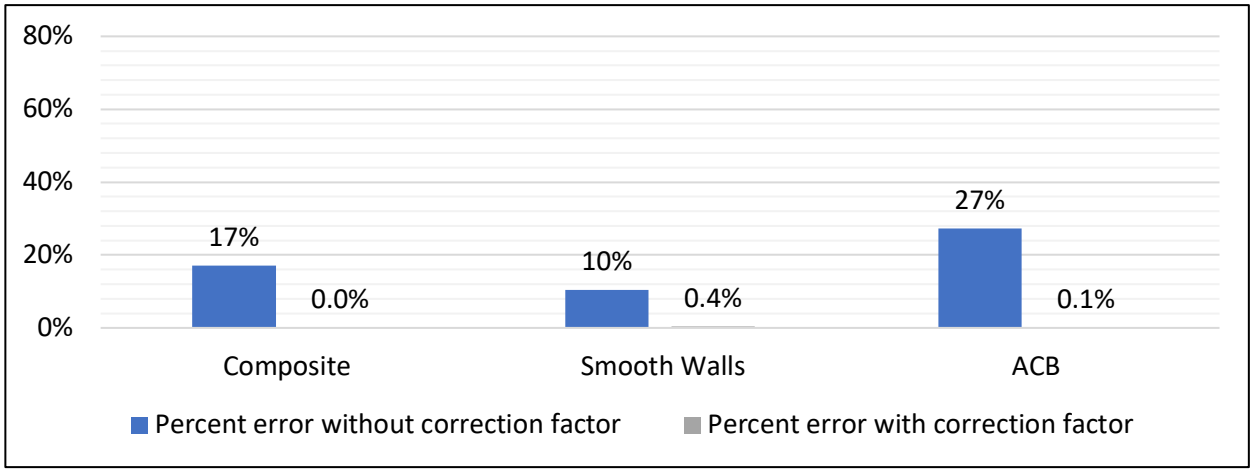

Figure 41. Percent error of mean Manning's *n* values computed over all flowrates for Γ = 0.58

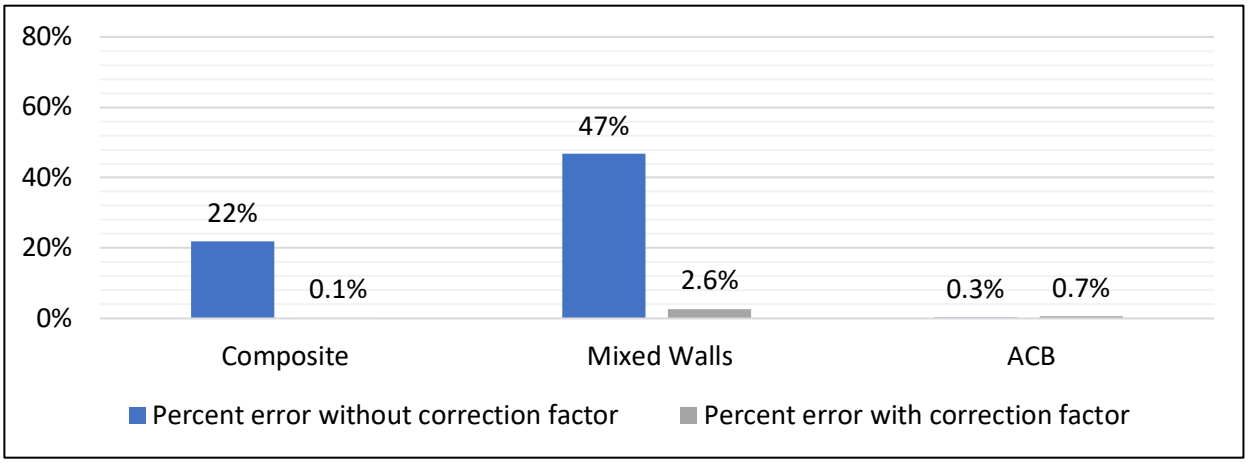

Figure 42. Percent error of mean Manning's *n* values computed over all flowrates for Γ = 2.01

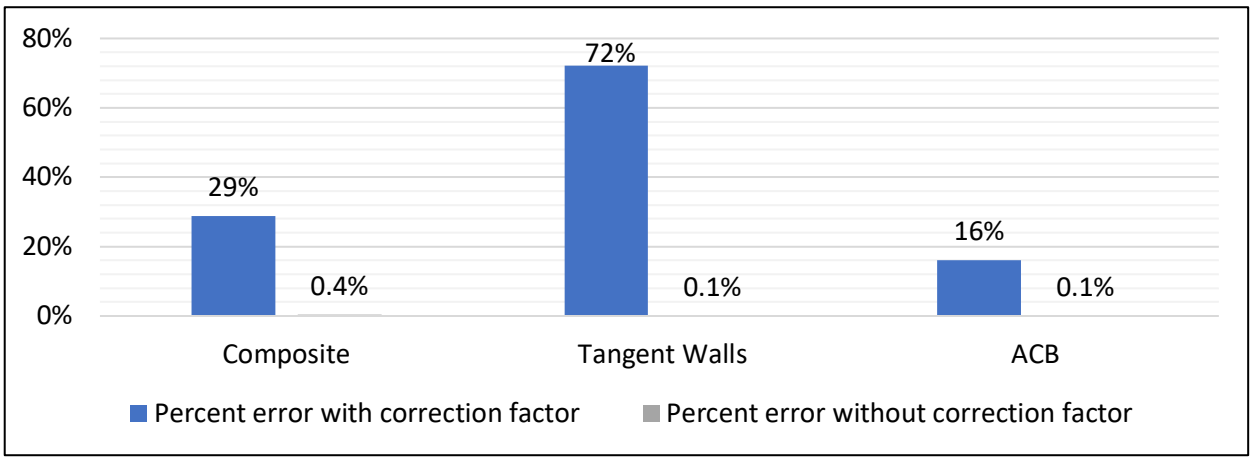

Figure 43. Percent error of mean Manning's *n* values computed over all flowrates for Γ = 2.84

8.3 Estimating Roughness Coefficient Correction Factors for a Range of Γ Values

Power equations for a given value of relative roughness (Γ) fit the general form shown in Eq. (24), relating the correction factor (ψ) to relative channel width (λ) by exponent β.

$$\psi = \lambda^{\beta} \tag{24}$$

Table 16 summarizes values of β obtained from previously provided Figure 35, Figure 36, and Figure 37 for tested values of Γ.

Table 16. Correction factor exponents for tested values of Γ

Relative Roughness $(\Gamma = n_w/n_b)$	Power Equation Exponent (β)		
	Composite (n_c)	Channel Walls (n_w)	Channel Bed (n_b)
0.58	0.181	-0.131	0.277
2.01	0.228	0.409	-0.011
2.84	0.294	0.619	-0.199

Figure 44 presents a graphical representation of Table 16, in which β is plotted against Γ for the predictive relationships of n_c, n_b, and n_w. Second order polynomials were fit to each data set, establishing a method to estimate β or a given value of Γ. The second-order polynomials were then forecasted (extrapolated) a short distance to the nearest value of Γ interval of 0.5, such that ψ may be estimated for all Γ values within the range of Γ = 0.5 to Γ = 3.0 in intervals of 0.5. Table 3 presents estimates of values of β based on the second-order polynomial relationships established in Figure 44 for a range of Γ values from 0.5 to 3.0. These relationships were developed using mean Γ values as shown in Table 16.

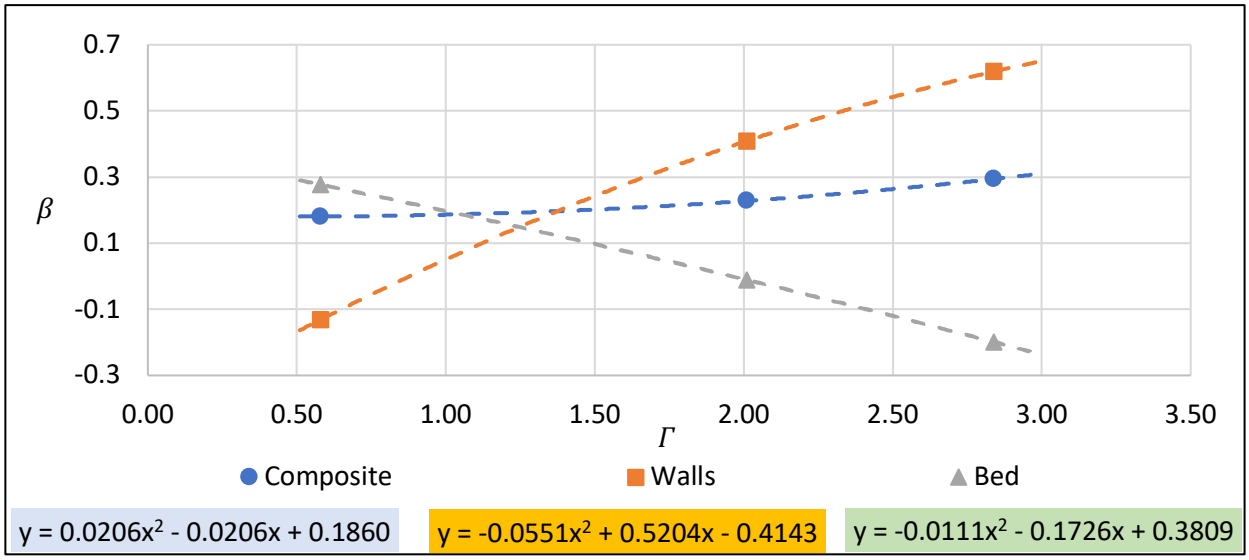

Figure 44. Correction factor exponents for tested values of Γ

Table 17. Estimated β values for a range of Γ values

Relative Roughness ($\Gamma = n_w/n_b$)	Power Equation Exponent (β)		
	Composite (n_c)	Channel Walls (n_w)	Channel Bed (n_b)
0.5[a]	0.181	-0.168	0.292
0.6	0.181	-0.122	0.273
0.7	0.182	-0.077	0.255
0.8	0.183	-0.033	0.236
0.9	0.184	0.009	0.217
1.0	0.186	0.051	0.197
1.1	0.188	0.091	0.178
1.2	0.191	0.131	0.158
1.3	0.194	0.169	0.138
1.4	0.198	0.206	0.118
1.5	0.201	0.242	0.097
1.6	0.206	0.277	0.076
1.7	0.211	0.311	0.055
1.8	0.216	0.344	0.034
1.9	0.221	0.376	0.013
2.0	0.227	0.406	-0.009
2.1	0.234	0.436	-0.031
2.2	0.240	0.464	-0.053
2.3	0.248	0.491	-0.075
2.4	0.255	0.517	-0.097
2.5	0.263	0.542	-0.120
2.6	0.272	0.566	-0.143
2.7	0.281	0.589	-0.166
2.8	0.290	0.611	-0.189
2.9[a]	0.300	0.631	-0.213
3.0[a]	0.310	0.651	-0.237

[a] β values in these rows are calculated based on an extrapolation of the observed data set

Figure 35 presented relationships for correction factor ψ_c for tested values of Γ. Figure 45 improves the applicability of the correction, using the results from the case study to estimate ψ_c as a function of λ over a range of Γ values from Γ = 0.5 to Γ = 3.0 in intervals of 0.5, using the relationships provided in Table 3. This figure highlights that ψ_c decreases with both increasing Γ and decreasing λ. This finding indicates that it becomes increasingly important to apply a correction factor to n_c when Γ is large (walls are significantly rougher than the bed material) and/or when λ is small (SUFA results in a prototype channel width that is significantly smaller than the proposed prototype channel width).

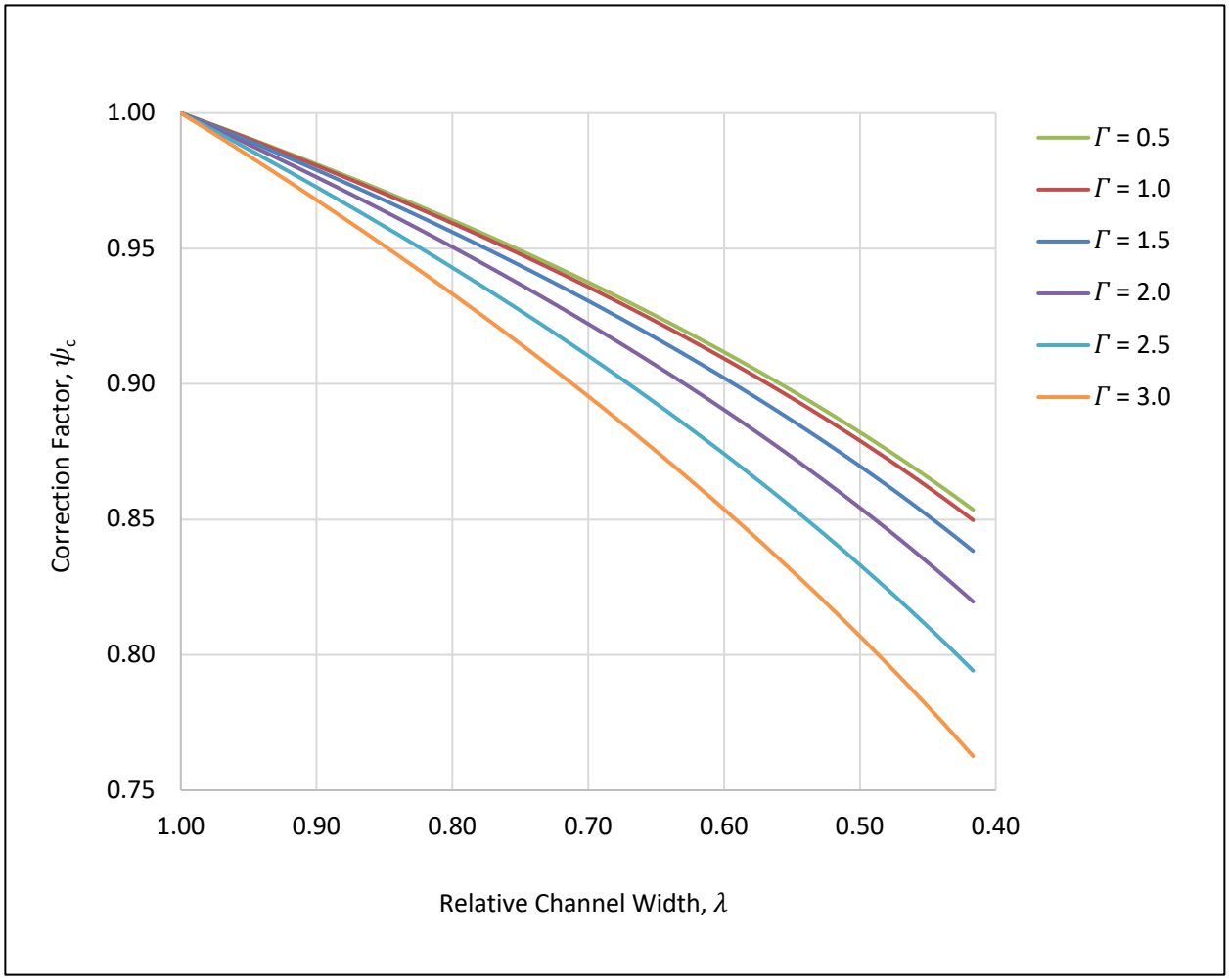

Figure 45. Estimated n_c correction factors for versus relative channel width for a range of Γ values

Figure 36 presented relationships for correction factor ψ_w for tested values of Γ. Figure 46 improves the applicability of the correction, using the results from the case study to estimate ψ_w as a function of λ over a range of Γ values from Γ = 0.5 to Γ = 3.0 in intervals of 0.5, using the relationships detailed in Table 3. The change in sign of the β values listed in Table 3 indicates that when using the SUFA, estimates of n_w are overpredicted ($\psi_w < 1$) when Γ is sufficiently large ($\Gamma \geq 0.9$) and underpredicted ($\psi_w > 1$) when Γ is sufficiently small ($\omega \leq 0.8$). Furthermore, Figure 46 illustrates that it becomes increasingly important to apply a correction factor to n_w at smaller values of λ, where w_q increasingly deviates from w_Q.

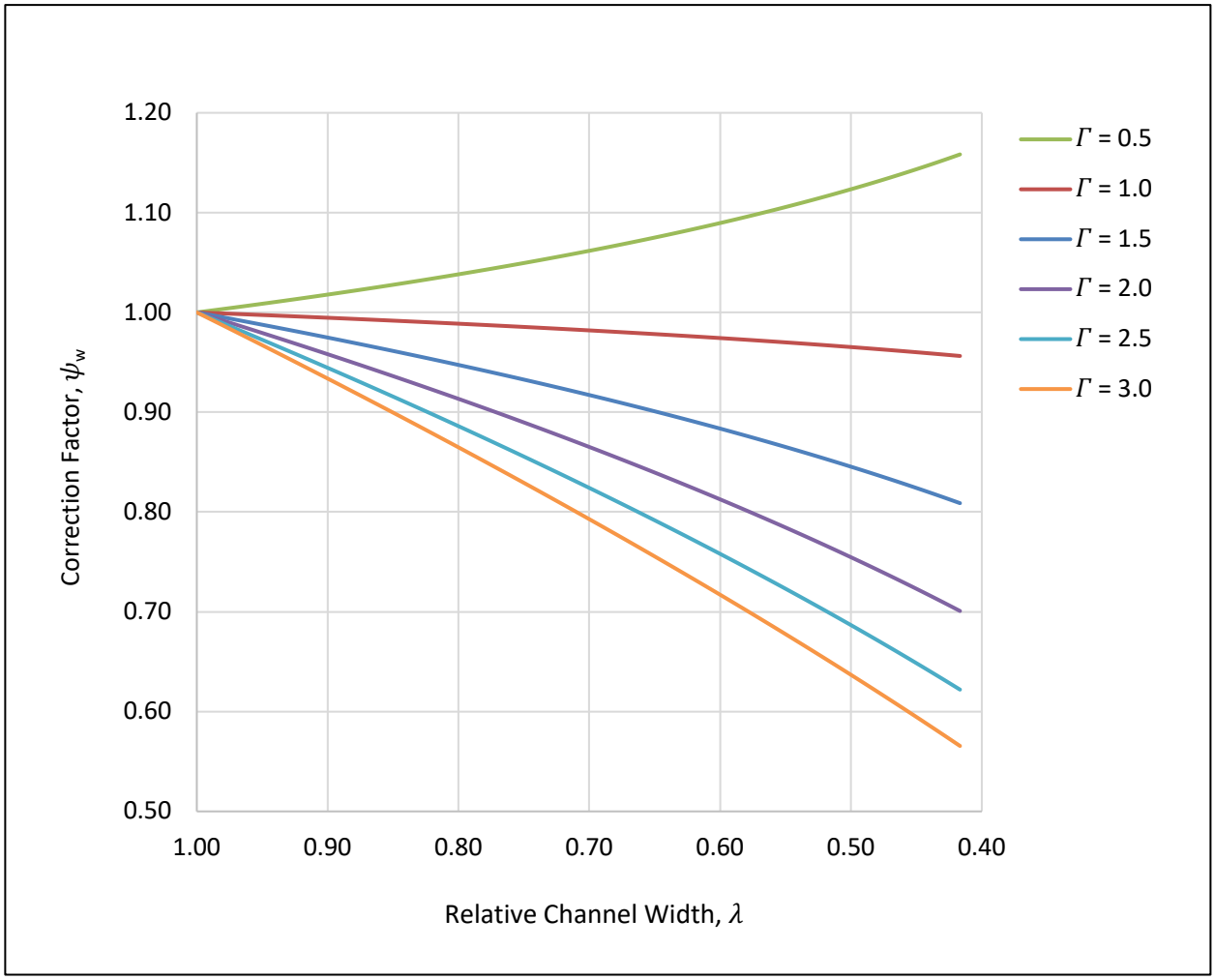

Figure 46. Estimated n_w correction factors for versus relative channel width for a range of Γ values

Figure 37 presented relationships for correction factor ψ_b for tested values of Γ. Figure 47 improves the applicability of the correction, using the results from the case study to estimate ψ_b as a function of λ over a range of Γ values from Γ = 0.5 to Γ =3.0 in intervals of 0.5, using the relationships detailed in Table 3. The change in sign of the β values listed in Table 3 indicates that when using the SUFA, estimates of n_b are overpredicted ($\psi_w < 1$) when Γ is sufficiently small ($\Gamma \leq 1.9$) and underpredicted ($\psi_b > 1$) when Γ is sufficiently large ($\Gamma \geq 2.0$). Furthermore, Figure 47 illustrates that it becomes increasingly important to apply a correction factor to n_b at smaller values of λ, where w_q increasingly deviates from w_Q.

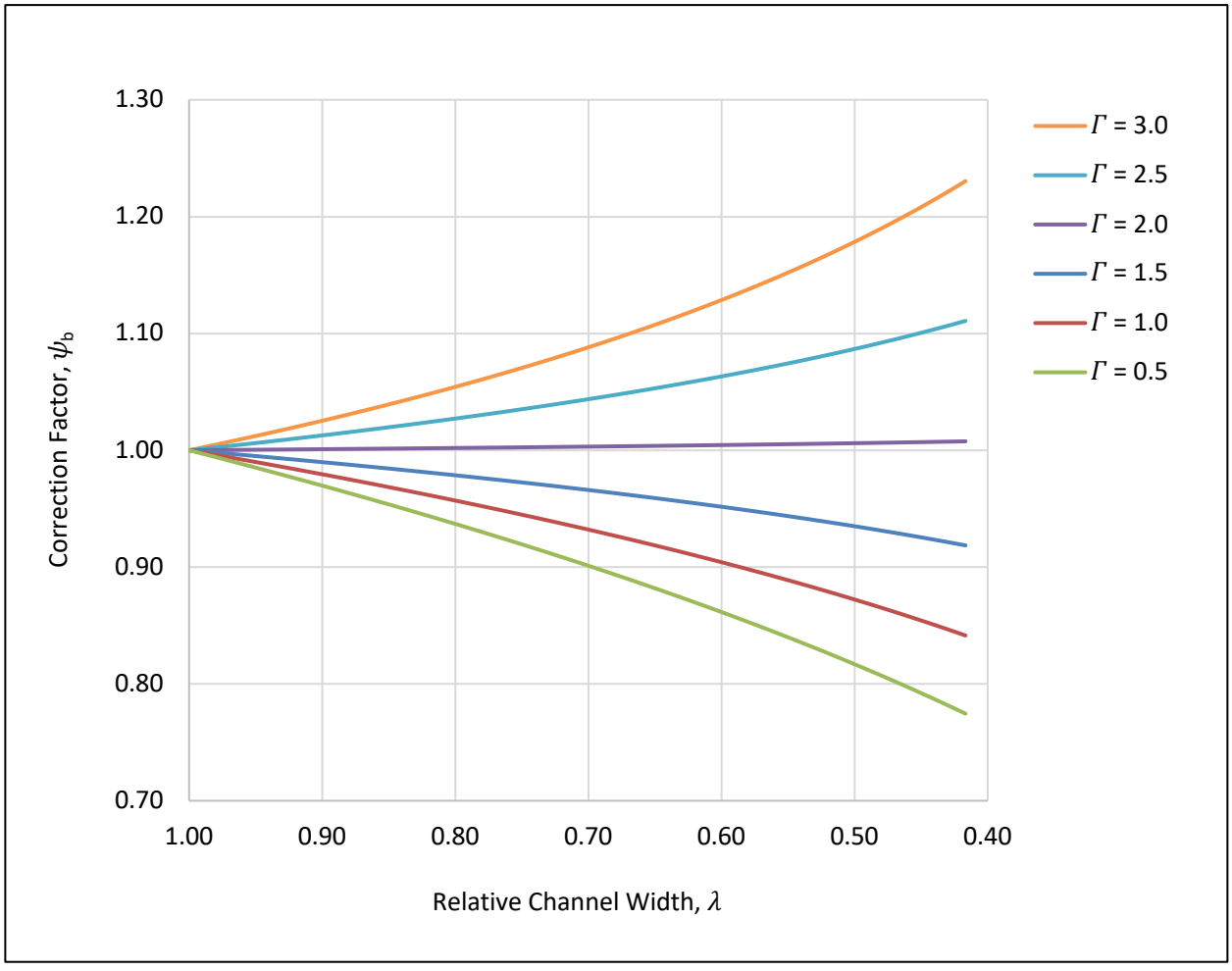

Figure 47. Estimated n_b correction factors for versus relative channel width for a range of Γ values

8.4 Example Application of Correction Factors

Application of the flow resistance correction factors presented in this thesis is described by the following theoretical example: a physical model was proposed to evaluate the flow resistance, characterized as Manning's *n*, for a 200-foot-wide rectangular prototype channel. The available flume at the laboratory was a 5-food-wide flume within the assembled model. At the request of project partners, and to mitigate potential scale effects and magnification of instrumentation and measurement errors, it was desirable to develop a Froude-scaled physical model at a length-scale factor no larger than 20. However, directly modeling the 200-foot-wide channel prototype channel in the 5.0 ft. wide flume would result in a length-scale factor of 40. Therefore, the SUFA was implemented for a length-scale factor of 20. A 5.0 ft. wide flume at a length-scale factor of 20 results in a 100 ft. wide channel evaluated using the SUFA. A channel width of this magnitude results in $\lambda = w_q/w_Q$ = 100 ft. / 200 ft. = 0.5, which is within the bounds of λ evaluated in this thesis ($0.42 \leq \lambda \leq 1.0$). At a specified design discharge, a value of n_c = 0.041 was computed using analysis methods presented in Section 5. Eq. (17) was then used to estimate values of n_w = 0.048 and n_b = 0.032. Therefore, $\Gamma = n_w/n_b$ = 0.048 / 0.033 = 1.5, which is also within the bounds of Γ presented in this thesis ($0.5 \leq \Gamma \leq 3.0$).

To correct estimates of n_c, the applicable row in Table 17 for Γ = 1.5 is consulted, indicating that by Eq. (24), $\psi_c = \lambda^\beta = 0.5^{0.201} = 0.87$. Therefore, by Eq. (20), $n_{c,Q} = \psi_c n_{c,q}$ = (0.87)(0.041) = 0.036. To correct estimates of n_w, Table 17 for Γ = 1.5 is again consulted, indicating that by Eq. (24), $\psi_w = \lambda^\beta = 0.5^{0.242} = 0.85$. Therefore, by Eq. (21), $n_{w,Q} = \psi_c n_{w,q}$ = (0.85)(0.048) = 0.041. To correct estimates of n_b, Table 17 for Γ = 1.5 is then again consulted, indicating that by Eq. (22), $\psi_b = \lambda^\beta = 0.5^{0.097} = 0.93$. Therefore, by Eq. (22), $n_{b,Q} = \psi_c n_{b,q}$ = (0.93)(0.033) = 0.031. ψ_c, ψ_w, and ψ_b could also have been estimated based on Figure 45, Figure 46, and Figure 47, respectively.

9 IMPLICATIONS FOR RIO PUERTO NUEVO

The RPN project's main objective was to provide 100-year flood hazard mitigation to areas adjacent to the Rio Puerto Nuevo floodplain. Additional objectives for the project included facilitating a minimum of 2 ft. of freeboard at bridge crossings, supporting a subcritical flow regime along the project reach, and mitigation of scour along the channel bed.

A concrete SPS comprised the proposed channel bed. Prototype channel walls were specified as 6-foot diameter concrete drilled shaft tangent piles. This unique channel geometry caused unknown flow resistance behavior and therefore required investigation. Two physical hydraulic model studies were conducted to aid the estimation of flow resistance and other hydraulic parameters of interest needed to evaluate the hydraulic performance within the scope of established design criteria for various scour protection system alternatives in a straight flume. Though outside the scope of the research described here, subsequent stages of the RPN Project used the selected scour protection system determined by this research to evaluate performance at the reach scale, which included local geometric complexities within the project reach such as channel width contractions and bends in the channel alignment.

Two model scales were evaluated to investigate an association between Manning's *n* and channel width. Flow resistance exerted by the geometry of the tangent walls was found to exert a significant influence on composite flow resistance values, particularly at the narrower prototype channel width applicable to the SUFA (1:10) model. Results indicated that the SUFA used by the 1:10 model scale resulted in an estimation of prototype n_c values that exceeded those computed for the full design channel width. The supplemental model scale was necessary to accommodate the full prototype design channel width and resulted in a substantial decrease in estimated flow resistance values.

Design criteria for the project specify that the lined channel facilitates acceptable hydraulic performance at a 100-year recurrence flowrate of 29,300 cfs in a 120.0-foot-wide design channel cross-section. At this flow event, the proposed channel requires a composite roughness, characterized as Manning's *n*, of 0.025 to 0.030, and a Froude number less than or equal to 0.80. A maximum composite Manning's *n* of 0.035 and Froude number of 0.85 may be accommodated, though values of this magnitude may pose manageable difficulties within the project reach.

The 1:10 scale model resulted in a 50 ft. prototype channel width. The results for this model indicated that the wet-cast ACB SPS did not meet the n_c criterion set for the proposed channel conveying the 100-year design flow. For that flow, the composite prototype Manning's roughness coefficient computed for System B was found to be n_c = 0.037. A value of this magnitude did not meet the design criterion set for the project reach specified in Table 2 (i.e., the maximum value of $n_c \leq 0.035$) and would have precluded the wet-cast ACB SPS from consideration. However, results from the 1:24 scale model (n_c = 0.028 at the 100-year design flow, a 32% reduction), simulating the full 120 ft. width of the prototype channel, were found to satisfy the project design criterion. This finding highlights why, for the present study, the 1:24 scale model, or a means of correcting from SUFA results, was needed.

The 1:24 scale model was used to evaluate Manning's roughness coefficient for the full 120 ft. prototype design channel width. For a design condition consisting of the 100-year discharge in the 120 ft. wide channel, this model resulted in a Froude number of Fr = 0.78 and n_c = 0.028. These results met the target design constraints listed in Table 2, which specify a target $\mathrm{Fr} \leq 0.80$, and a target n_c of $0.025 \leq n_c \leq 0.030$. Therefore, the wet-cast ACB SPS satisfied Manning's *n* design criterion for the 120 ft. design channel width.

Due to the two model scales, flow resistance values were estimated at two prototype channel widths. Results from these two models were used to develop a relationship to estimate Manning's roughness coefficient as a function of channel width. Figure 48 presents these results, specific to the 100-year flow applicable to the proposed channel's design, providing insights regarding the anticipated variability of n_i and n_c with channel width, which is proposed to fluctuate from 95 ft. to 150 ft. along the project reach. Additional details about the development of this figure, and the associated figures presented previously, are available in Section 7.4.

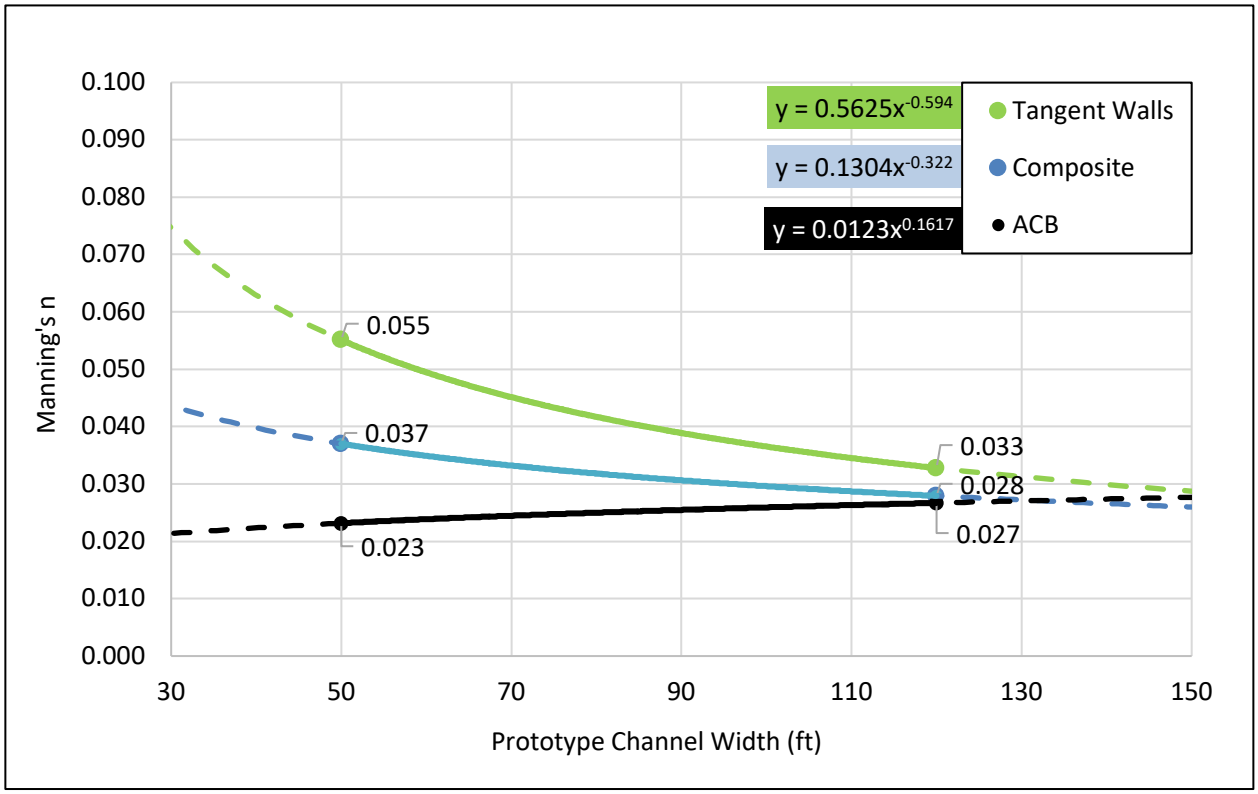

Figure 48. Prototype values of n_i and n_c versus channel width at the 100-year design event

The tangent walls and ACB channel bed lining components were found to have variable contributions to the resulting value of n_c for the channel. For the 100-year design condition in the 1:10 model, the tangent walls were found to have a much larger Manning's n (n_w = 0.055), compared to

Manning's *n* for the ACB-lined bed (n_b = 0.023). For the 100-year design condition in the 1:24 model, the tangent walls were found to have a prototype value of Manning's *n* (n_w = 0.033), compared to Manning's *n* for the ACB-lined bed (n_b = 0.027). This outcome, in which channel walls exerted greater resistance to flow than the channel bed, was reasoned to contribute to the increased values of n_c found in the model that constituted a narrower prototype channel width.

9.1 Waves

Waves were observed in multiple tests, as shown graphically by the water-surface profiles in Appendix E. Of particular interest were wave heights observed at the design condition (100-year flow event, tangent walls) for the potential SPS candidates (Systems B and D). Excessive wave heights have the potential to reduce clearance at bridge crossings below the freeboard estimates provided in Section 9.2. Freeboard estimates employed water-surface profile trendlines, thus dampening the effect of waves along the profile. Representative wave heights applicable to System B and System D were estimated as 0.70 ft. and 0.48 ft. at the prototype scale, respectively.

9.2 Bridge Freeboard

Six bridges were identified along the project reach as shown in Figure 1. Bridge names, locations, low chord elevations, proposed channel bed elevations, and estimates of freeboard are summarized in Table 18. Channel bed elevations reflect the elevation of the proposed channel at the upstream face of each bridge and were extracted from the USACE 60% design plan set dated October 2022 (CDM Smith, 2022). Low-chord elevations were provided directly by USACE officials and reflect the strut elevations for the Northeast (NE) and Southeast (SE) Ramp bridges, as recommended by USACE. For each bridge

crossing, the required freeboard at the 100-year design event is 2.0 ft. However, 3.0 ft. was specified as the target clearance.

Table 18. Estimates of RPN bridge freeboard

Bridge Name	Bridge Number	Station[a] (ft.)	Low Chord Elevation (ft.)	Channel Bed Elevation[a] (ft.)	Water-Surface Elevation (ft.)	Freeboard (ft.)
Los Américas	1	158+00	17.25	-5.6	8.88	8.4
NE Ramp	2	164+05	15.30	-4.1	10.3	5.0
Piñero	3	169+55	16.69	-2.8	11.7	5.0
SE Ramp	4	174+65	18.50	-1.6	12.9	5.6
Notre Dame	5	195+93	25.46	3.5	18.0	7.5
Pedestrian	6	196+77	25.46	3.7	18.2	7.3

[a] measured at the upstream bridge face along the centerline of the channel

An approximation of the longitudinal profile of the proposed project reach is provided in Figure 49 using the low chord, channel bed, and WSE reported in Table 18. Estimates indicate that the proposed channel results in the bridge crossings passing the 100-year event with a freeboard of 5.0 ft. or larger. However, these estimates do not account for WSE variations due to geometric fluctuations in the channel, superelevation due to bends in the alignment, or potential wave heights as summarized in Section 9.1. These elements may result in reductions in freeboard beyond the estimates reported in Table 18.

This estimate of freeboard was measured at the upstream bridge opening using a one-dimensional analysis, with no variation in WSE at a given cross-section. In practice, however, freeboard is commonly measured from the low-chord elevation of the bridge superstructure to the highest point in the WSE at a cross-section located upstream of any contraction region caused by the structure. Alternate measuring techniques such as this may be more conservative than the estimates listed in Table 18. Super-elevation of the water surface due to bends, backwater effects caused by channel constrictions, the potential for

standing waves, and other factors, all may contribute to further limitations on freeboard in the prototype channel. Furthermore, due to the relatively short flume length (40 ft.), flow uniformity was not obtained within the subject model. Therefore, due to the influence of the boundary condition, water depths may be subject to change for the prototype channel.

This estimate serves as a preliminary check on bridge capacity. Flow resistance results from this stage of the RPN analysis were used to calibrate a Flow-3D model produced by AECOM. Additional insights regarding bridge capacity and the other design criteria elements for the proposed RPN channel were evaluated using the calibrated Flow-3D model as an effort outside the scope of the present RPN study discussed.

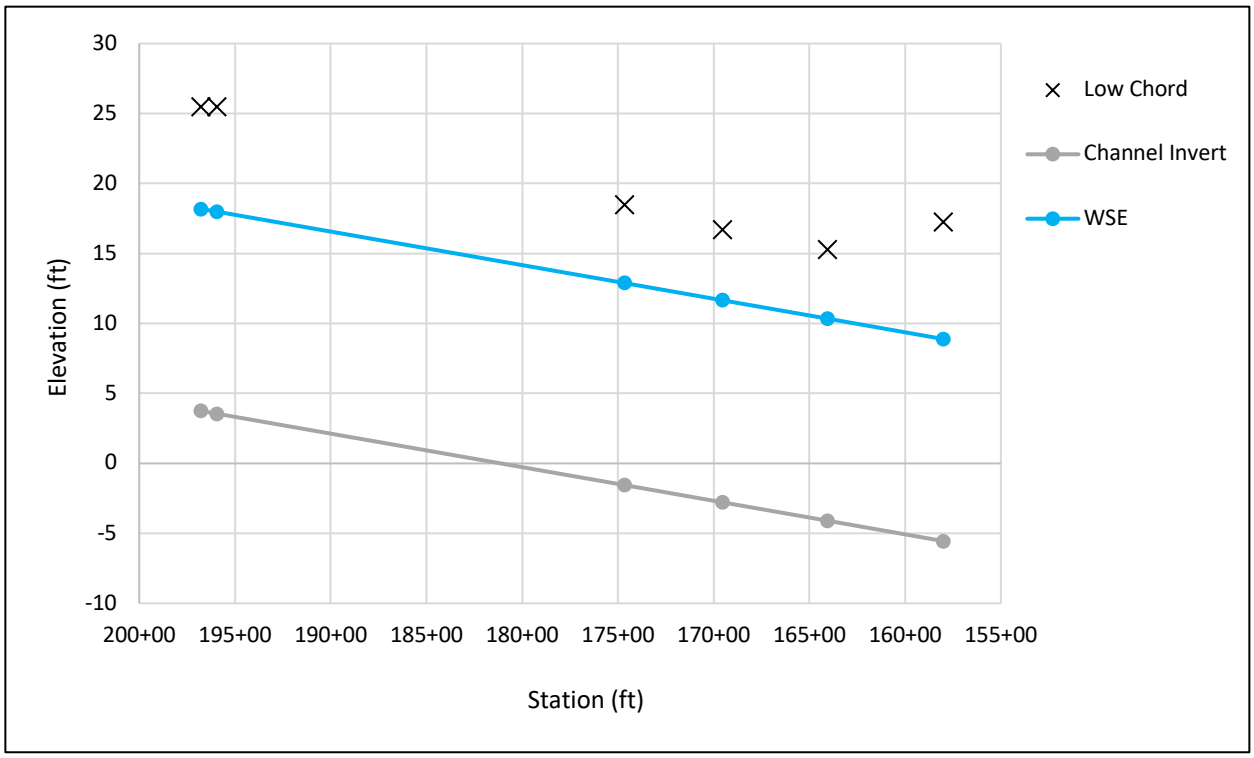

Figure 49. Longitudinal profile of the RPN channel with bridge low chord elevations

10 CONCLUSIONS

The findings presented in this research indicate that applying a scaled unit flowrate physical modeling approach (SUFA) can result in inflated estimates of flow resistance, characterized as Manning's *n*. The secondary model of the Rio Puerto Nuevo (RPN) channel was essential to the success of the project, as without the secondary model, or means of correcting flow resistance estimates from the SUFA model, the articulated concrete block channel lining would not have met established project design criteria. The correction factors presented are shown to reduce estimates of n_c (composite Manning's *n*) obtained from the RPN SUFA model as much as 29%. The two models developed for this project formed the basis for which future flow resistance estimates derived from SUFA models may be corrected. The correction procedure presented in this thesis addresses a gap in the body of existing literature regarding empirical relations of flow resistance in open-channel flows.

Two physical models were built to evaluate the proposed PRN channel. The use of two model scales enabled the estimation of the flow resistance to be assessed at two channel widths. Replication of the 120 ft. design channel width of the channel was facilitated by the 1:24 model, though not by the 1:10 model (M:P). A relationship, developed using data from two models developed at different length-scale factors, provided insights on the variability of n_c with channel width, which changes along the project reach from 95 ft. to 150 ft. As a supplemental effort beyond the scope of the RPN project, two other wall boundary element conditions were evaluated to investigate the impact of variable flow resistance exerted by channel sidewalls. A comparative analysis of the two models, for which three sidewall conditions were evaluated, provided the basis for a case study evaluation of flow resistance estimates derived from unit flow rate models.

The relationships developed for RPN yielded insights regarding flow behavior for channels at variable widths, though with the same unit flowrate, and the associated dependence on the relative flow resistance exerted by wall and bed channel boundary elements. The use of the 1:10 scale results on the RPN project, at which there was a relatively large Γ (relative roughness, given by the ratio of Manning's *n* of the wall boundary n_w, to the Manning's *n* of the channel bed boundary n_b), and small λ (relative channel width, given by the ratio of prototype channel width evaluated using the unit flow rate modeling approach, to the design prototype channel width), would have resulted in the ACB SPS (articulated concrete block scour protection system) being precluded from consideration due to n_c values exceeding the specified design criteria. Conducting the 1:24 scale model allowed the full prototype channel width to be modeled and resulted in the ACB SPS meeting project constraints. Therefore, the wet-cast ACB SPS was recommended for continued evaluation on the RPN project.

Findings presented in this thesis indicate that, when using SUFA, estimates for flow resistance need to be corrected to accurately reflect prototype channel conditions applicable to the full channel width. Comparative results from the two models indicate that the SUFA results in larger prototype flow depths, smaller estimates of Froude number, and larger estimates of n_c. Additionally, findings indicate that it becomes increasingly important to apply a correction factor to n_c when Γ is large (walls exert a more significant impact on flow resistance than the bed material) and/or when λ is small (SUFA results in a prototype channel width that is significantly smaller than the proposed prototype channel width). Furthermore, findings indicate that it increasingly important to apply a correction factor to n_w and n_b at lower values of λ.

Future research can build on this body of work presented in this thesis by expanding the dataset for which correction relationships were developed, thereby increasing the applicability to a wider range of

prototype channels. This could include larger variations in channel width ($\lambda < 0.42$), or relative roughness values below ($\Gamma \leq 0.5$) or above ($\Gamma \geq 3.0$) the range evaluated in this thesis. Additionally, the corrections presented could be improved by the inclusion of Reynolds-number scale effect considerations, decomposition of flow resistance components, or the development of relative roughness estimates based on roughness element height for specific boundary elements. Correction factors for n_w and n_b may be improved by evaluating model results using alternate computation methodologies, such as deviating from the Horton method to estimate n_w and n_b for individual roughness elements. Furthermore, it would also be useful to establish correction factors for depth and velocity derived from unit flowrate physical models, as these parameters are of particular interest in most hydraulic model applications.

A scaled unit flowrate physical modeling approach is a tool that facilitates the minimization of the length-scale factor for a given model. Minimization of length-scale factor is an important consideration in the development of a physical model given constraints imposed by the width of available laboratory facilities, precision capabilities of model production equipment, the desire to minimize scale-effects and error magnification. Future physical models concerned with flow resistance may use the results of this research to better understand and correct estimates of flow resistance derived from physical models using SUFA. Correction factors are presented for a range of relative channel width values from approximately 0.4 to 1.0, and a range of relative roughness values from approximately 0.5 to 3.0. Future SUFA models with relative channel widths and relative flow resistance values within the specified ranges evaluated in this research may use the presented correction method to improve estimates of flow resistance, characterized as Manning's *n*, for individual channel elements and flow resistance specific to the composite channel.

REFERENCES

Aqueel, Al-Adili. (2016). Investigation of the effect of Manning roughness on Froude number in subcritical flow. *Journal of Construction and Building Material*. doi:01(01:39-51)

Carrasco, C. (2019, October 3). *Corps awards dredging contract for Rio Puerto Nuevo Flood Control Project in San Juan, Puerto Rico*. Retrieved from US Army Corps of Engineers, Jacksonville District Website: https://www.saj.usace.army.mil/Media/News-Releases/Article/1979792/corps-awards-dredging-contract-for-rio-puerto-nuevo-flood-control-project-in-sa/

CDM Smith. (2022, October). Rio Puerto Nuevo Project Contract 4: Modification of the Four Las Americas Over Rio Piedras and Rio Puerto Nuevo Channel Improvements from Station 147+40 to Station 175+90 San Juan, Puerto Rico. *60% Submittal*.

Chanson, H. (2004). Chapter 14: Physical Modeling of Hydraulics. In *The Hydraulics of Open Channel Flow: An Introduction* (pp. 261-279). London, UK: Butterworth Heinemann.

Cheng, N.-S. a. (2005). Comparisons of sidewall correction of bed shear stress in open-channel flows. *Journal of Hydraulic Engineering, 131*(7), 605-609. Retrieved from https://doi.org/10.1061/(asce)0733-9429(2005)131:7(605)

Chow, V.T. (1959). Open Channel Hydraulics. New York, NY: McGraw-Hill.

Contech, E. S. (2023). Armourflex Cellular Concrete Block. Greenwood Village, CO.

Deya, L. (2022, May 13). *Rio Puerto Nuevo – Moving Forward with Innovated Proposed Channel*. Retrieved from US Army Corps of Engineers, Jacksonville District Website: https://www.saj.usace.army.mil/Media/News-Stories/Article/3030732/rio-puerto-nuevo-moving-forward-with-innovated-proposed-channel/

Julien, P. Y. (2010). *Erosion and Sedimentation* (2 ed.). Cambridge, UK: Cambridge University Press.

Morgan, S. C. (1999). *Hydraulic Stability of Cable Concrete Revetment System During Overtopping Flow.* Minneapolis, Minnesota: St. Anthony Falls Laboratory, University of Minnesota.

NECA. (2023). Cable Concrete. Farmington, NM.

Nikora, V. I. (2019). Friction factor decomposition for rough-wall flows: Theoretical background and application tyo open-channel flows. *Journal of Fluid Mechanics, 872*, 626-664. Retrieved from https://doi.org/https://people.eng.unimelb.edu.au/imarusic/publications/Edited%20Papers%202019/Nikora_JFM-2019-Friction%20Factor.pdf

Pinto, T. (2020). *Scaling Issues in Hydraulic Modelling*. Retrieved from World Register of Introduced Marine Species: www.coastalwiki.org/introduced/wiki/Scaling_Issues_in_Hydraulic_Modelling

SimScale. (2023, August 11). *What is Reynolds Number?* . Retrieved from SimScale: https://www.simscale.com/docs/simwiki/numerics-background/what-is-the-reynolds-number/

Sturm, T. W. (2001). *Open Channel Hydraulics* (Third ed.). McGraw-Hill.

Thornton, C. I. (2018). *Hydraulic Testing Report for Shoreblock EPEC SD-475 OCT Articulating Concrete Block System.* Fort Collins, Colorado: Colorado State University and Shoretec, LLC.

USACE. (2022, October). Río Puerto Nuevo Flood Control Project: Hydraulic Design Considerations & Physical Model Kickoff. USACE - Jacksonville District.

USACE. (2022). *Statement of Work for General Model of the Proposed Puerto Nuevo Rectangular Channel.* Retrieved June 14, 2022

USACE. (2023). *Rio Puerto Nuevo Flood Damage Reduction Project*. Retrieved from US Army Corps of Engineers, Jacksonville District Website: https://www.saj.usace.army.mil/About/Divisions-Offices/Antilles-Office/Rio-Puerto-Nuevo/

Webb et al., C. B. (2011). Scale effects in physical hydraulic engineering models. *Journal of Hydraulic Research 49:3*, 293-306.

APPENDIX A

Supplemental Slideshow


Unit Flowrate
Physical Models

Q
flowrate
(volumetric discharge)

q
unit flowrate
(flowrate per unit length of channel width)

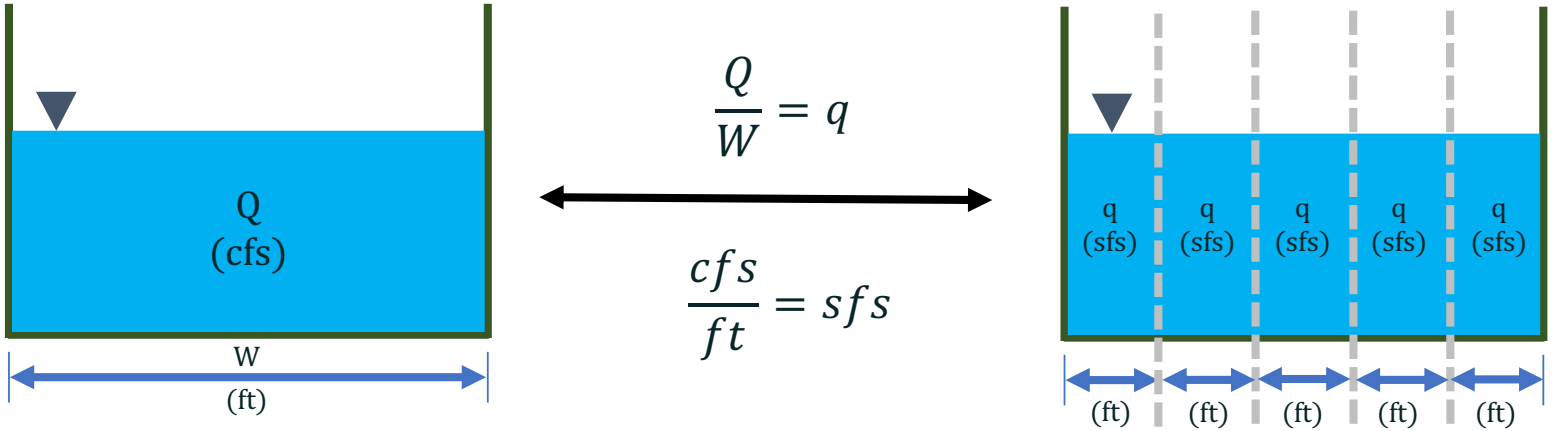

Q = flowrate (cfs); W = channel width; q = unit flowrate

Prototype Channel

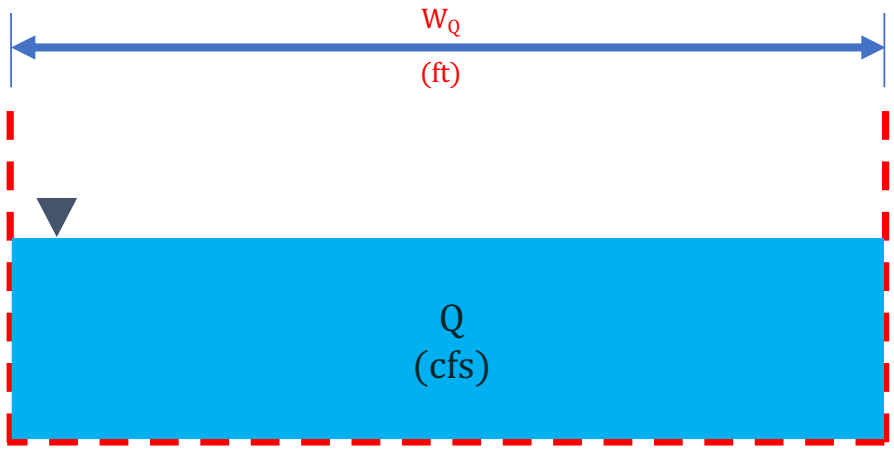

Parameters:

- Q = flowrate
- W_Q = prototype channel width

Unit Flowrate

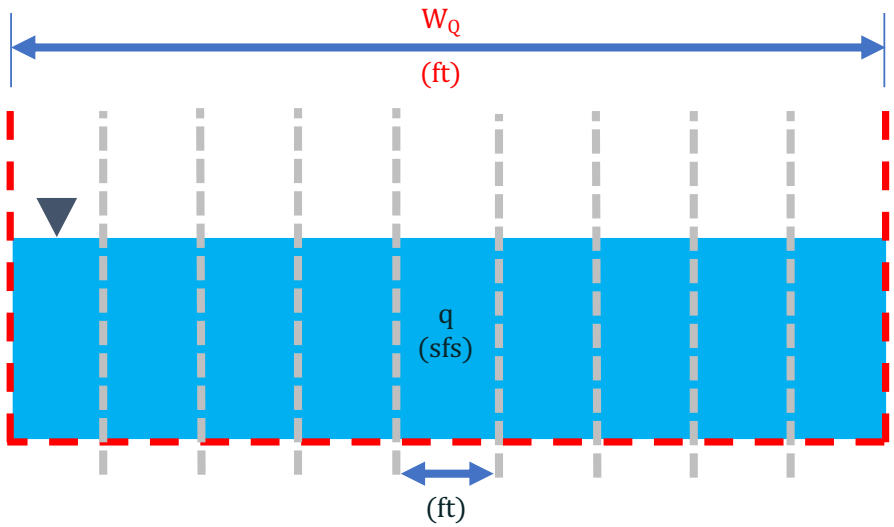

Parameters:

- Q = flowrate
- W_Q = prototype channel width
- $q = Q/ W_Q$ = unit flowrate

Prototype Channel Width Modeled

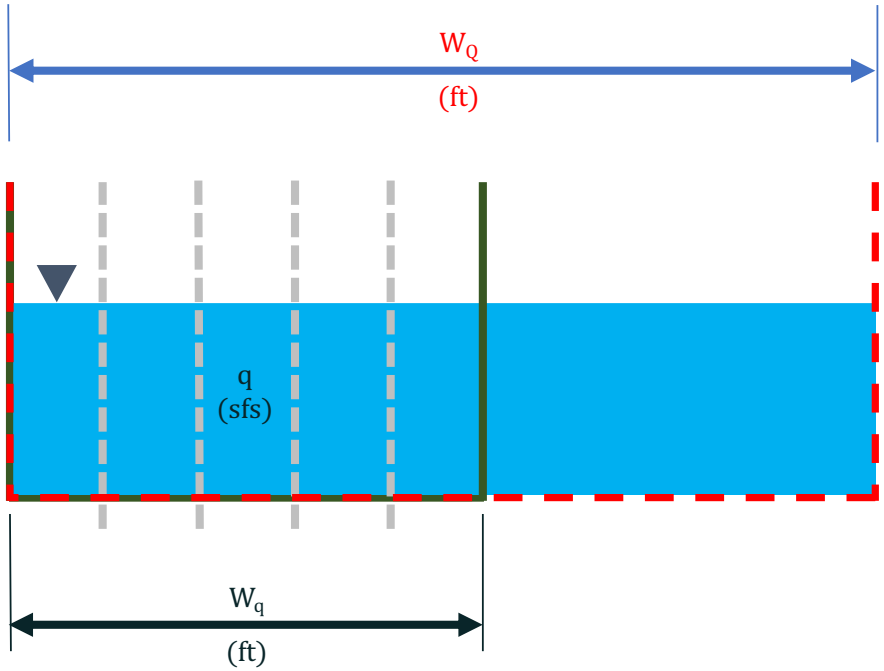

Parameters:

- Q = flowrate
- W_Q = prototype channel width
- q = Q/ W_Q = unit flowrate
- W_q = prototype channel width modeled using q

$$W_q < W_Q$$

Modeled width — Prototype width
Unit flow rate — Total flowrate

Flow Depth

$Y_q > Y_Q$

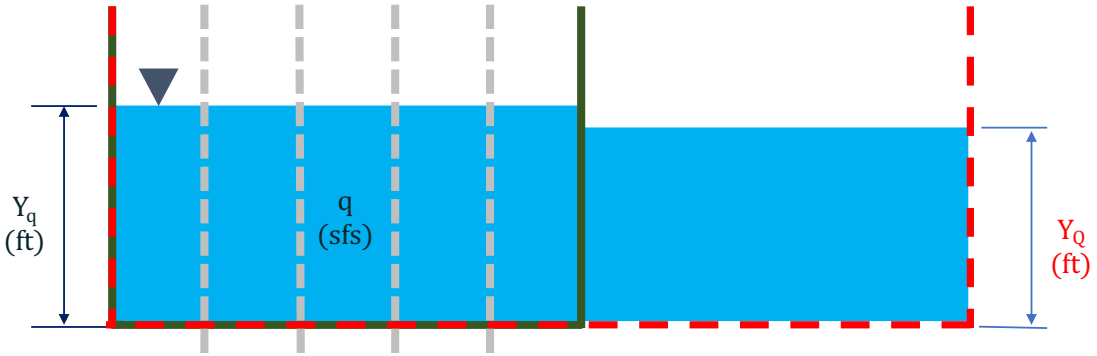

Recall: $W_q < W_Q$

Parameters:

- Q = flowrate
- W_Q = prototype channel width
- $q = Q/W_Q$ = unit flowrate
- W_q = prototype channel width modeled using q
- Y_Q = prototype flow depth
- Y_q = prototype flow depth modeled using q

Froude Number

$FR_q < FR_Q$

$$Fr = \frac{V}{\sqrt{gY}} = \frac{Q}{Y^{1.5}W\sqrt{g}}$$

Recall:

- $W_q < W_Q$
- $Y_q > Y_Q$
- $Fr_m = Fr_p$

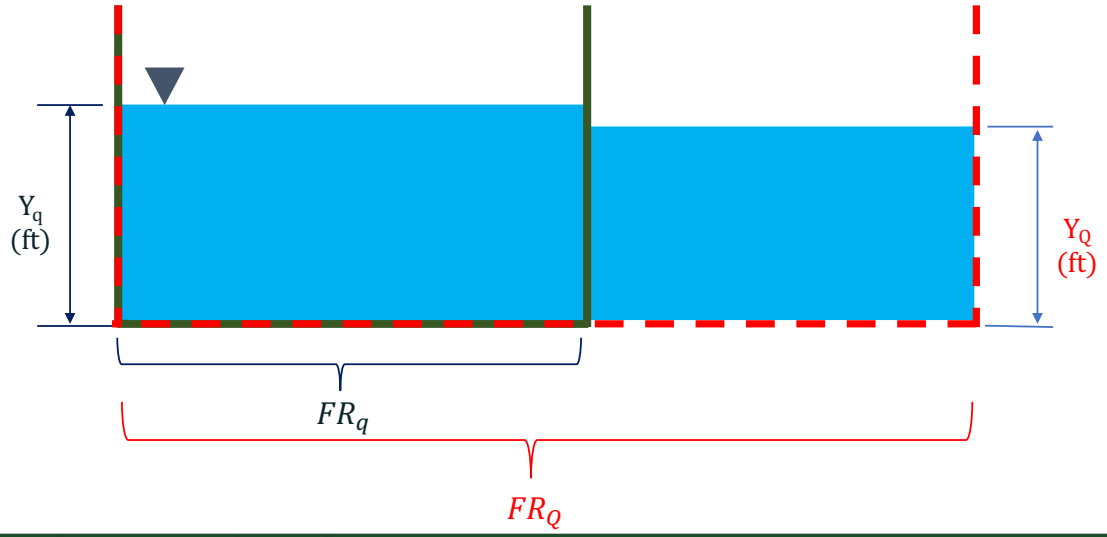

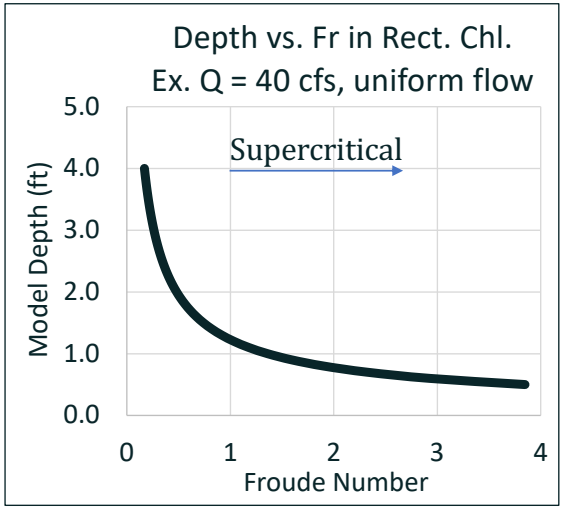

Manning's n in Unit Flowrate Models

$n_{c,Q} < n_{c,q}$

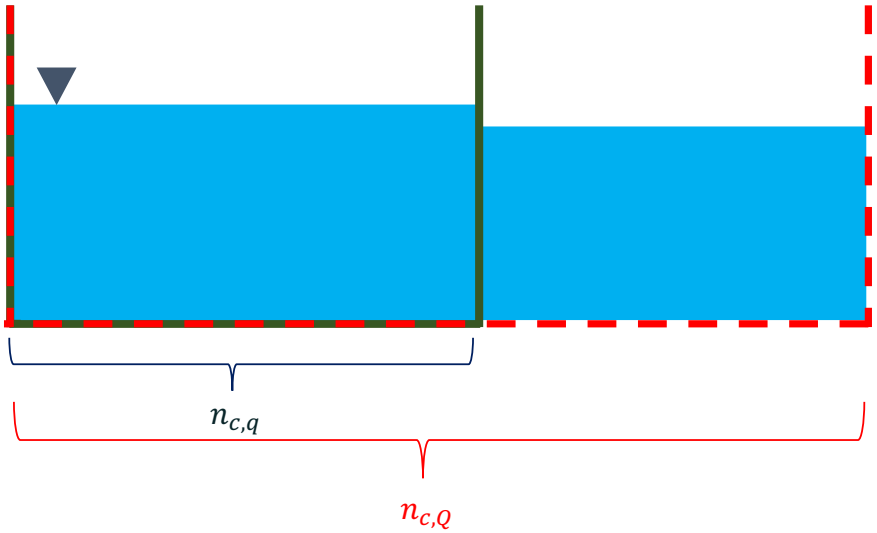

Recall:

- $W_q < W_Q$
- $Y_q > Y_Q$
- $Fr_q < Fr_Q$

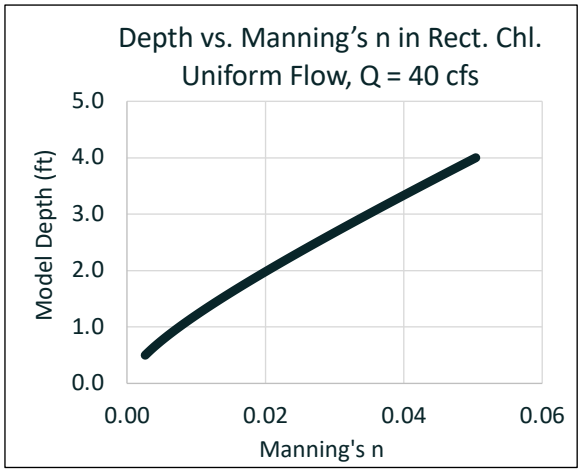


Comparative Analysis
Results from Two Models

$Y_q > Y_Q$

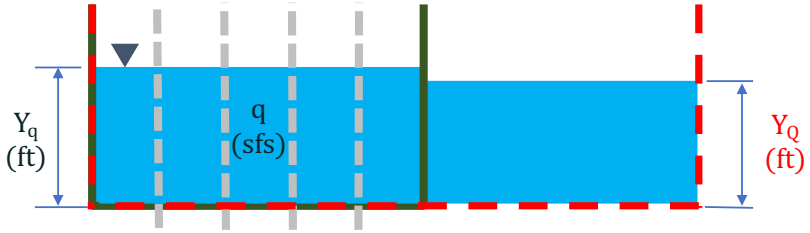

Smooth Walls ->

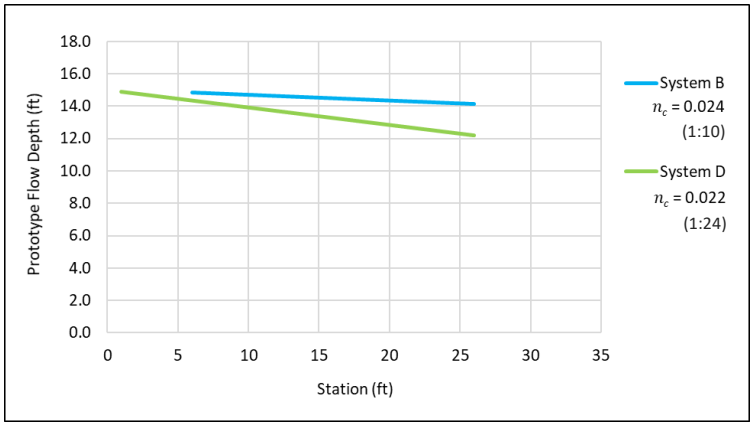

<- Mixed Walls

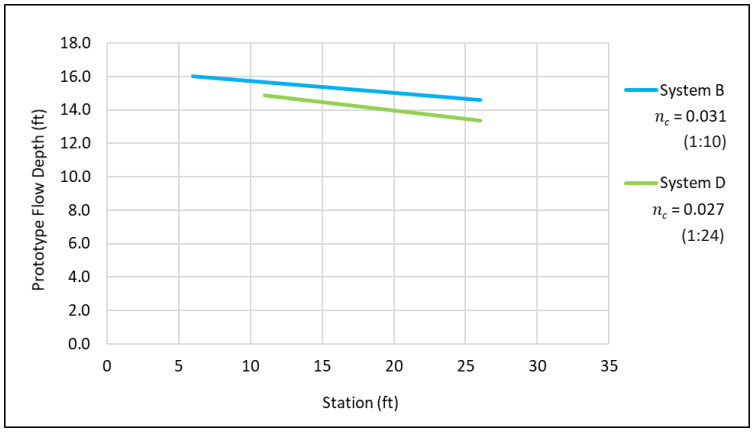

Tangent Walls ->

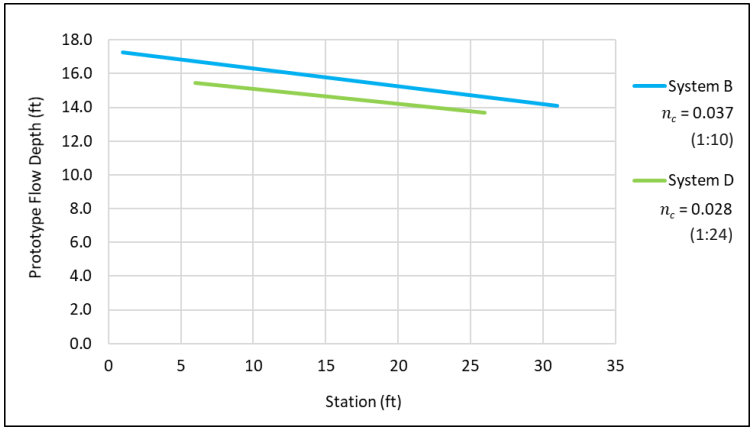

$FR_q < FR_Q$

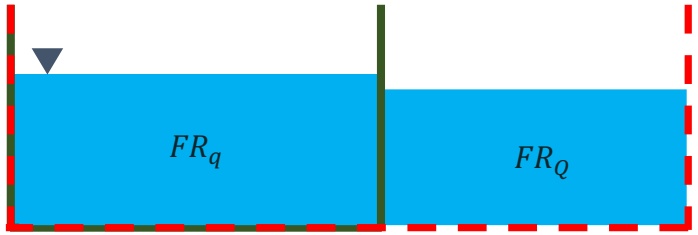

$$Fr = \frac{V}{\sqrt{gY}} = \frac{Q}{Y^{1.5}W\sqrt{g}}$$

$$\mathrm{Fr}_p = \mathrm{Fr}_m$$

Smooth Walls ->

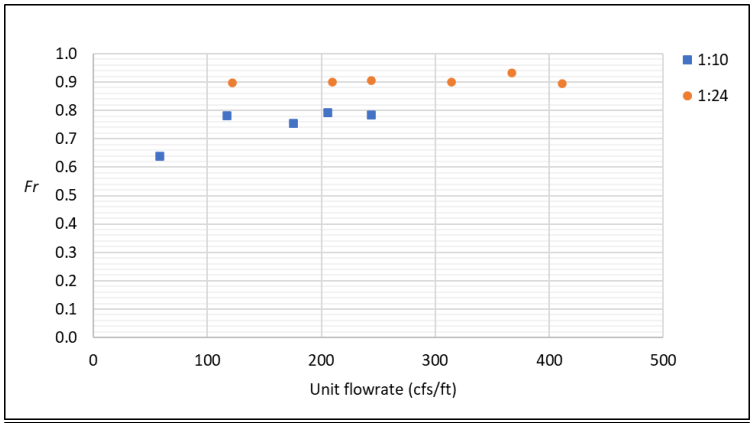

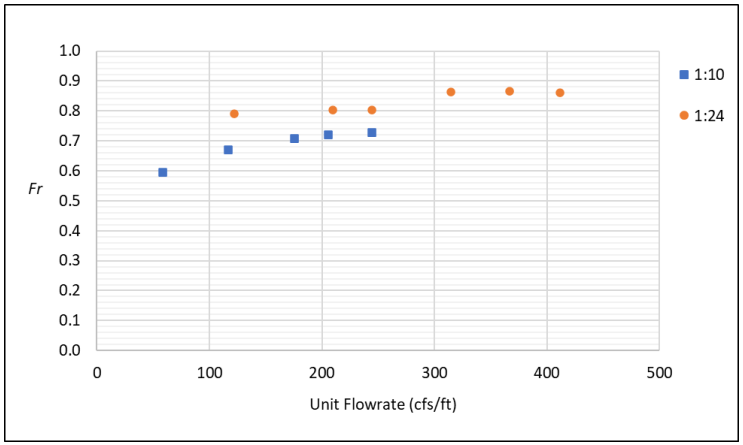

<- Mixed Walls

Tangent Walls ->

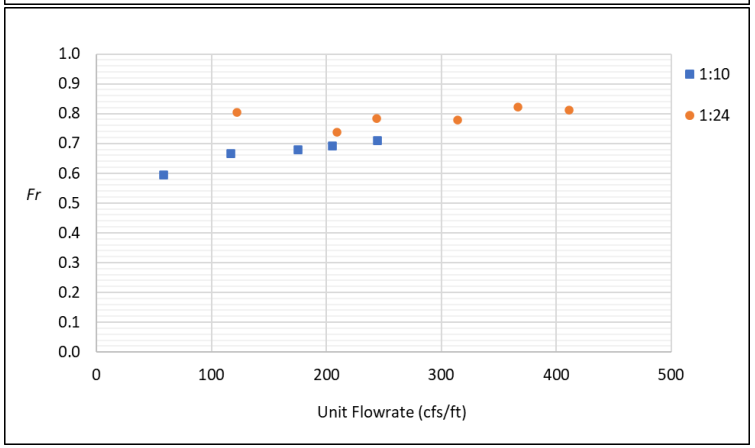

$n_{c,q} > n_{c,Q}$

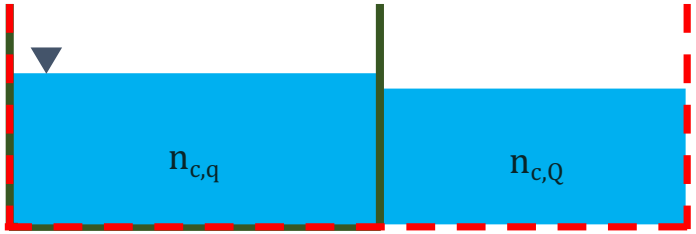

Smooth Walls ->

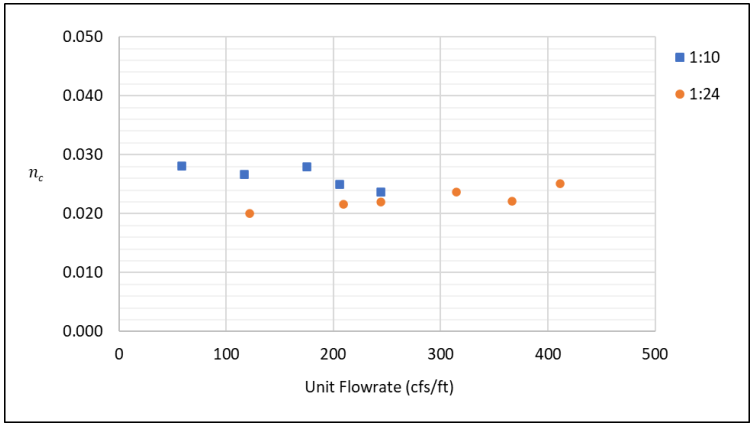

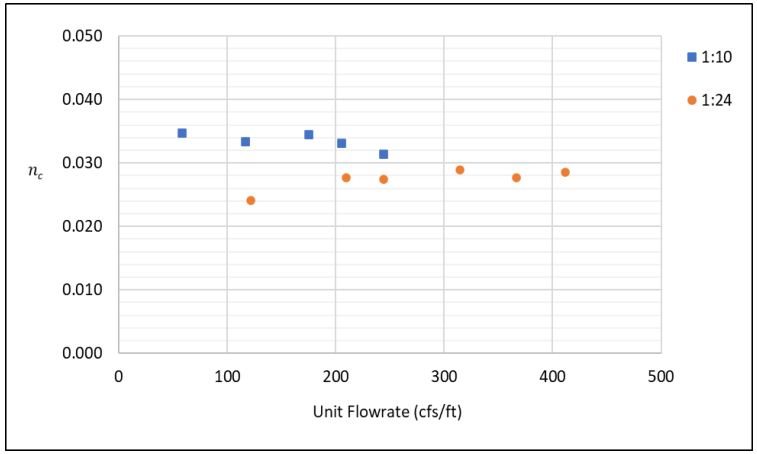

<- Mixed Walls

Tangent Walls ->

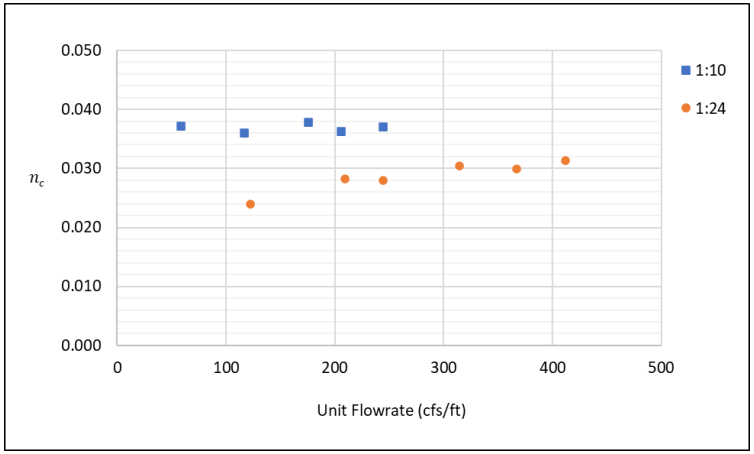

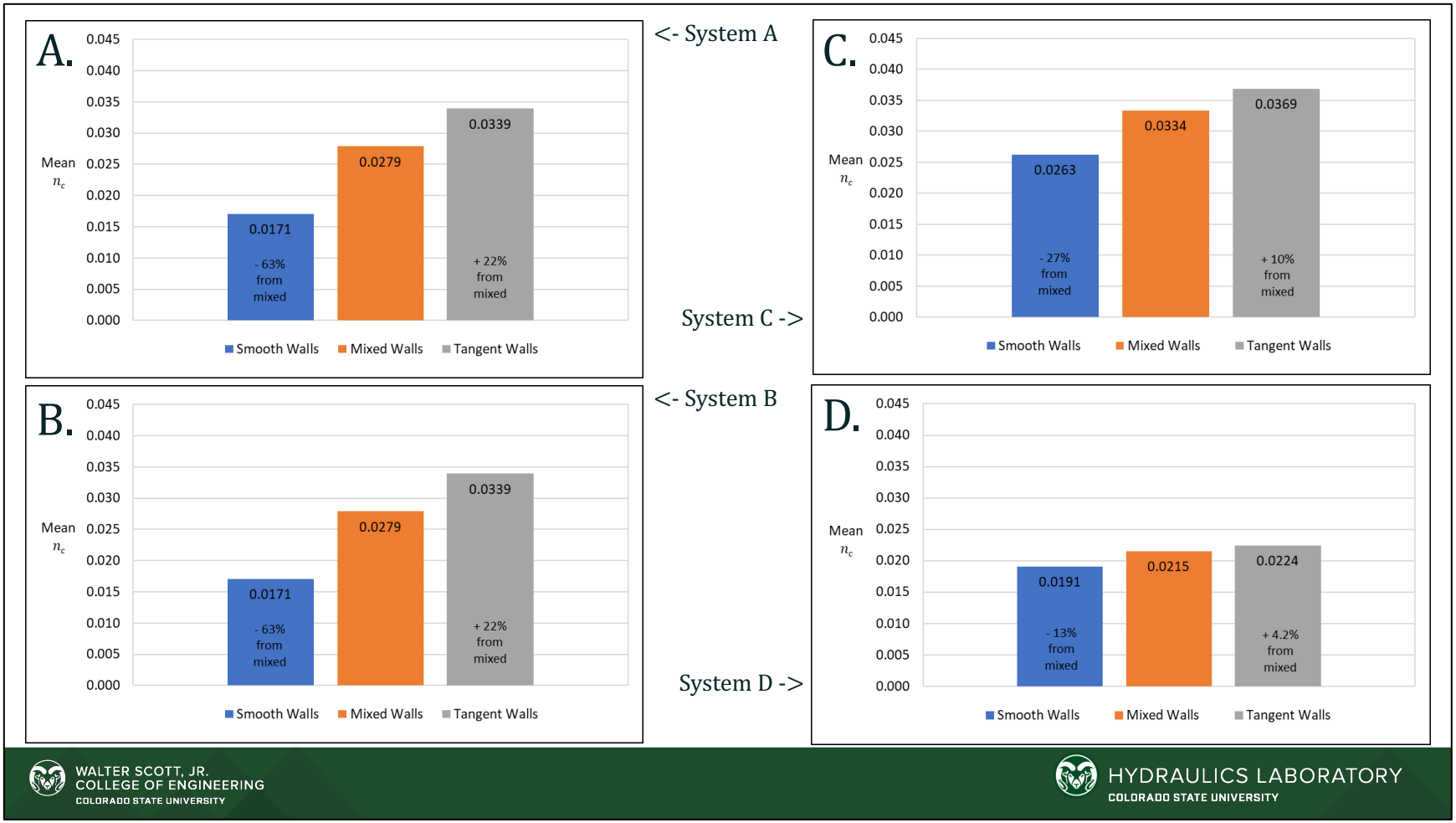
A.
0.045
0.040
0.035
0.030
0.025
0.020
0.015
0.010
0.005
0.000
Mean n_c
0.0171
- 63% from mixed
0.0279
0.0339
+ 22% from mixed
Smooth Walls
Mixed Walls
Tangent Walls
<- System A
System C ->
C.
0.0263
- 27% from mixed
0.0334
0.0369
+ 10% from mixed
<- System B
System D ->
B.
D.
0.0191
- 13% from mixed
0.0215
0.0224
+ 4.2% from mixed

Roughness Elements

$$n_c = \left(\frac{\sum_{i=1}^{n}\left(P_i\, n_i^{1.5}\right)}{P_{total}}\right)^{2/3}$$

$$= \left(\frac{2hn_w^{1.5} + wn_b^{1.5}}{2h+w}\right)^{2/3}$$

Relative Chl. Width

$$\lambda = \frac{w_q}{w_Q}$$

$$\lambda_{RPN} = \frac{50}{120} = 0.42$$

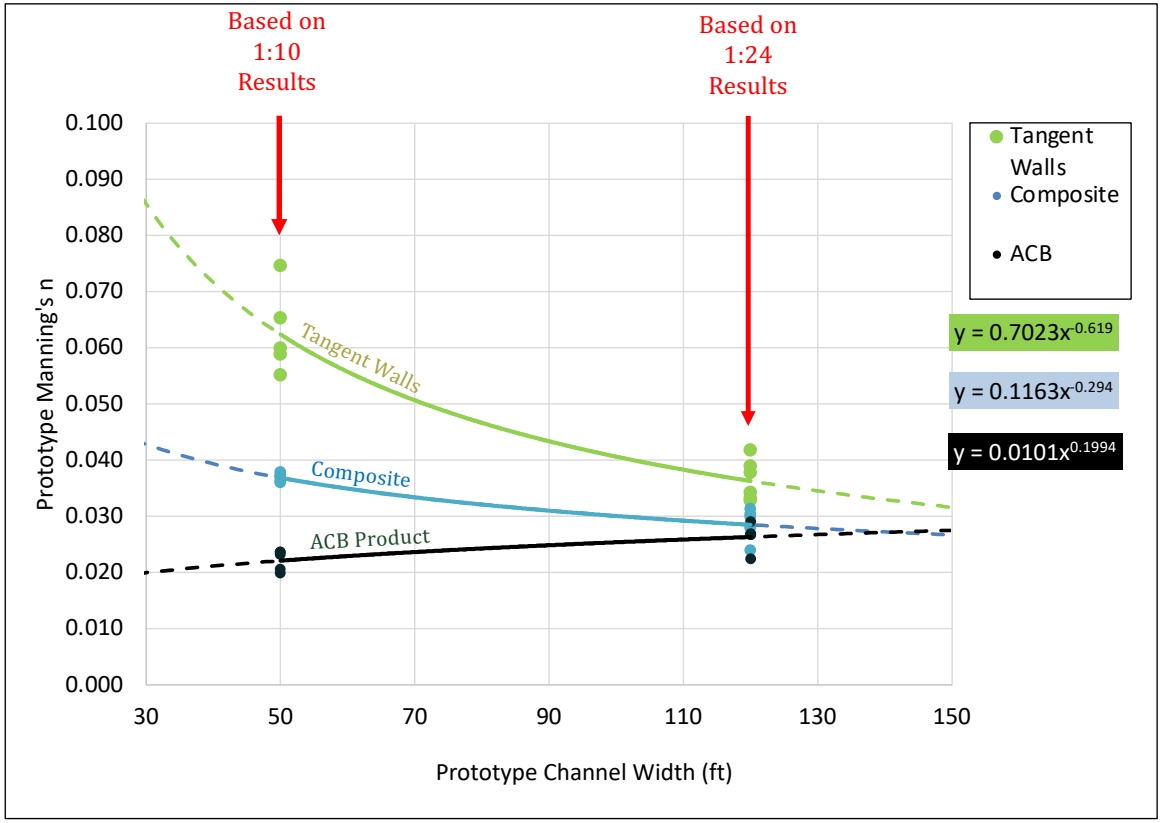

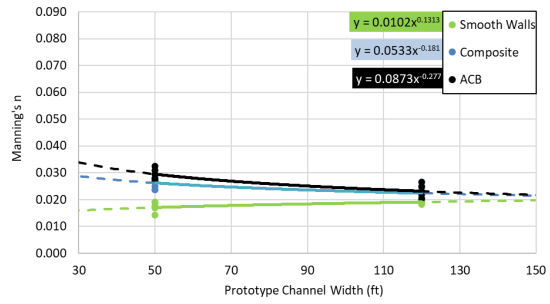

Smooth Walls

$\Gamma = 0.58$

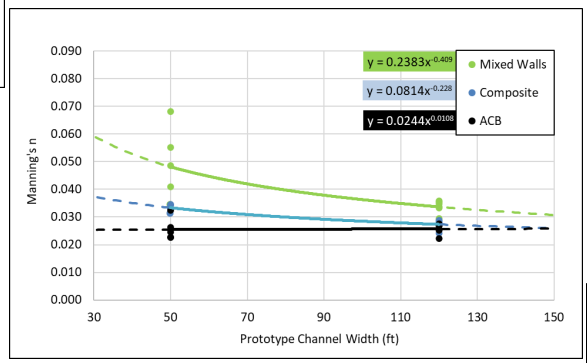

Mixed Walls

$\Gamma = 2.01$

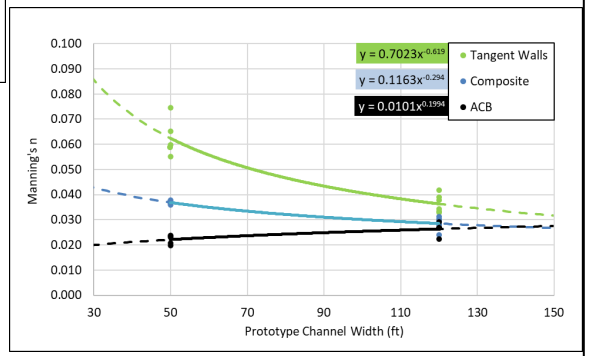

Tangent Walls

$\Gamma = 2.84$

Relative Roughness, Γ

$$\Gamma = \frac{n_w}{n_b}$$


Flow Resistance
Correction Factors
for Unit Flowrate Physical Models

Correction Factor ψ

$$n_{c,Q} = \psi_c n_{c,q}$$

$$n_{w,Q} = \psi_w n_{w,q}$$

$$n_{b,Q} = \psi_b n_{b,q}$$

Channel Walls ->

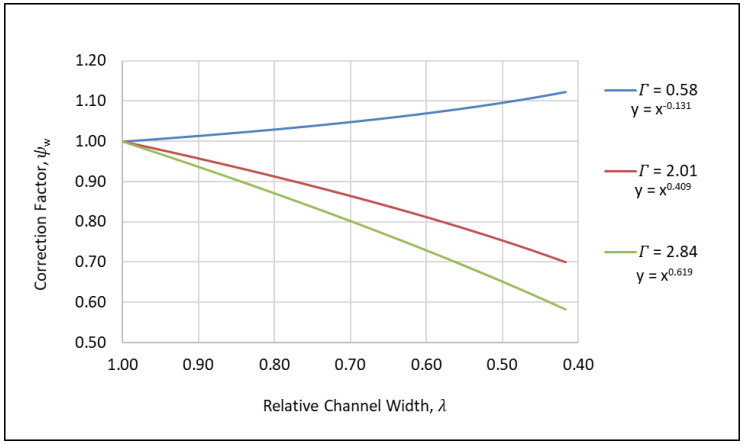

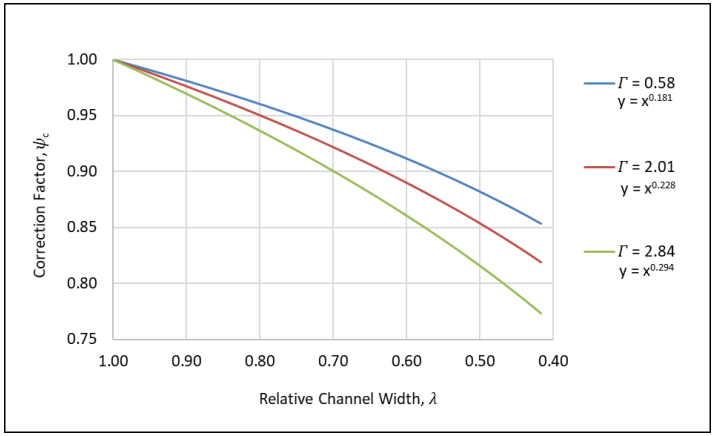

<- Composite

Channel Bed ->

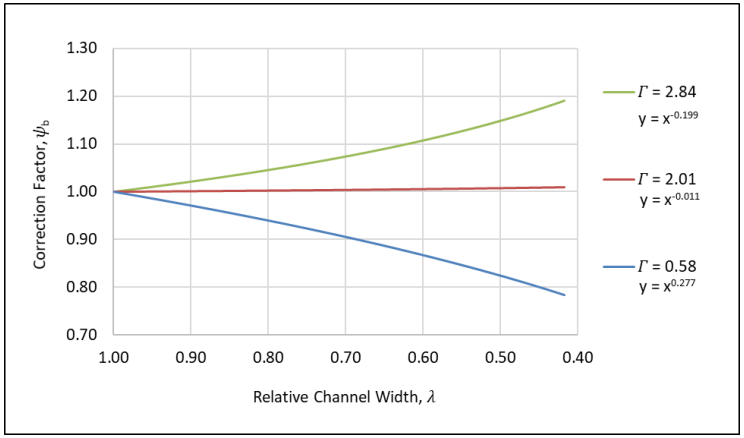

Composite Manning's n Correction Factor ψ_c

$$n_{c,Q} = \psi_c n_{c,q}$$

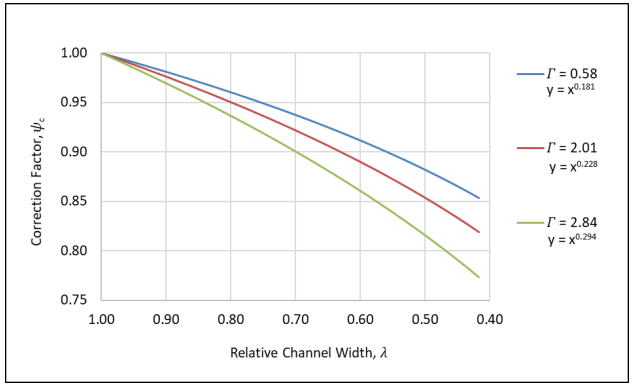

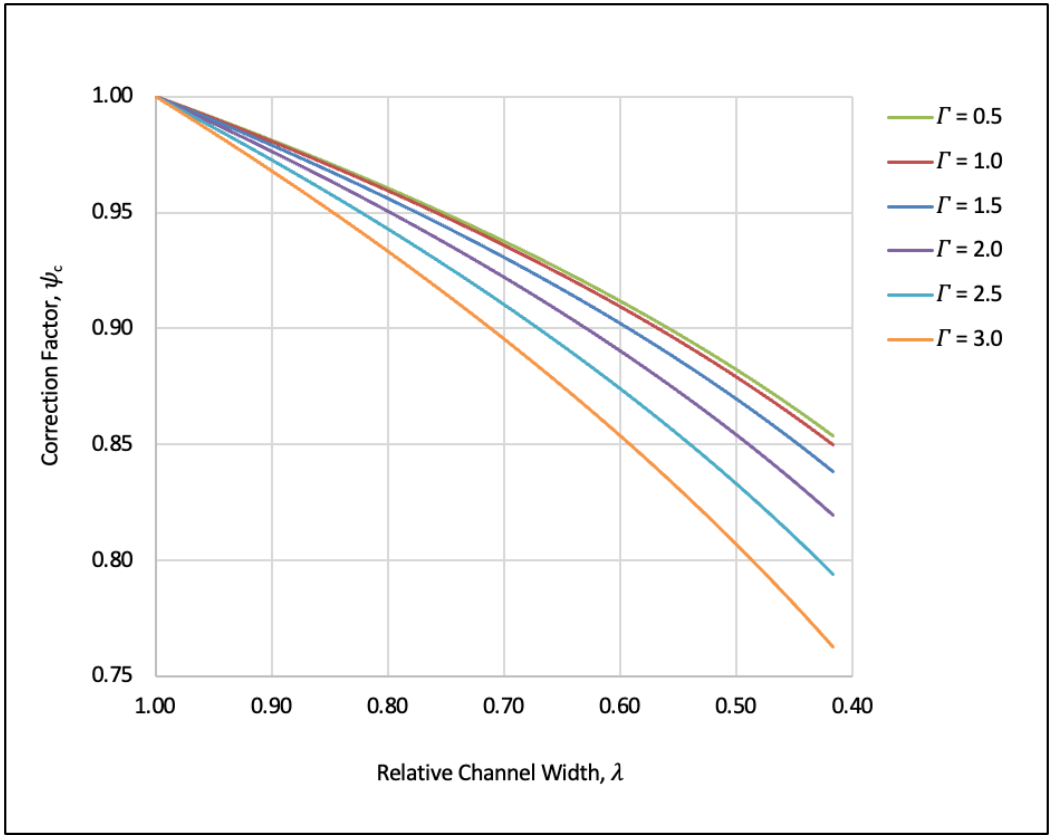

Channel Walls Manning's n Correction Factor ψ_w

$$n_{w,Q} = \psi_w n_{w,q}$$

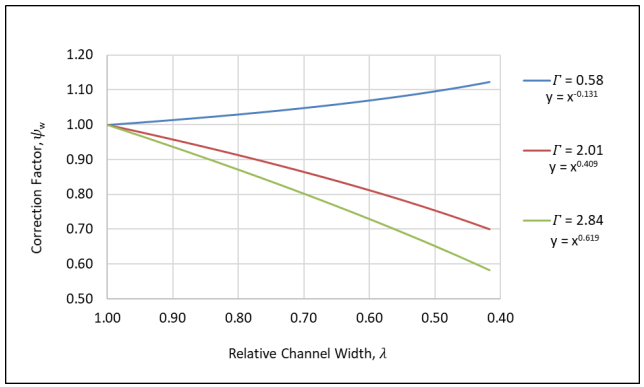

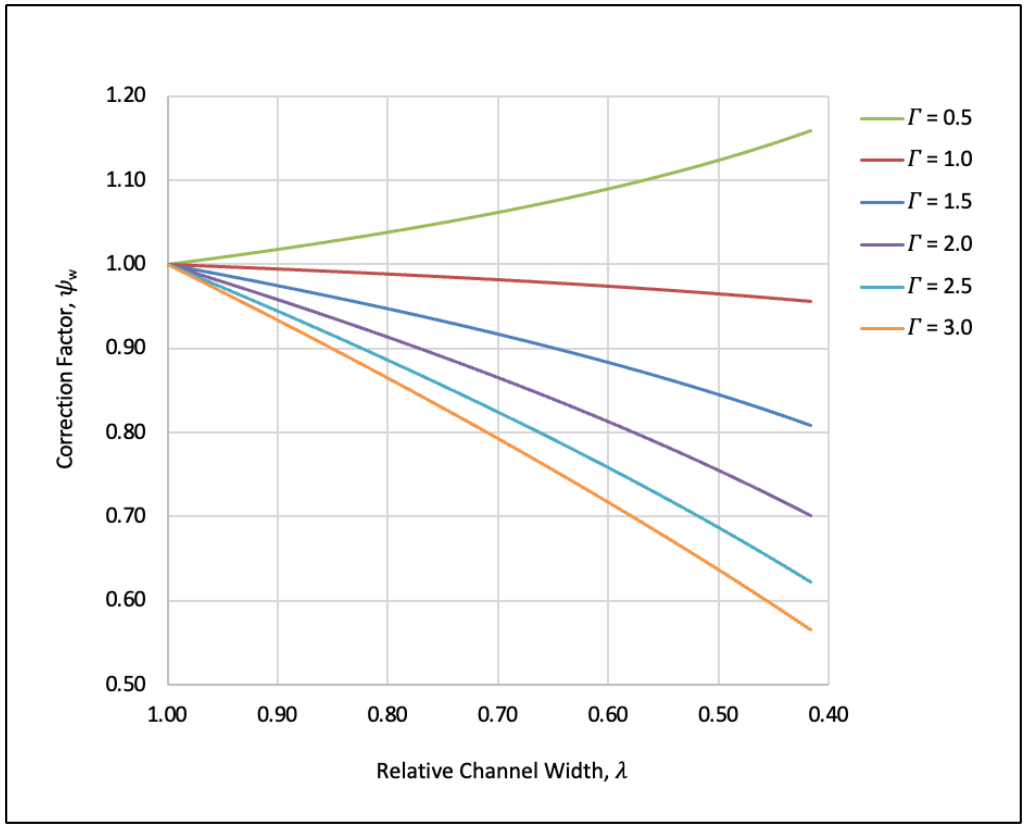

Channel Bed Manning's n Correction Factor ψ_b

$$n_{b,Q} = \psi_b n_{b,q}$$

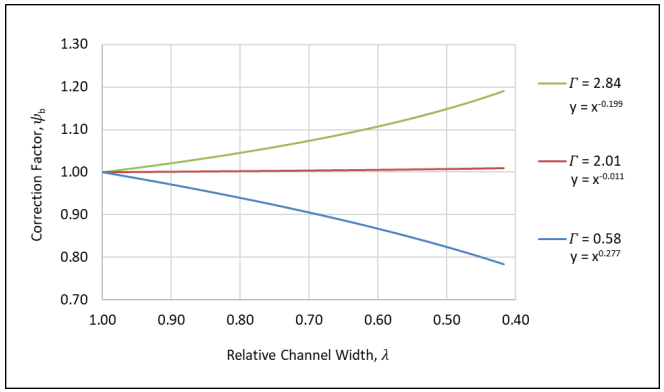

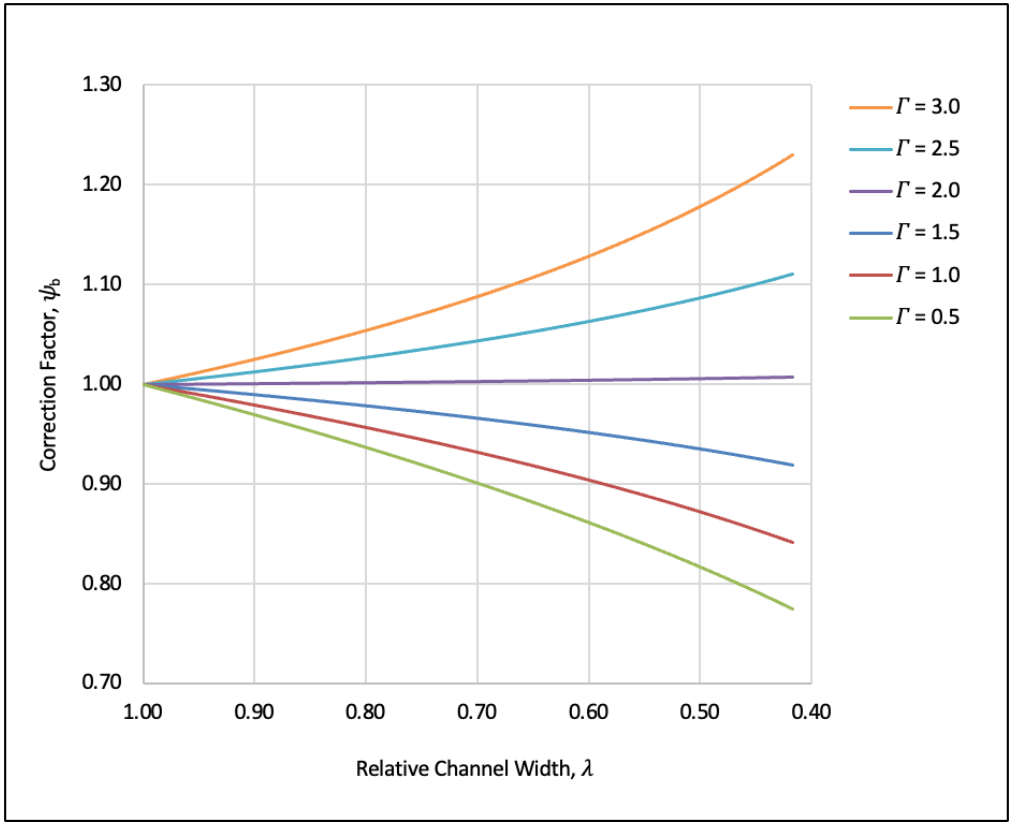

APPENDIX B

Equation Sheet

$$L_r = \frac{L_p}{L_m} \tag{1}$$

$$\mathrm{Fr}_m = \mathrm{Fr}_p \tag{2}$$

$$\mathrm{Fr} = \frac{V}{\sqrt{gY}} \tag{3}$$

$$V_r = L_r^{1/2} \tag{4}$$

$$q_r = V_r L_r = L_r^{\frac{3}{2}} \tag{5}$$

$$Q_r = q_r L_r = L_r^{\frac{5}{2}} \tag{6}$$

$$Q = VA = V(Yw) \tag{7}$$

$$Q = \left(\frac{\phi}{n_c}\right) A\, R^{2/3} S_f^{1/2} = \left(\frac{\phi}{n_c}\right)(Yw)\left(\frac{Yw}{2Y+w}\right)^{2/3} S_f^{1/2} \tag{8}$$

$$n_r = L_r^{1/6} \tag{9}$$

$$Y = \frac{Y_1 + Y_2}{2} \tag{10}$$

$$\mathrm{Fr} = \frac{V}{\sqrt{g\bar{Y}}} = \frac{Q/(Yw)}{\sqrt{g\bar{Y}}} = \frac{Q}{Y^{1.5} w\sqrt{g}} \tag{11}$$

$$n_c = \frac{\phi}{V} R_h^{2/3} S_f^{1/2} = \frac{\phi}{Q/(Yw)}\left(\frac{Yw}{2Y+w}\right)^{2/3} S_f^{1/2} \tag{12}$$

$$S_f = \frac{V^2 n_c^2}{\phi^2 R_h^{4/3}} \tag{13}$$

$$\bar{S_f} = \frac{S_{f_1} + S_{f_2}}{2} \tag{14}$$

$$H_i = z_i + Y_i + \frac{\alpha_i {V_i}^2}{2g} \tag{15}$$

$$H_1^* = H_2 + \bar{S_f}\Delta x \tag{16}$$

$$n_c = \left(\frac{\sum_{i=1}^{n}(P_i\, n_i^{1.5})}{P_{total}}\right)^{2/3} = \left(\frac{2hn_w^{1.5} + wn_b^{1.5}}{2h+w}\right)^{2/3} \tag{17}$$

$$\Gamma = \frac{n_w}{n_b} \tag{18}$$

$$\lambda = \frac{w_q}{w_Q} \tag{19}$$

$$n_{c,Q} = \psi_c n_{c,q} \tag{20}$$

$$n_{w,Q} = \psi_w n_{w,q} \tag{21}$$

$$n_{b,Q} = \psi_b n_{b,q} \tag{22}$$

$$\delta = \left|\frac{n_{obs} - n_{exp}}{n_{exp}}\right| * 100\% \tag{23}$$

$$\psi = \lambda^{\beta} \tag{24}$$

APPENDIX C

Photographs

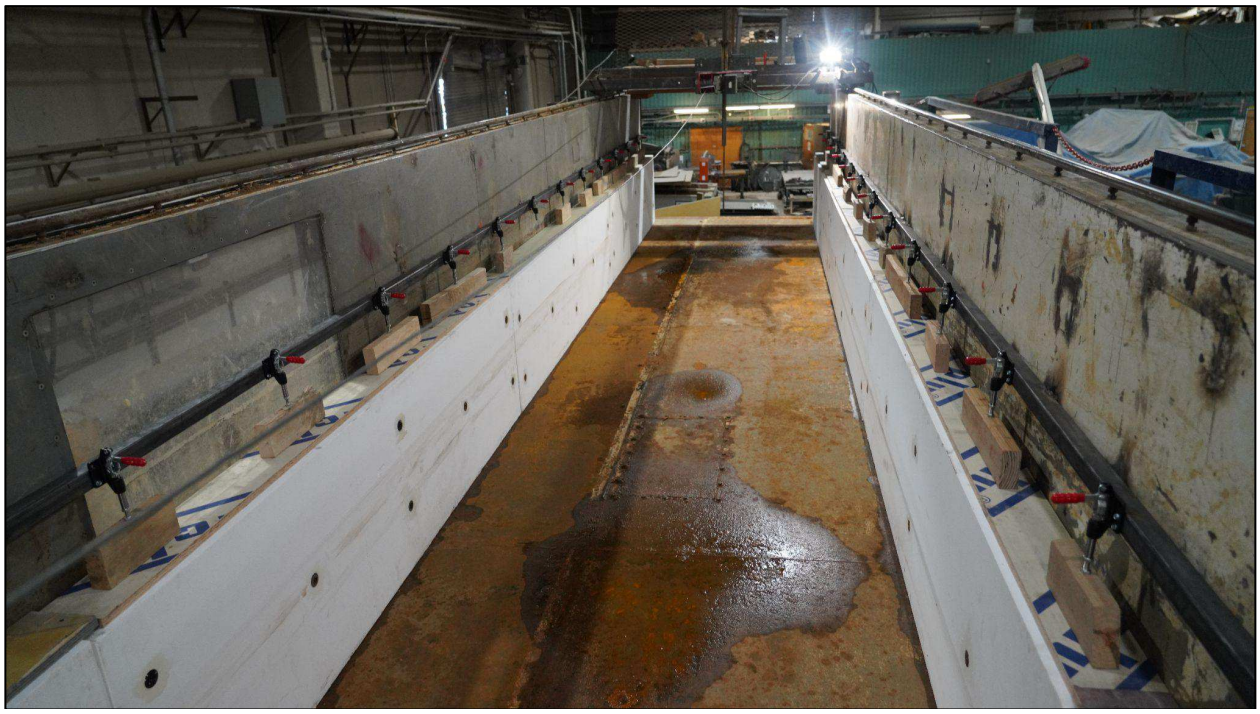

Fig. C1. System A smooth wall configuration

Fig. C2. System A mixed wall configuration

Fig. C3. System A tangent wall configuration

Fig. C4. System B smooth wall configuration

Fig. C5. System B mixed wall configuration

Fig. C6. System B tangent wall configuration

Fig. C7. System C smooth wall configuration

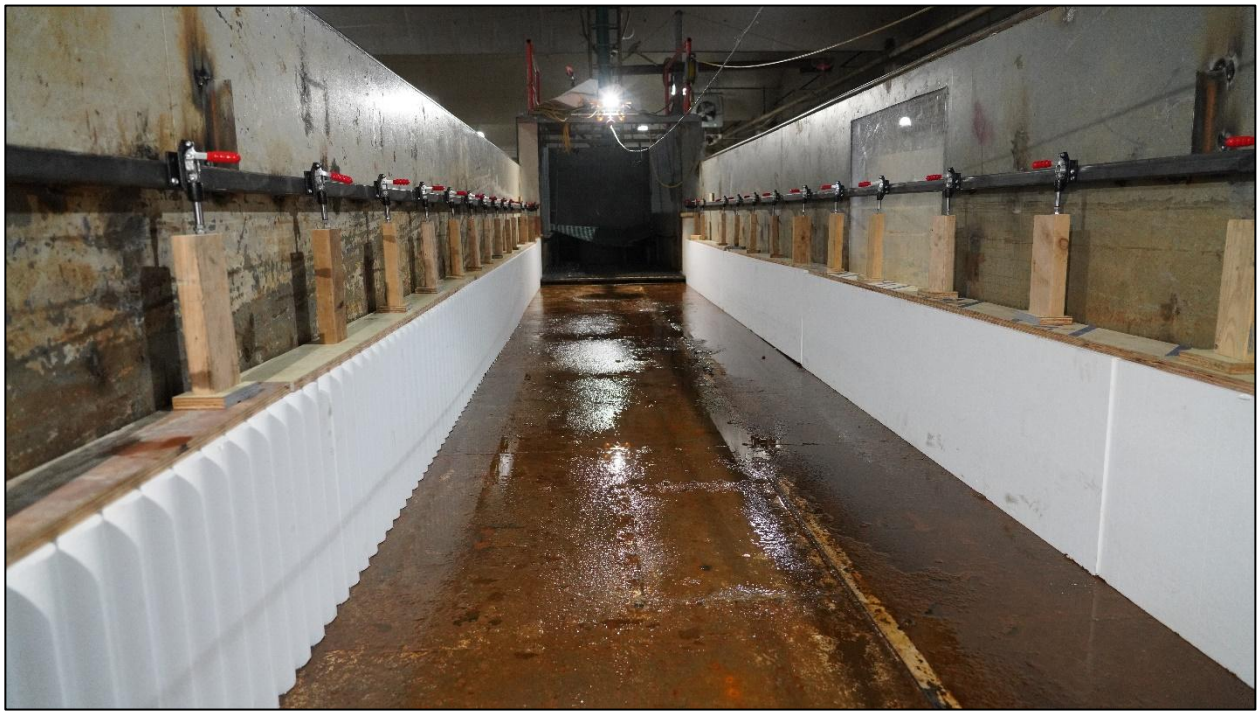

Fig. C8. System C mixed wall configuration

Fig. C9. System C tangent wall configuration

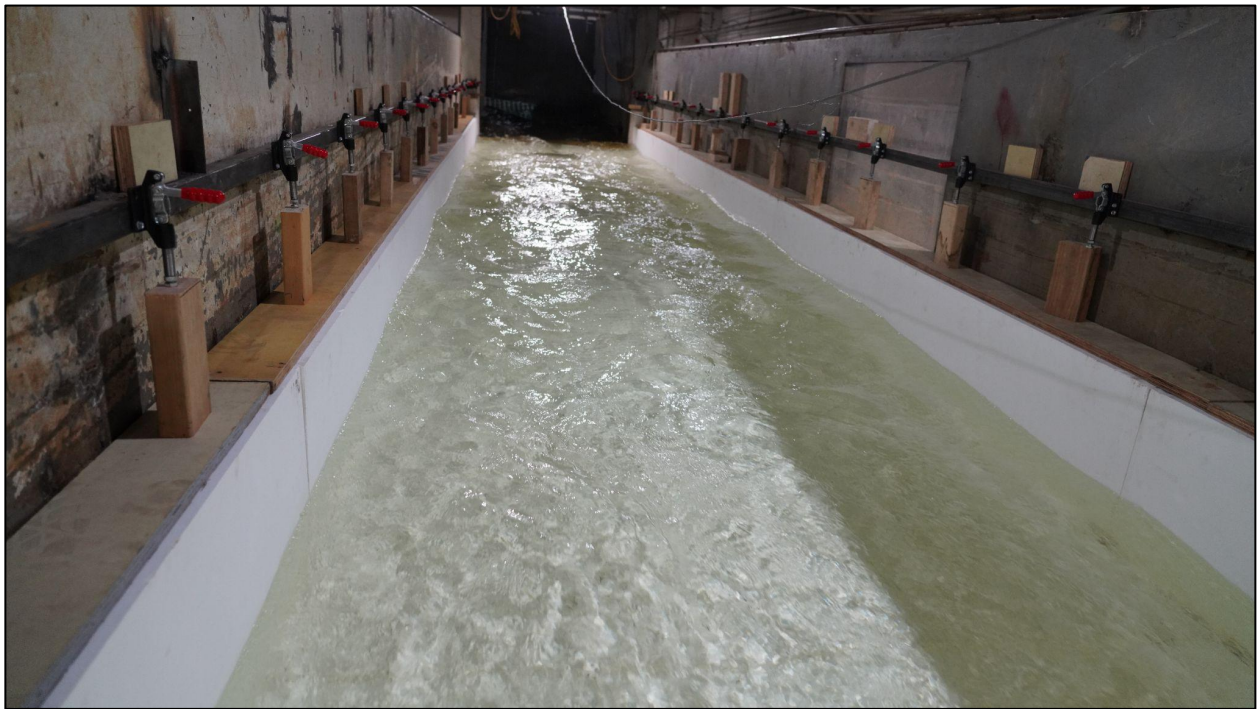

Fig. C10. System D smooth wall configuration

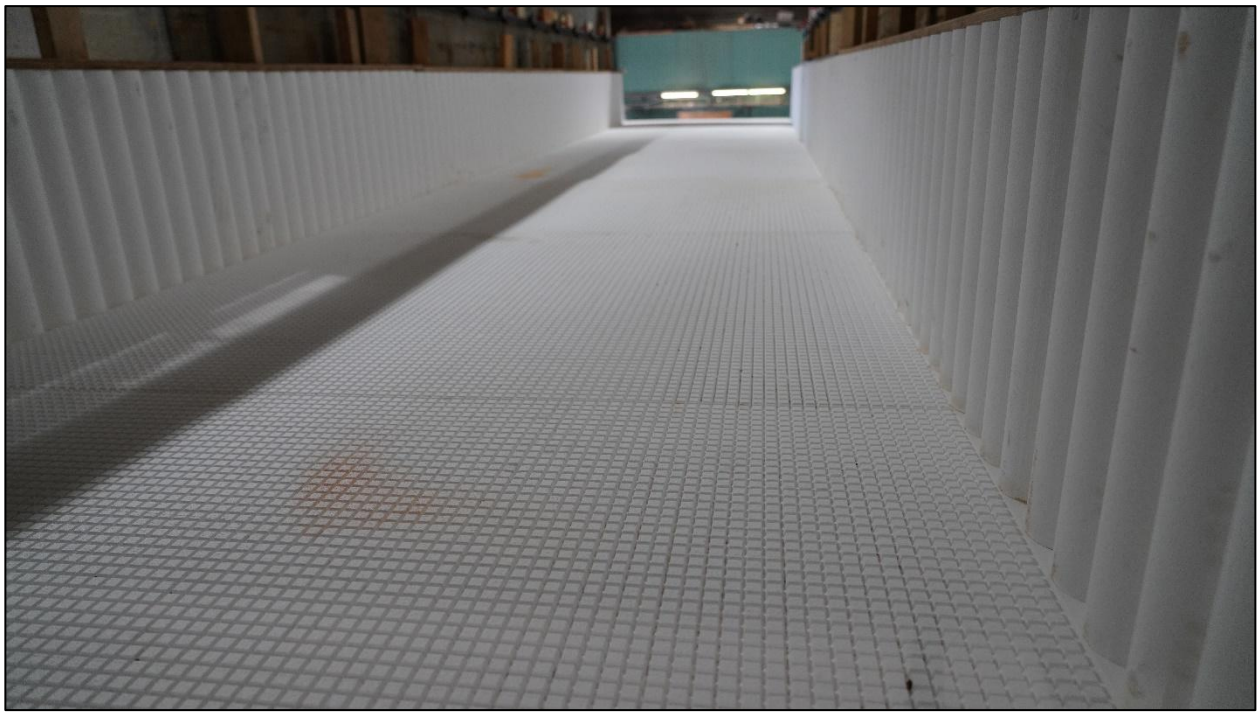

Fig. C11. System D tangent wall configuration

System D mixed wall configuration was not documented by photograph.

APPENDIX D

Velocity Estimates

The following tables and figures summarize velocities estimated at the model scale and prototype scale. Table B1 presents the velocities used in the analysis of the model, established using the continuity relationship provided by Eq. (7), and the reach averaged flow depths summarized in Table 7. Table B2 presents the ADV Velocimeter measurements that were taken for several of the model configurations.

Table D1: Velocity from continuity relationships

System & Description	Q_m (cfs)	Smooth Wall (V, fps)		Mixed Walls (V, fps)		Tangent Walls (V, fps)	
		Model	Prototype	Model	Prototype	Model	Prototype
System A *1:10, Smooth Bed*	38.6	7.04	22.3	5.28	16.7	5.10	16.1
	32.5	6.67	21.1	5.04	15.9	4.59	14.5
	27.8	6.41	20.3	4.81	15.2	4.46	14.1
	18.5	5.20	16.4	4.10	13.0	3.84	12.1
	9.3	3.85	12.2	3.18	10.1	3.02	9.5
System B *1:10, ACB*	38.6	5.34	16.9	5.08	16.1	5.00	15.8
	32.5	5.09	16.1	4.77	15.1	4.65	14.7
	27.8	4.68	14.8	4.48	14.2	4.35	13.8
	18.5	4.17	13.2	3.77	11.9	3.75	11.9
	9.3	2.91	9.2	2.78	8.8	2.77	8.8
System C *1:24, Smooth Bed*	17.5	6.46	31.6	5.97	29.2	5.30	26.0
	15.6	6.26	30.7	5.88	28.8	5.18	25.4
	13.4	6.03	29.5	5.58	27.4	5.04	24.7
	10.4	5.43	26.6	4.94	24.2	4.46	21.9
	8.9	5.28	25.8	4.94	24.2	4.20	20.6
	5.2	4.40	21.5	4.15	20.3	3.70	18.1
System D *1:24, ACB*	17.5	4.49	22.0	4.37	21.4	4.21	20.6
	15.6	4.44	21.7	4.22	20.7	4.08	20.0
	13.4	4.12	20.2	4.01	19.7	3.74	18.3
	10.4	3.80	18.6	3.51	17.2	3.46	16.9
	8.9	3.59	17.6	3.33	16.3	3.15	15.4
	5.2	3.00	14.7	2.76	13.5	2.79	13.7

ADV velocimeter data were collected during using the systematic grid illustrated in Figure 13. For the runs in which the Velocimeter was utilized, velocity was collected every 10-ft starting at STA 11. Five measurements were taken at each cross-section in which data was captured. Table D2 and the associated figures present data at STA 20, the center point of the flume, for the 100-year return interval design flow.

Table D2: Velocimeter Results

Description	Model Scale (fps)				Prototype Scale (fps)			
	Vx	Vy	Vz	Vmag	Vx	Vy	Vz	Vmag
System A Smooth Walls	6.93	-0.10	-0.24	6.93	21.91	-0.32	-0.76	21.91
	7.39	-0.13	-0.44	7.40	23.37	-0.41	-1.39	23.40
	7.40	-0.04	-0.52	7.41	23.40	-0.13	-1.64	23.43
	6.88	-0.04	0.00	6.88	21.76	-0.13	0.00	21.76
	6.79	-0.19	-0.77	6.83	21.47	-0.60	-2.43	21.60
System A Mixed Walls	5.16	-0.31	-0.22	5.17	16.32	-0.98	-0.70	16.35
	5.47	-0.10	-0.30	5.48	17.30	-0.32	-0.95	17.33
	5.58	0.17	-0.26	5.59	17.65	0.54	-0.82	17.68
	5.15	0.19	0.09	5.16	16.29	0.60	0.28	16.32
	5.18	-0.04	-0.53	5.21	16.38	-0.13	-1.68	16.48
System A Tangent Walls	5.30	-0.26	-0.36	5.32	16.76	-0.82	-1.14	16.82
	5.78	-0.04	-0.44	5.80	18.28	-0.13	-1.39	18.34
	5.79	0.13	-0.32	5.80	18.31	0.41	-1.01	18.34
	5.08	0.29	-0.30	5.10	16.06	0.92	-0.95	16.13
	4.95	0.21	-0.64	5.00	15.65	0.66	-2.02	15.81
System B Smooth Walls	5.36	-0.17	-0.34	5.37	16.95	-0.54	-1.08	16.98
	5.55	-0.20	-0.43	5.57	17.55	-0.63	-1.36	17.61
	5.37	-0.18	-0.55	5.40	16.98	-0.57	-1.74	17.08
	5.01	-0.26	-0.08	5.02	15.84	-0.82	-0.25	15.87
	5.07	-0.39	-0.78	5.14	16.03	-1.23	-2.47	16.25
System B Mixed Walls	4.91	-0.43	-0.41	4.95	15.53	-1.36	-1.30	15.65
	3.36	-0.26	-0.13	3.38	10.63	-0.82	-0.41	10.69
	4.04	0.02	-0.30	4.05	12.78	0.06	-0.95	12.81
	4.73	-0.11	-0.44	4.75	14.96	-0.35	-1.39	15.02
	2.77	-0.20	-0.34	2.80	8.76	-0.63	-1.08	8.85
System B Tangent Walls	4.66	-0.07	-0.52	4.69	14.74	-0.22	-1.64	14.83
	5.85	0.10	-0.74	5.90	18.50	0.32	-2.34	18.66
	5.73	0.27	-0.79	5.80	18.12	0.85	-2.50	18.34
	5.15	0.32	-0.54	5.19	16.29	1.01	-1.71	16.41
	4.69	0.30	-0.77	4.76	14.83	0.95	-2.43	15.05

All data reported in Table B2 reflect the velocity captured at 60% of the depth, from the top of the water column. The velocity captured in this location is an approximate representation of the depth-averaged velocity in a water column. Each of the velocity components is summarized as follows:

- Vx: longitudinal velocity (along channel centerline)
- Vy: transverse velocity (along the cross-section)
- Vz: vertical (along the water column)
- Vmag: magnitude of resulting velocity vector (x, y, & z)

Figures B1 – B6 present the cross-sectional prototype results reported in Table B2 for the ADV Velocimeter data. These figures highlight the variability of velocity within a cross-section. It is anticipated that there is additional variability within the water column. This further supports the use of Table B1 velocities, which provide a method for estimating the cross-sectional depth-averaged velocity based on continuity (Q = VA).

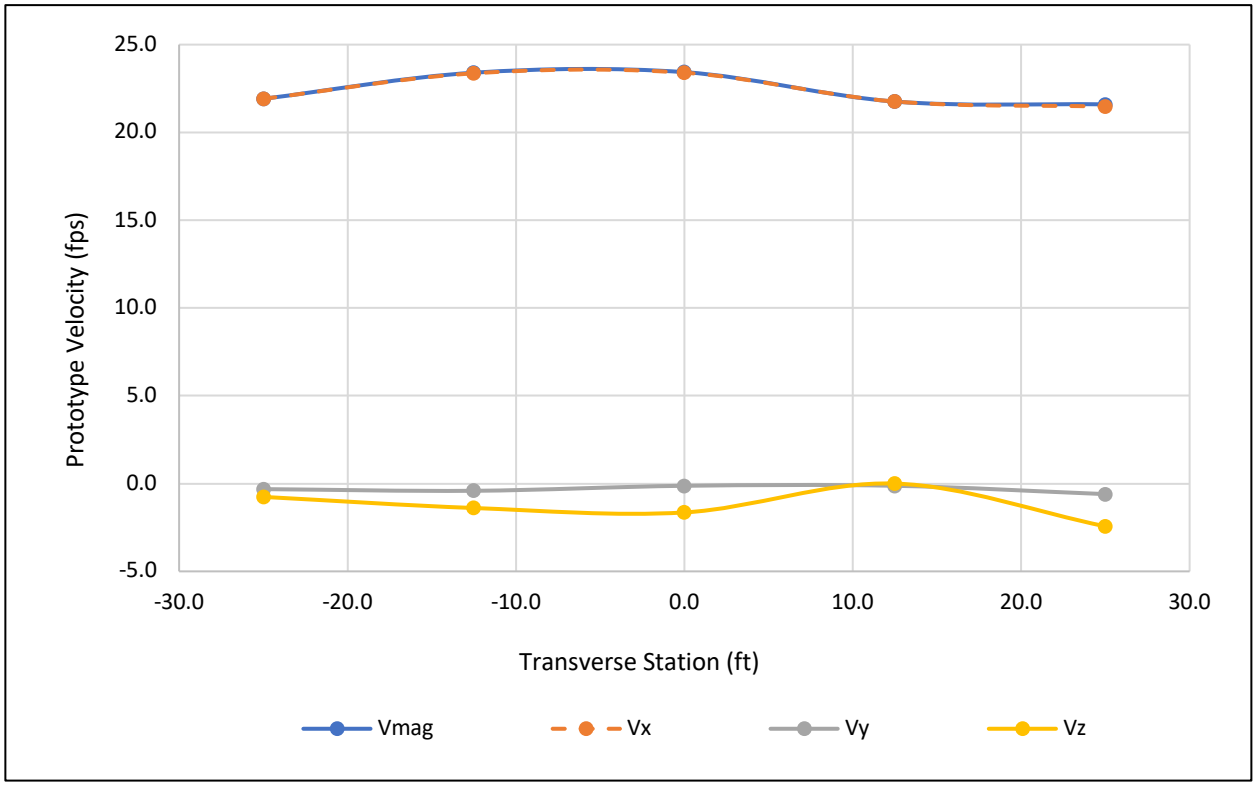

Fig. D1. Velocimeter results for System A, smooth wall configuration

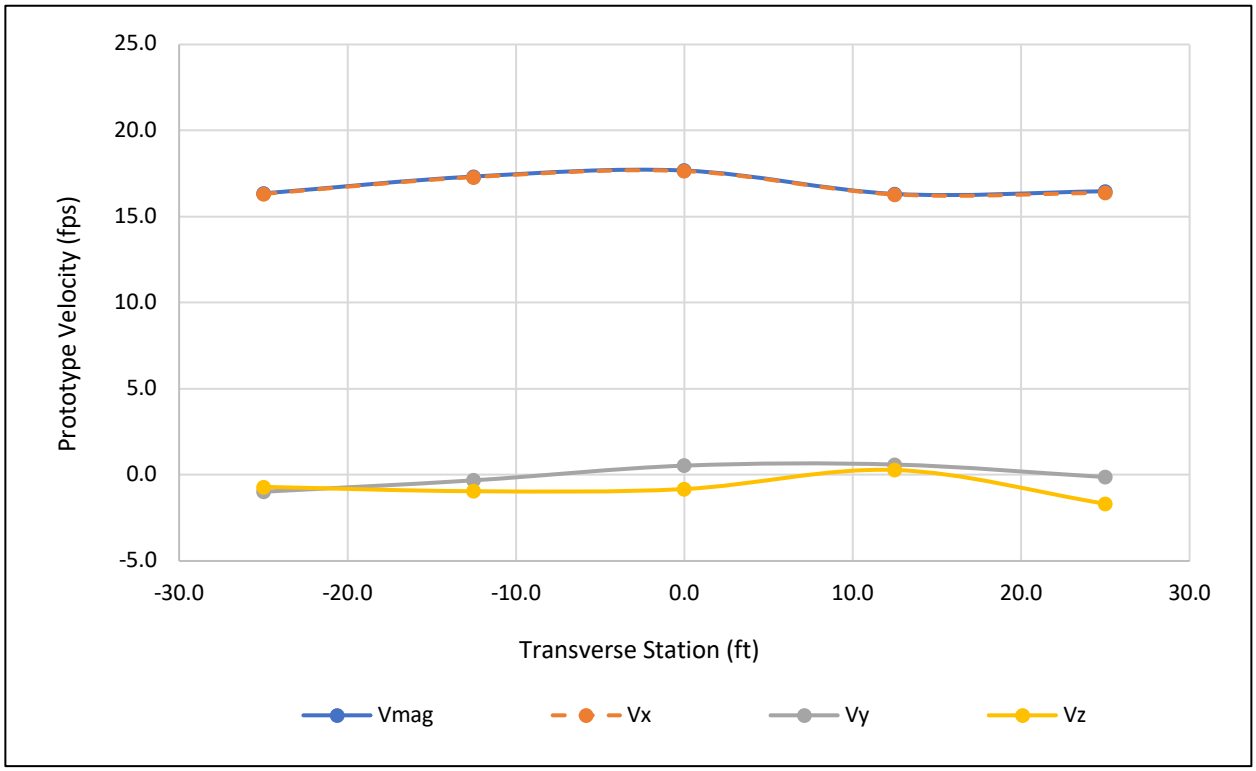

Fig. D2. Velocimeter results for System A, mixed wall configuration

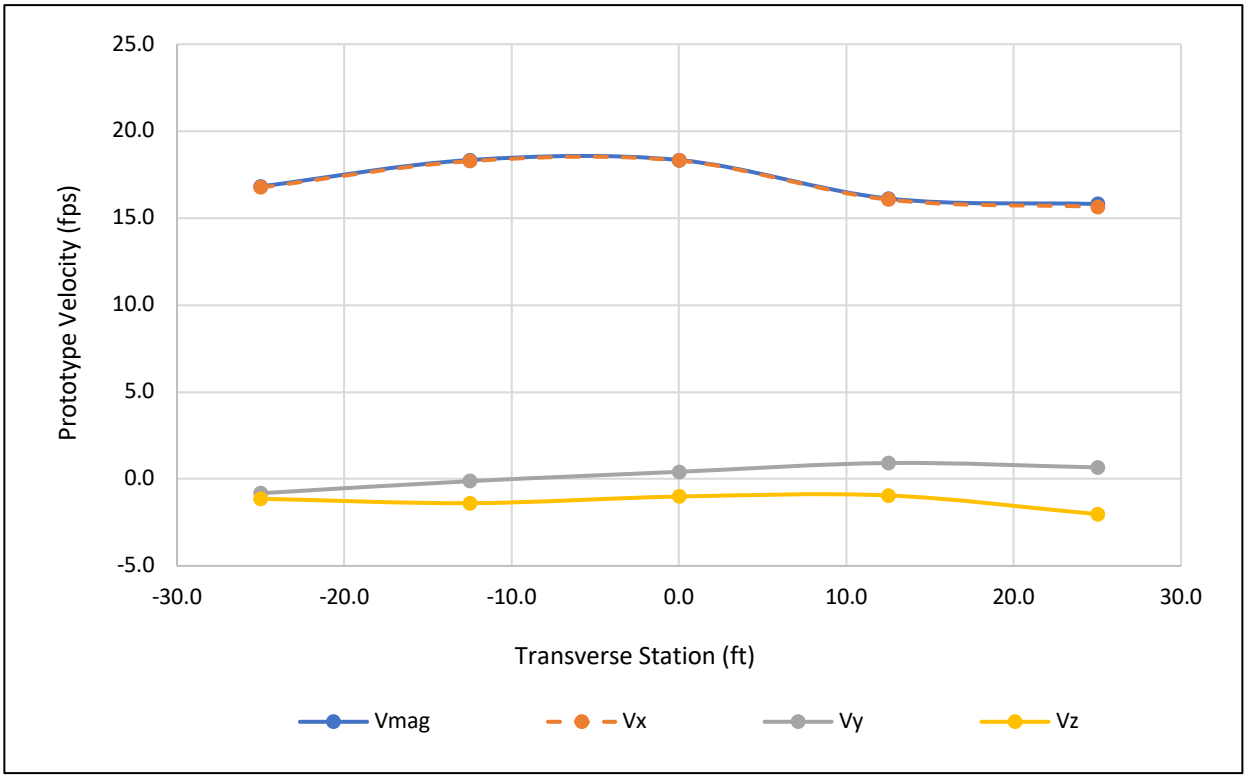

Fig. D3. Velocimeter results for System A, tangent wall configuration

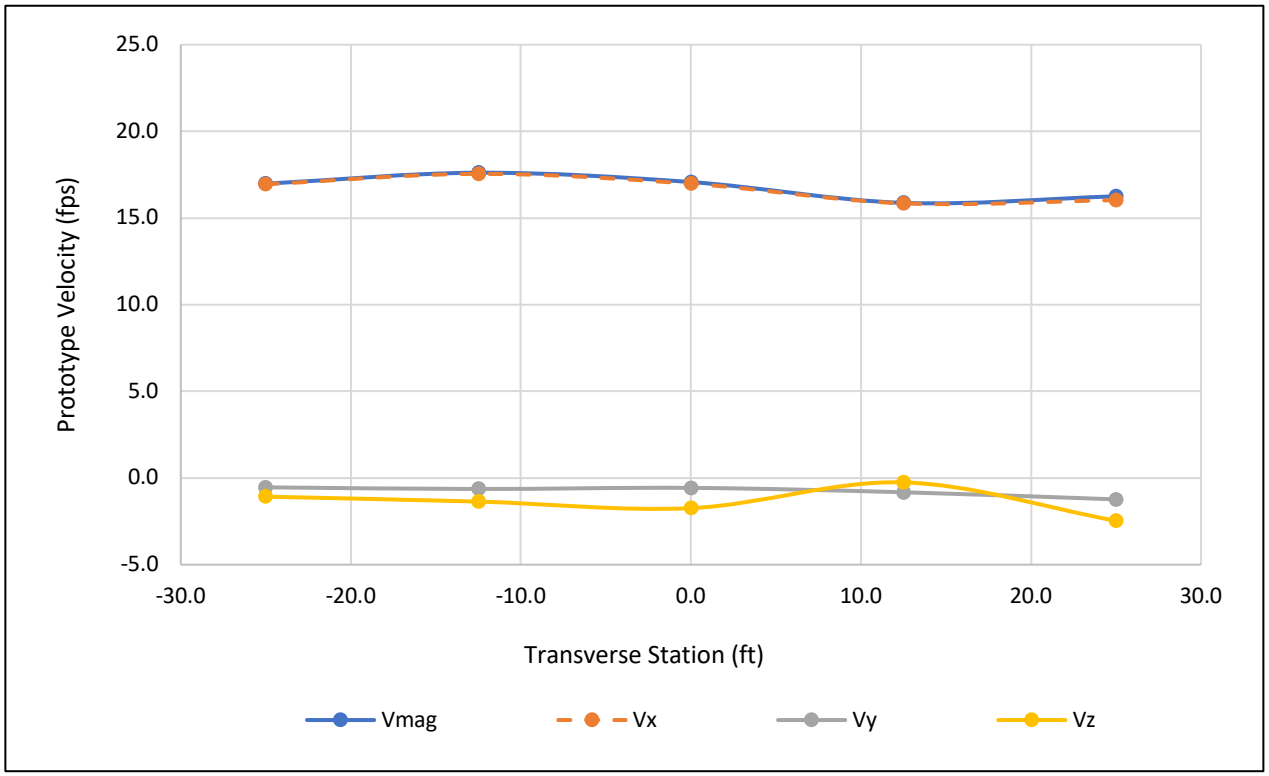

Fig. D4. Velocimeter results for System B, smooth wall configuration

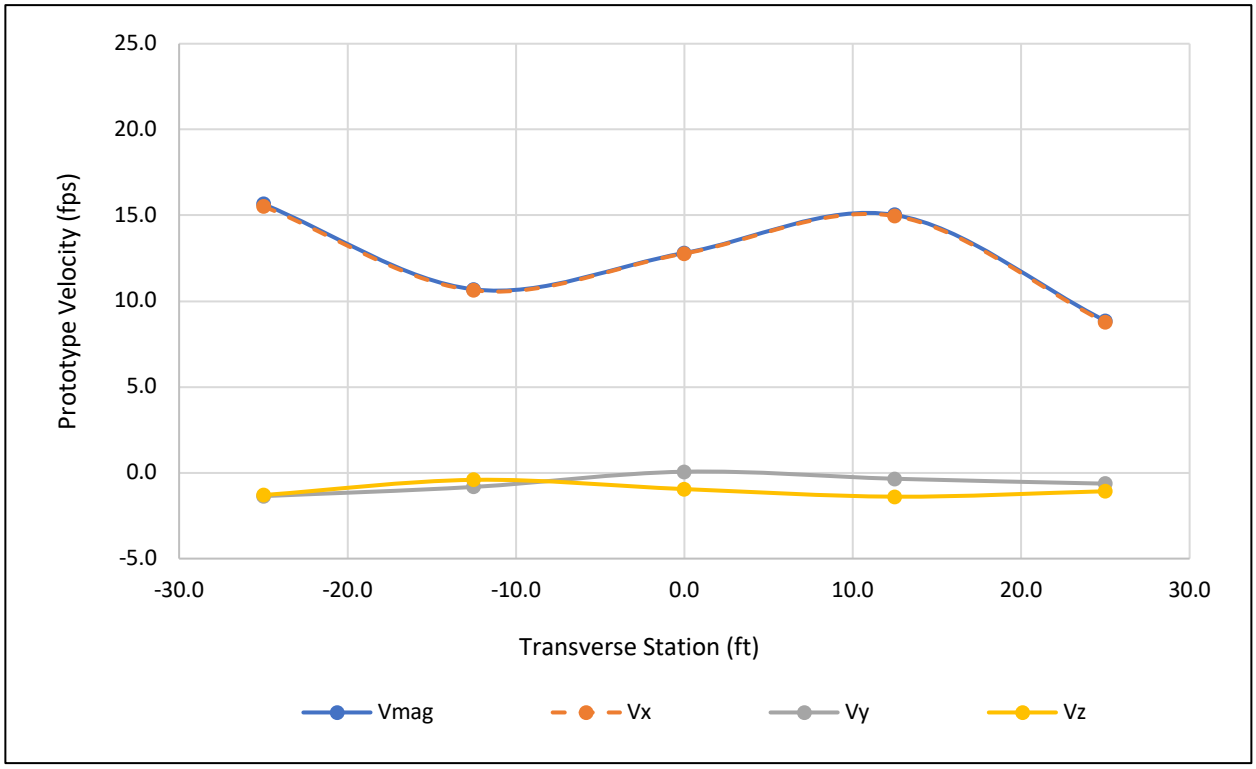

Fig. D5. Velocimeter results for System B, mixed wall configuration

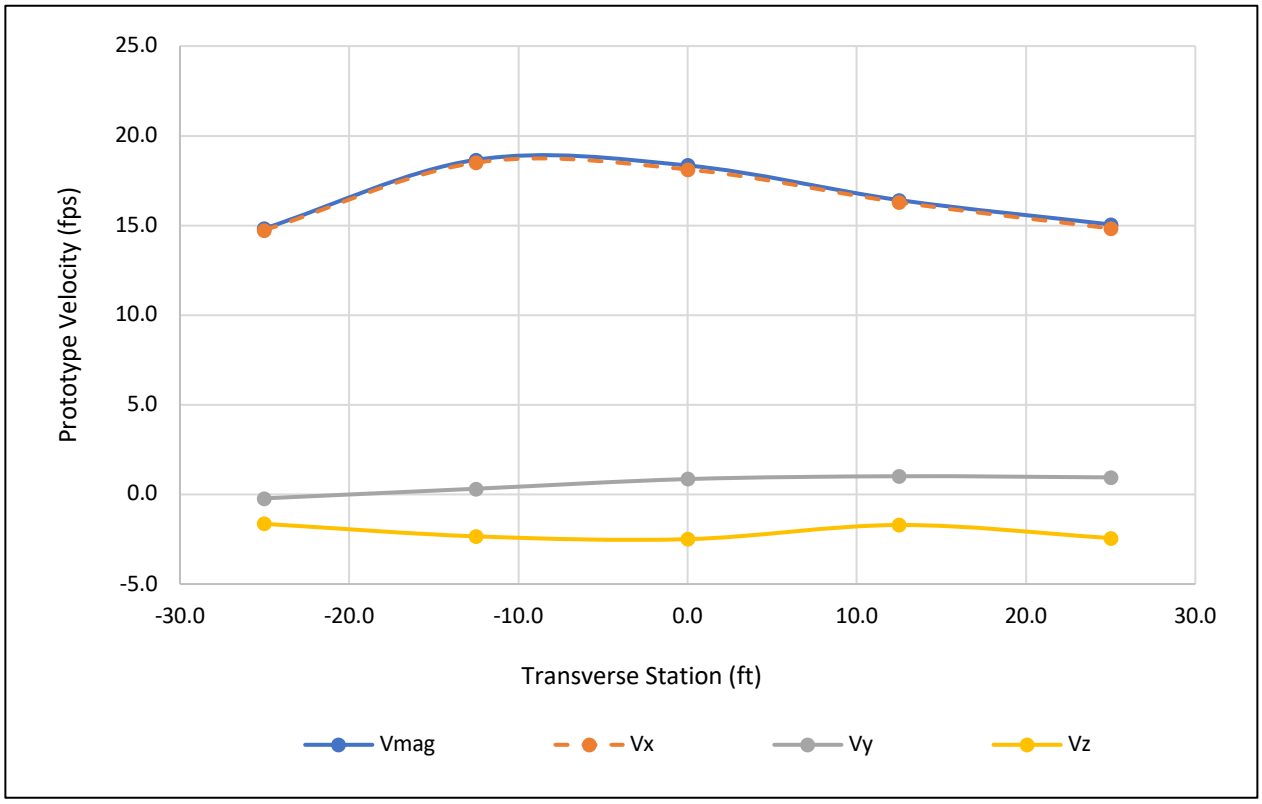

Fig. D6. Velocimeter results for System B, tangent wall configuration

APPENDIX E

Water Surface Profiles and Cross-Sections

System E, Smooth Walls

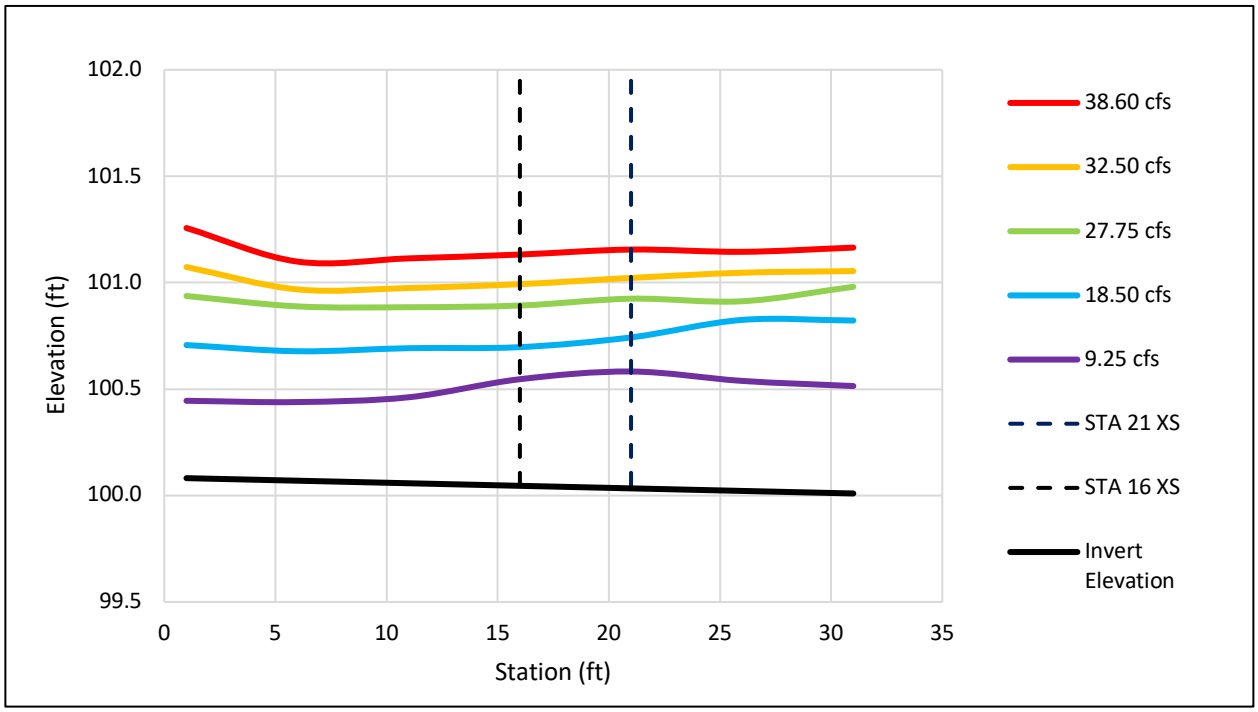

Fig. E1. Cross-sectioned averaged water surface profiles: System A, smooth wall configuration

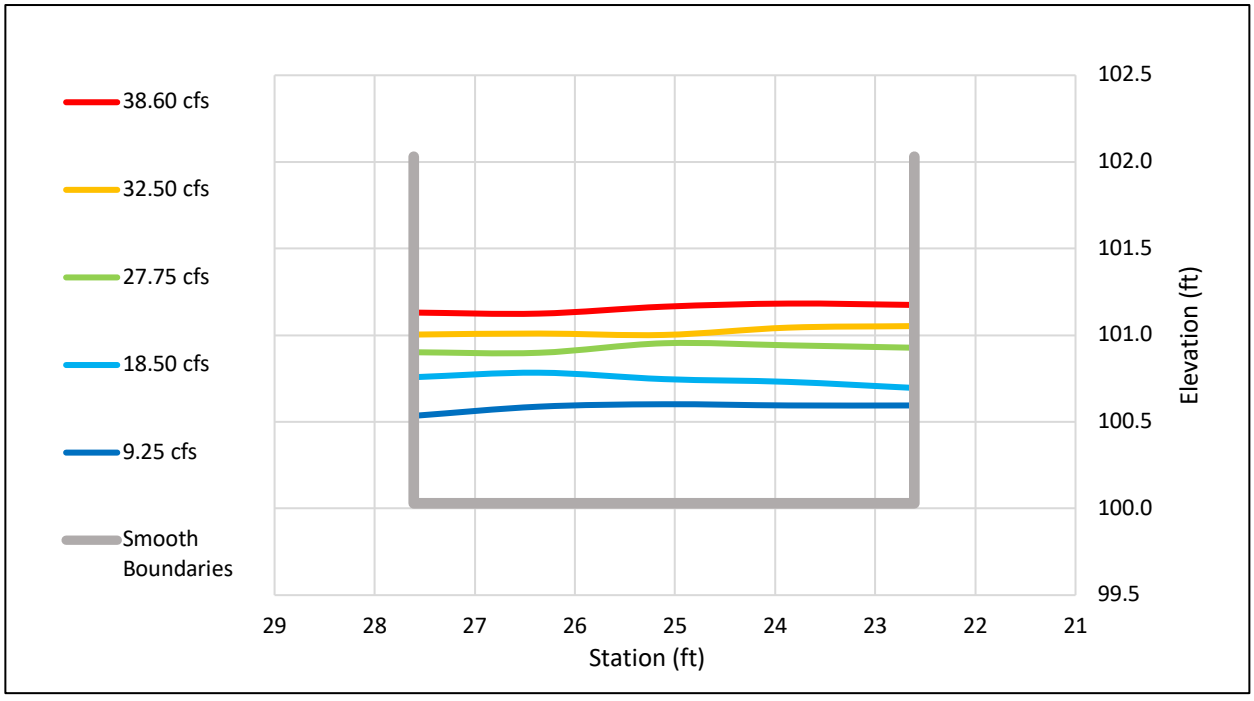

Fig. E2. STA 21 cross-section: System A, smooth wall configuration

System A, Mixed Walls

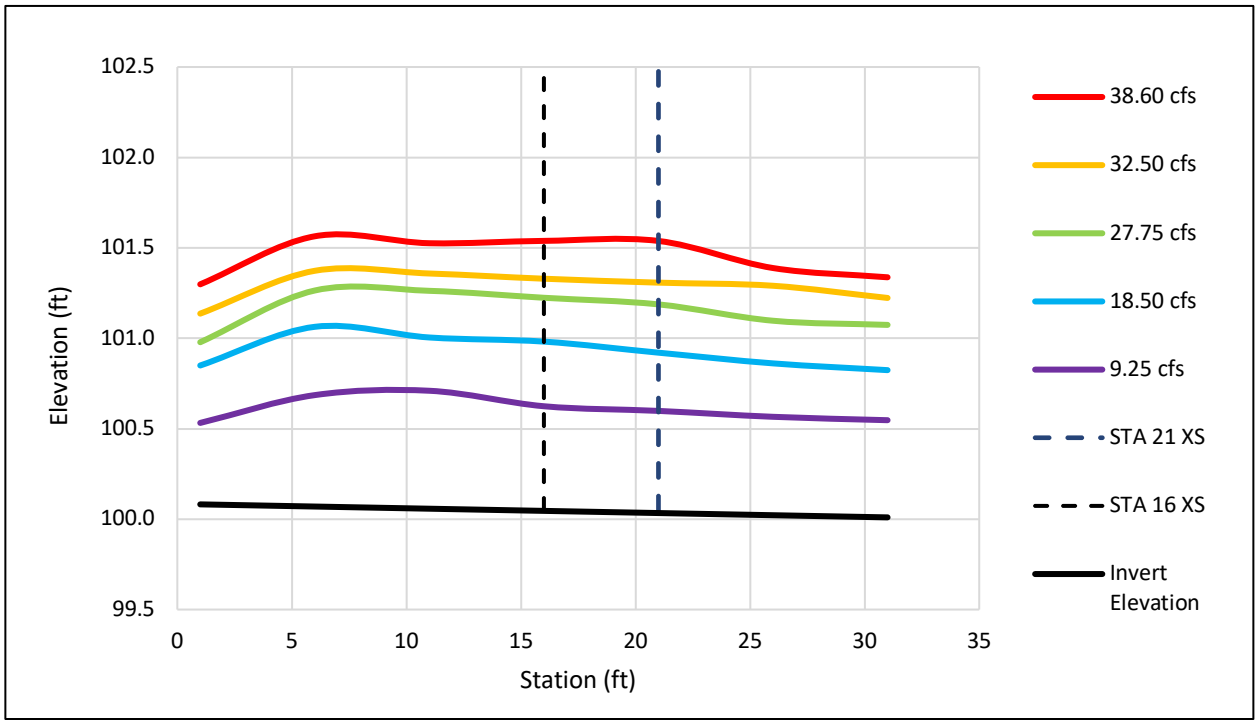

Fig. E3. Cross-sectioned averaged water surface profiles: System A, mixed wall configuration

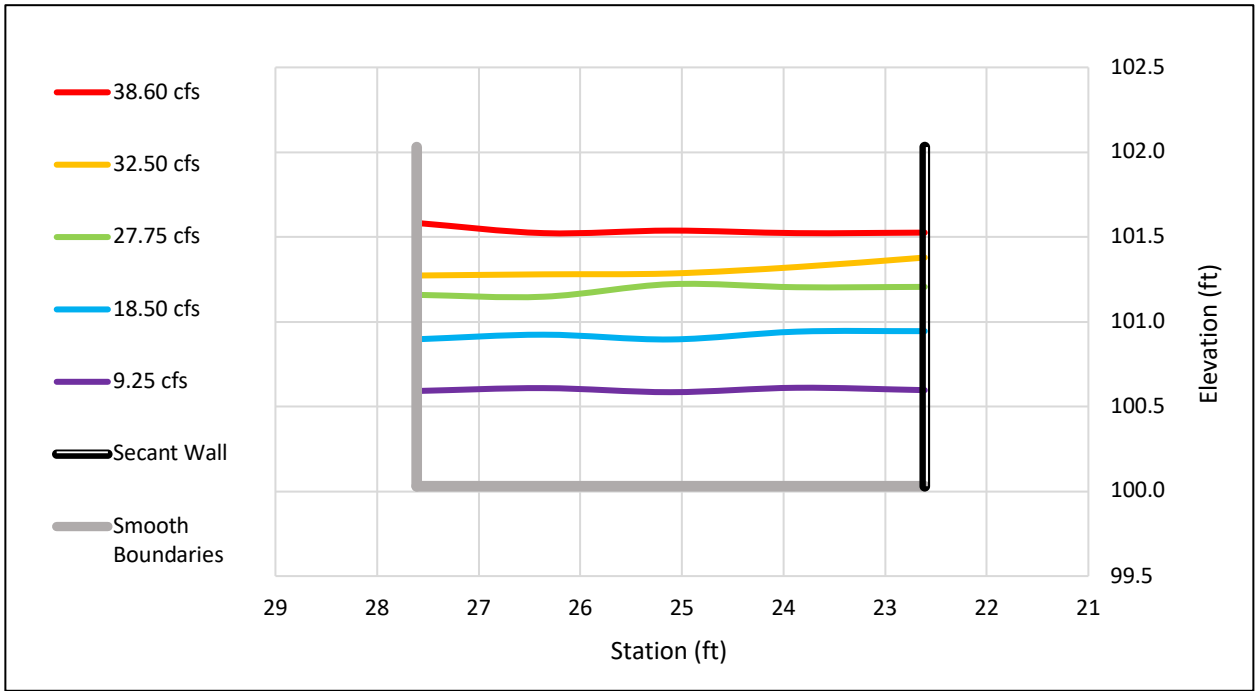

Fig. E4. STA 21 cross-section: System A, mixed wall configuration

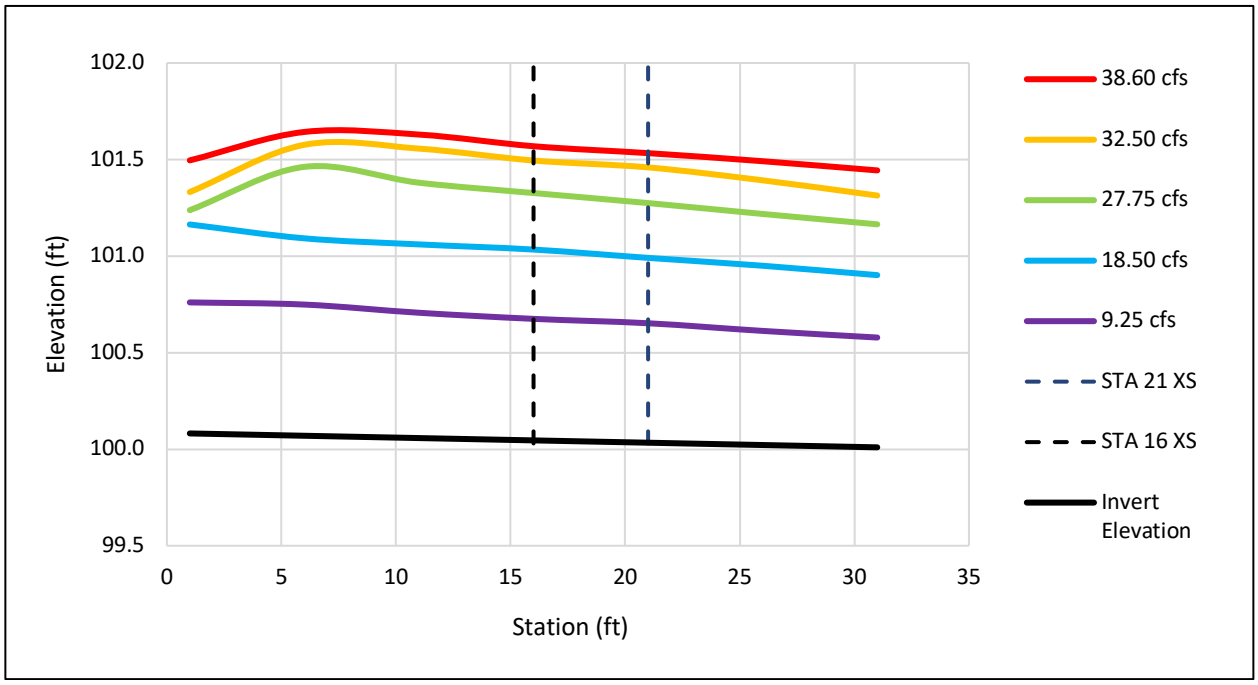

Fig. E5. Cross-sectioned averaged water surface profiles: System A, tangent wall configuration

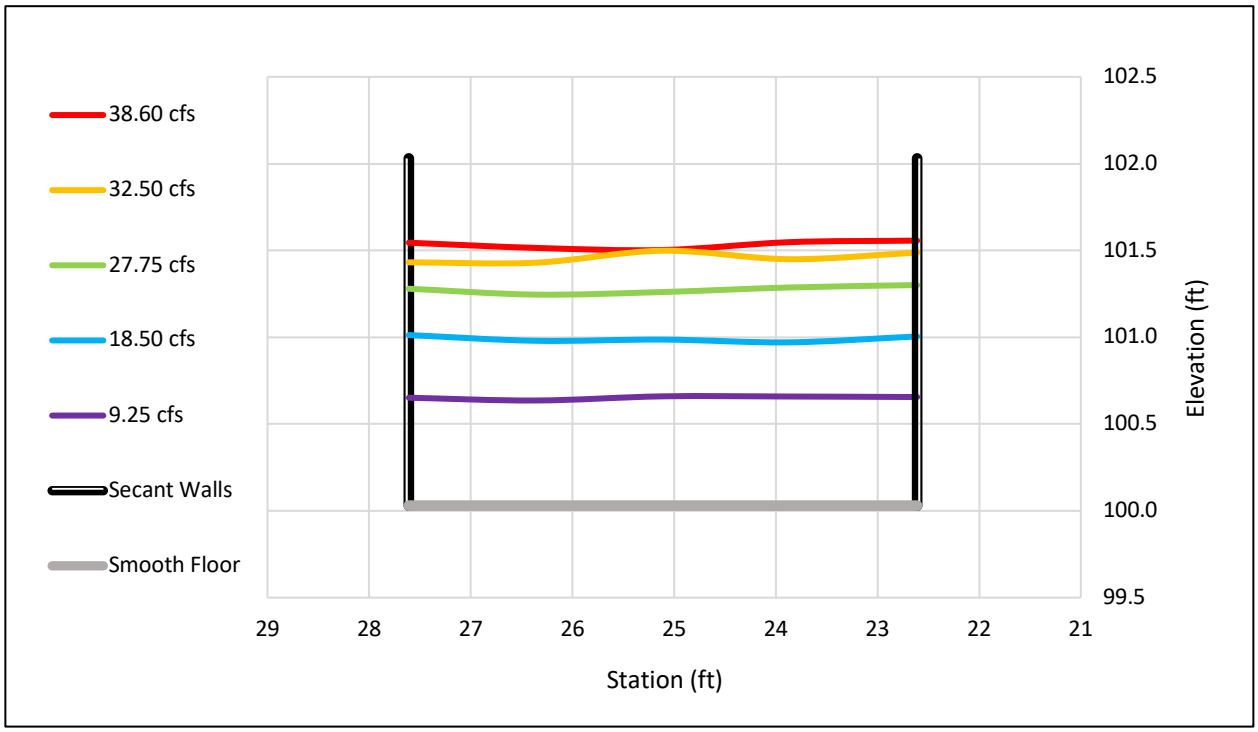

Fig. E6. STA 21 cross-section: System A, tangent wall configuration

System B, Smooth Walls

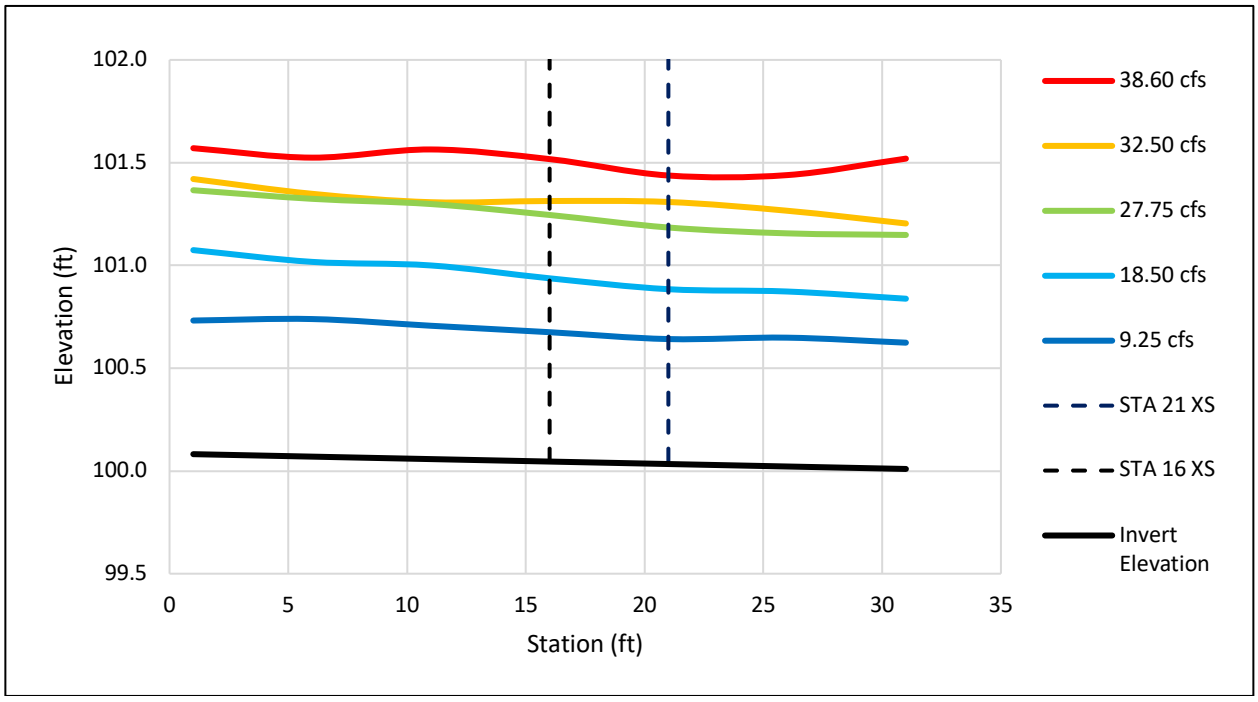

Fig. E7. Cross-sectioned averaged water surface profiles: System B, smooth wall configuration

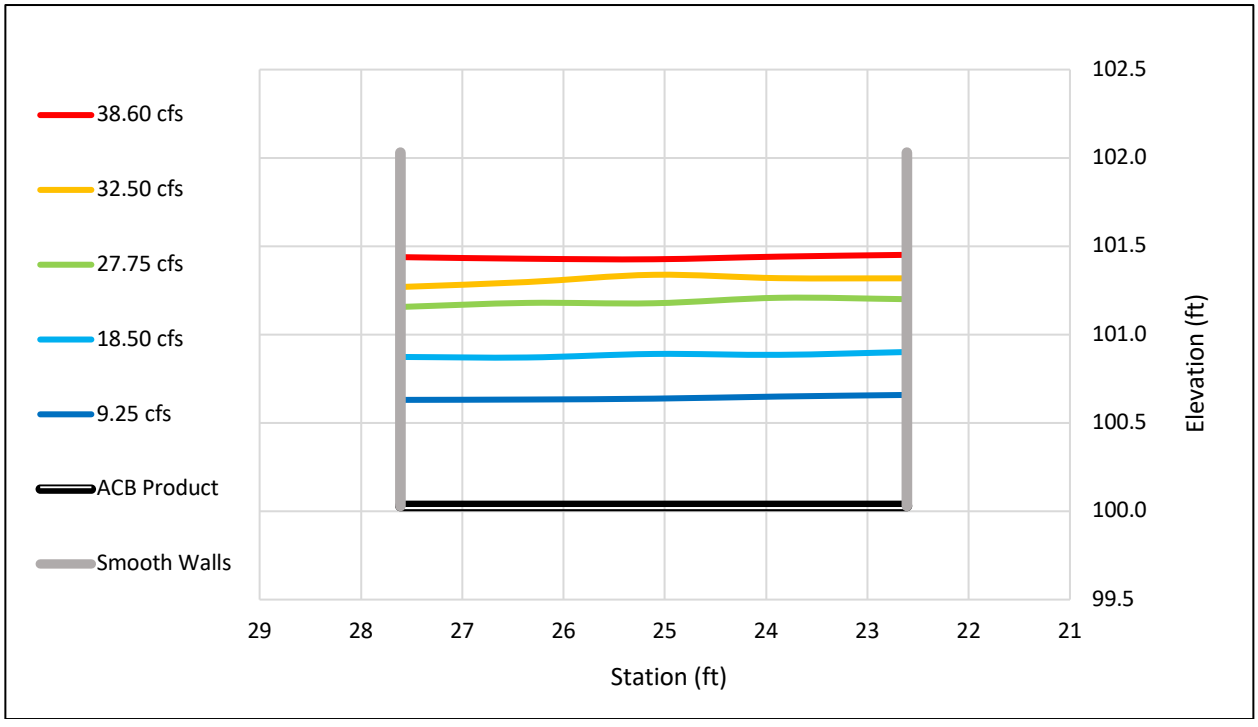

Fig. E8. STA 21 cross-section: System B, smooth wall configuration

System B, Mixed Walls

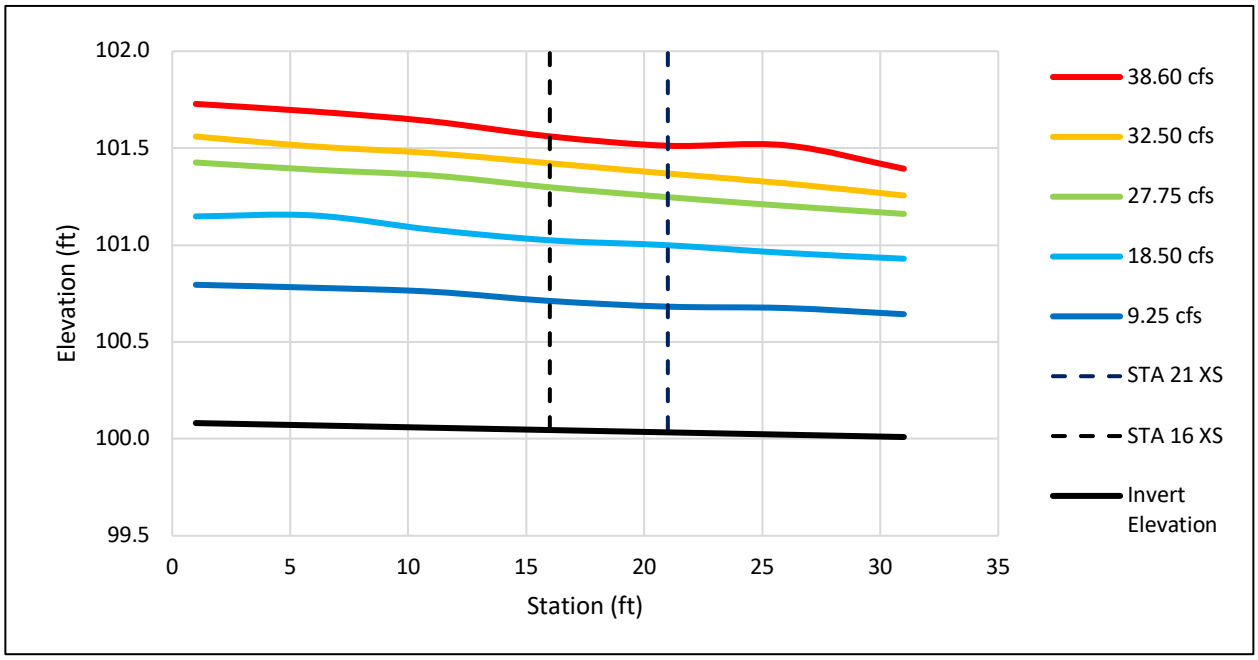

Fig. E9. Cross-sectioned averaged water surface profiles: System B, mixed wall configuration

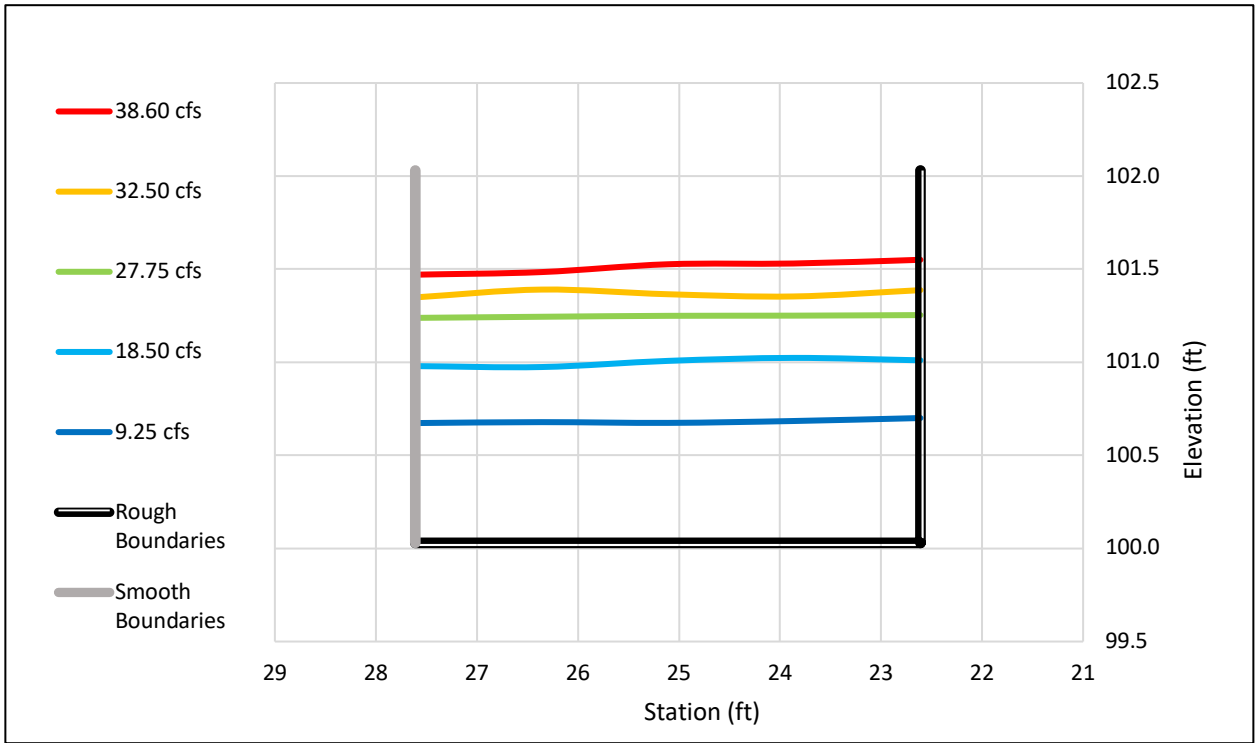

Fig. E10. STA 21 cross-section: System B, mixed wall configuration

System B, Tangent Walls

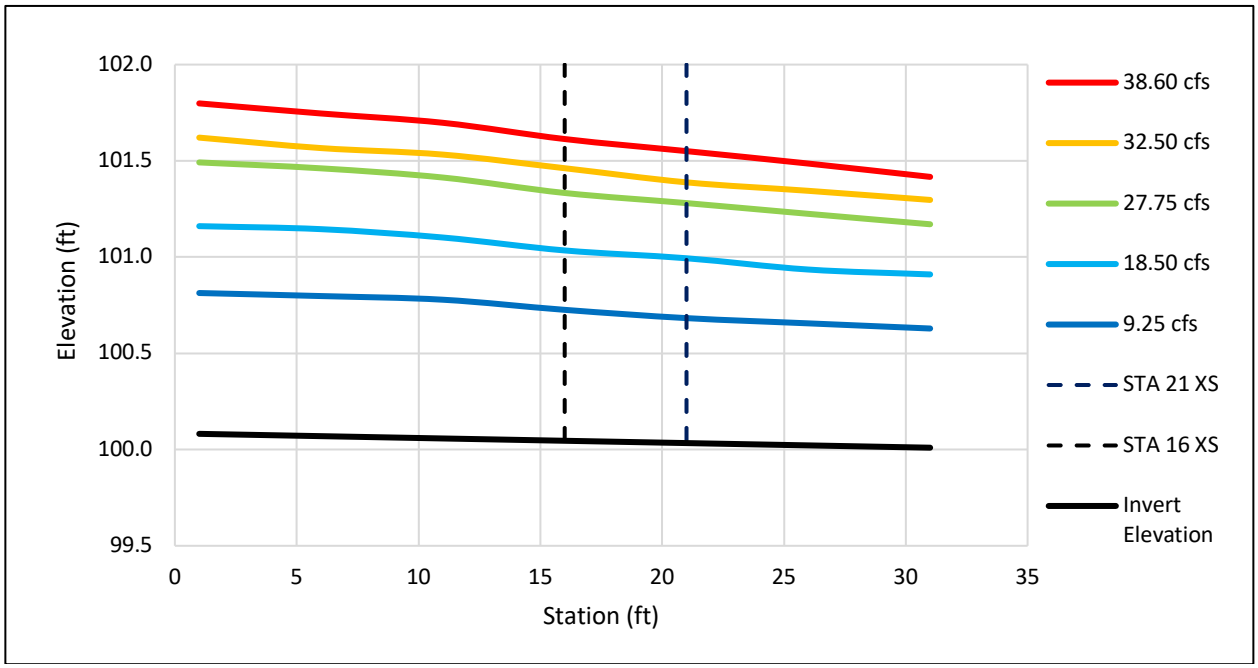

Fig. E11. Cross-sectioned averaged water surface profiles: System B, tangent wall configuration

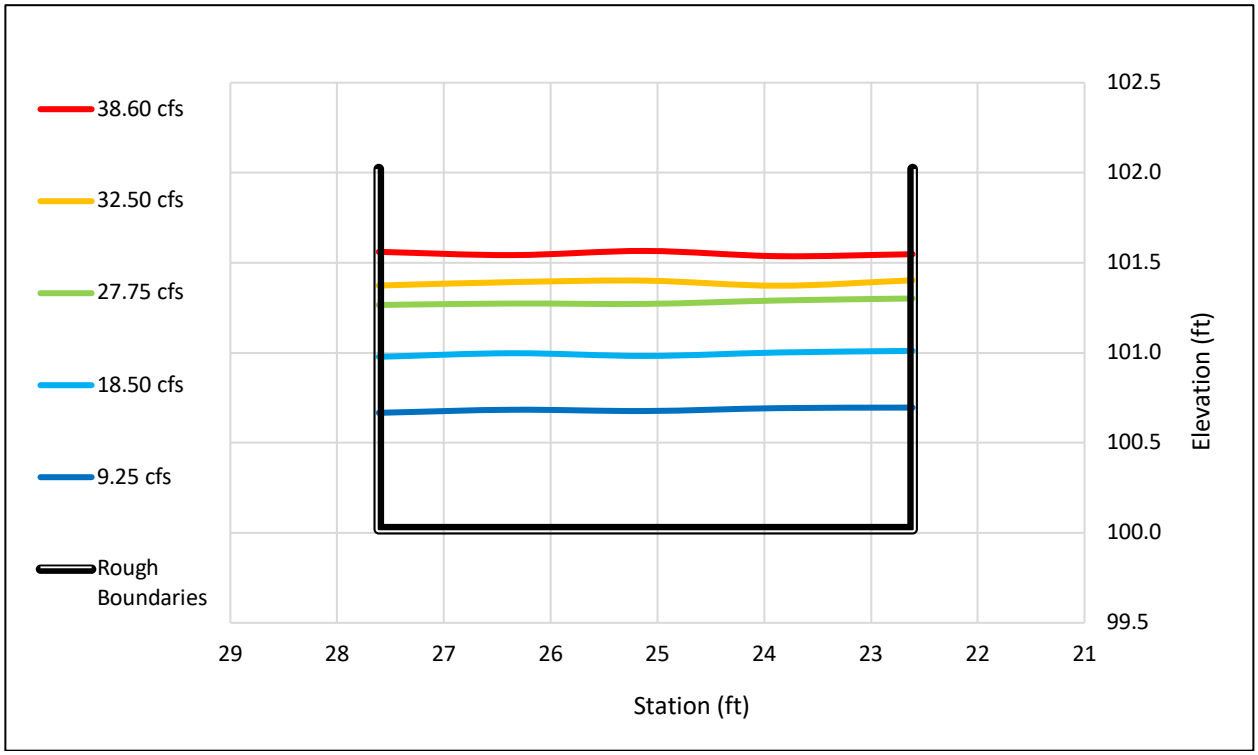

Fig. E12. STA 21 cross-section: System B, tangent wall configuration

System C, Smooth Walls

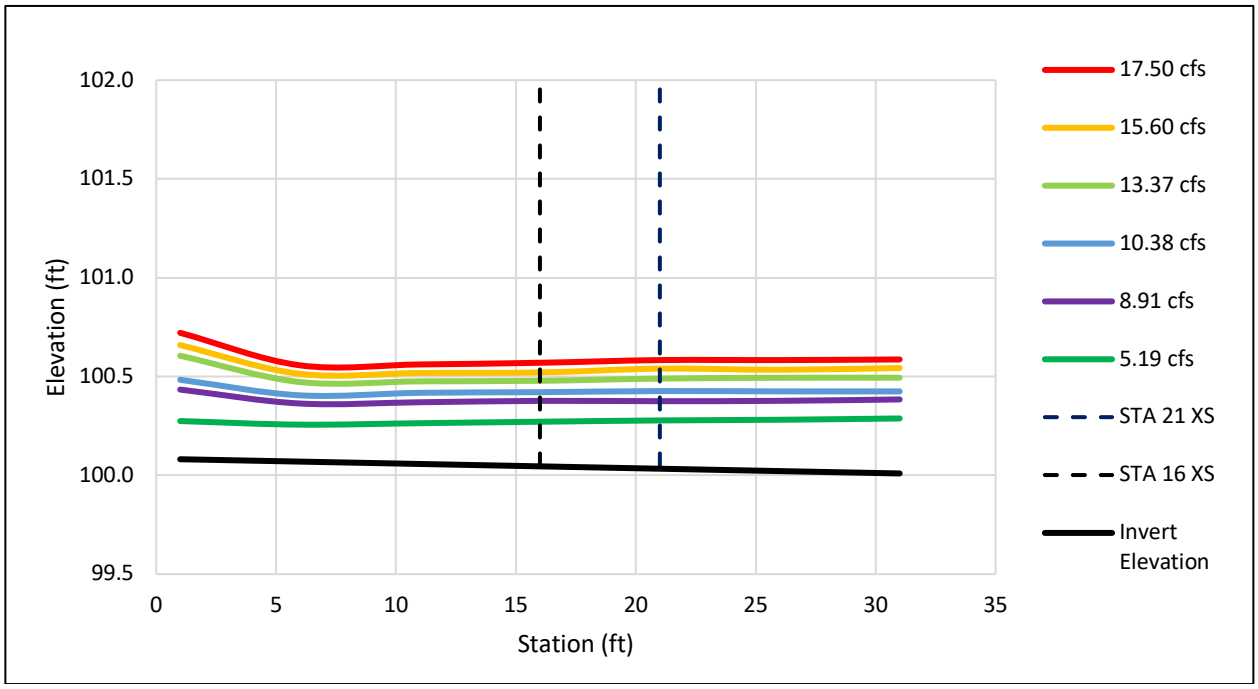

Fig. E13. Cross-sectioned averaged water surface profiles: System C, smooth wall configuration

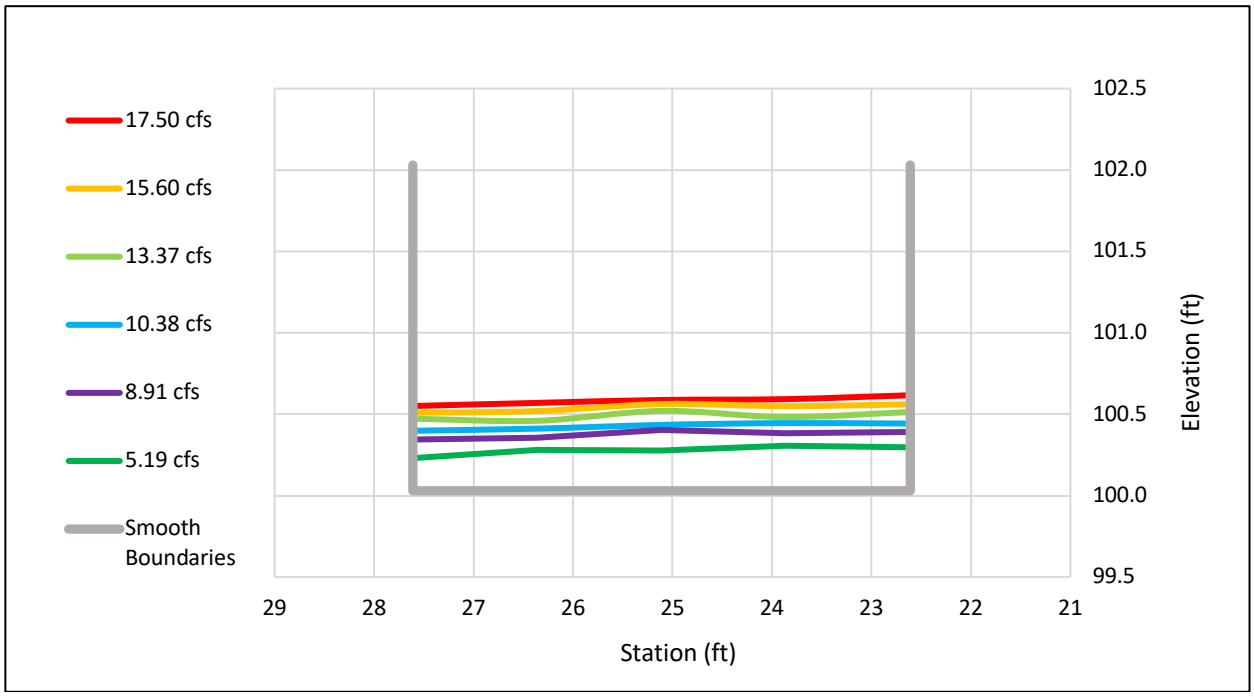

Fig. E14. STA 21 cross-section: System C, smooth wall configuration

System C, Mixed Walls

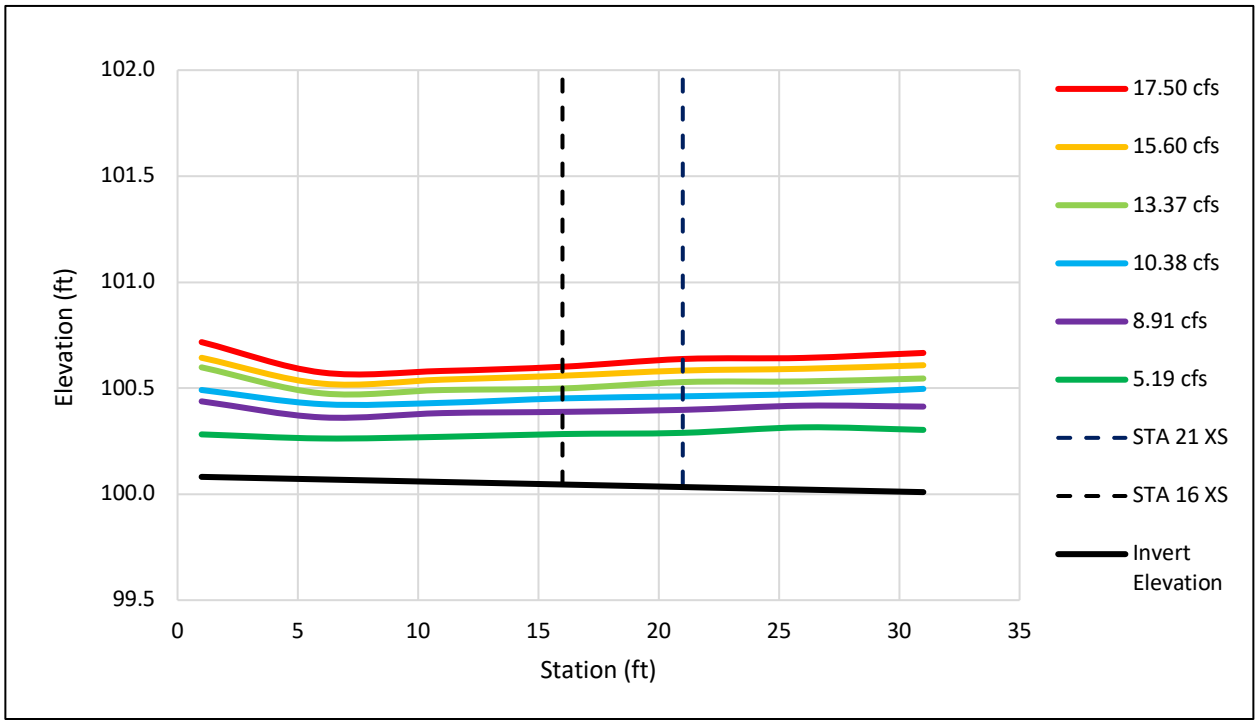

Fig. E15. Cross-sectioned averaged water surface profiles: System C, mixed wall configuration

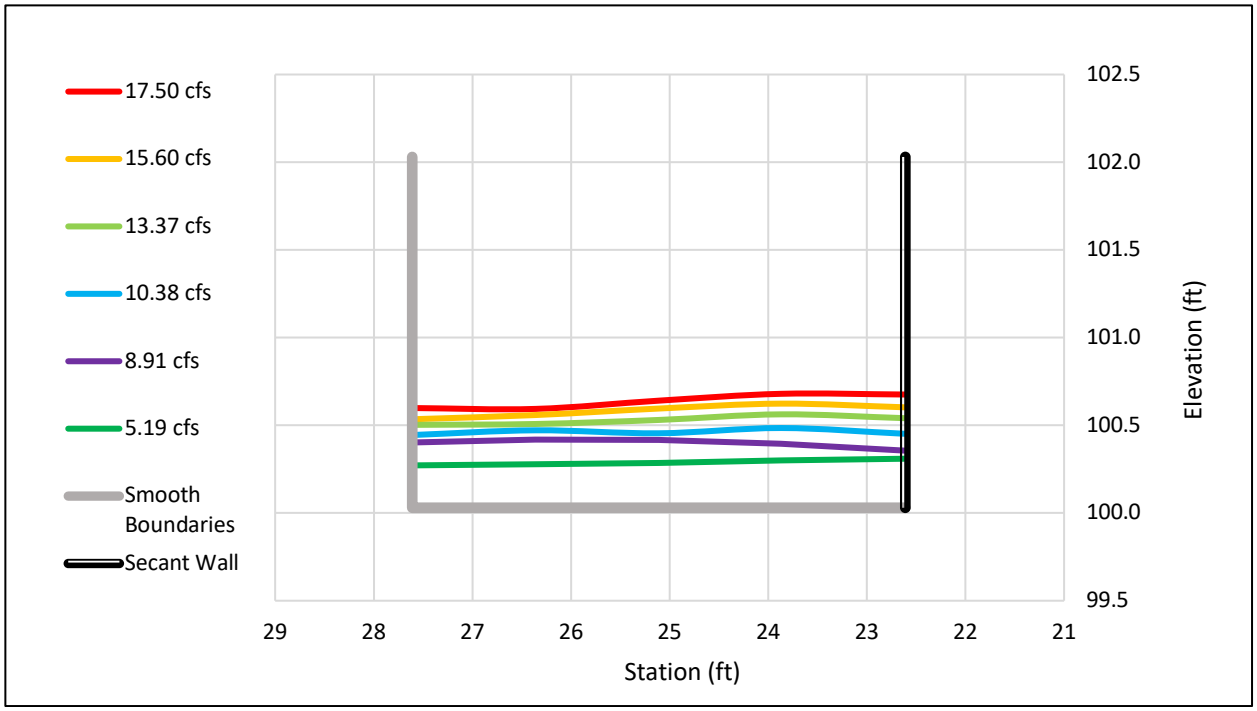

Fig. E16. STA 21 cross-section: System C, mixed wall configuration

System C, Tangent Walls

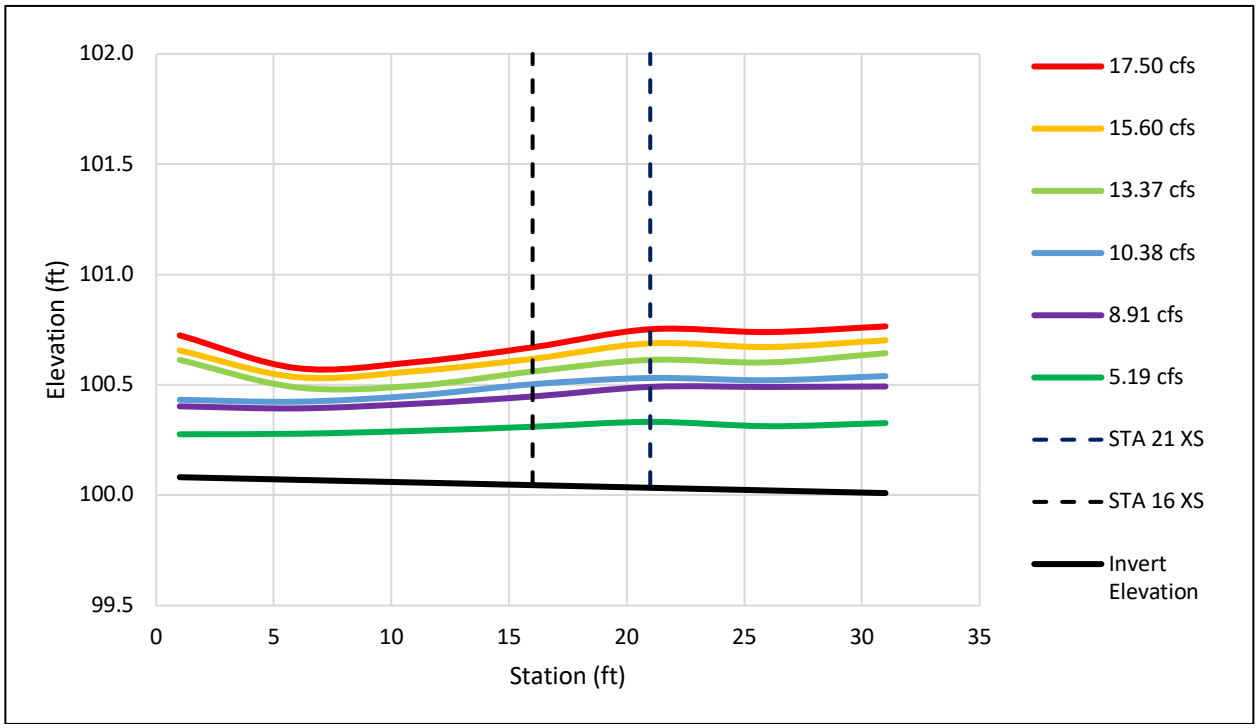

Fig. E17. Cross-sectioned averaged water surface profiles: System C, tangent wall configuration

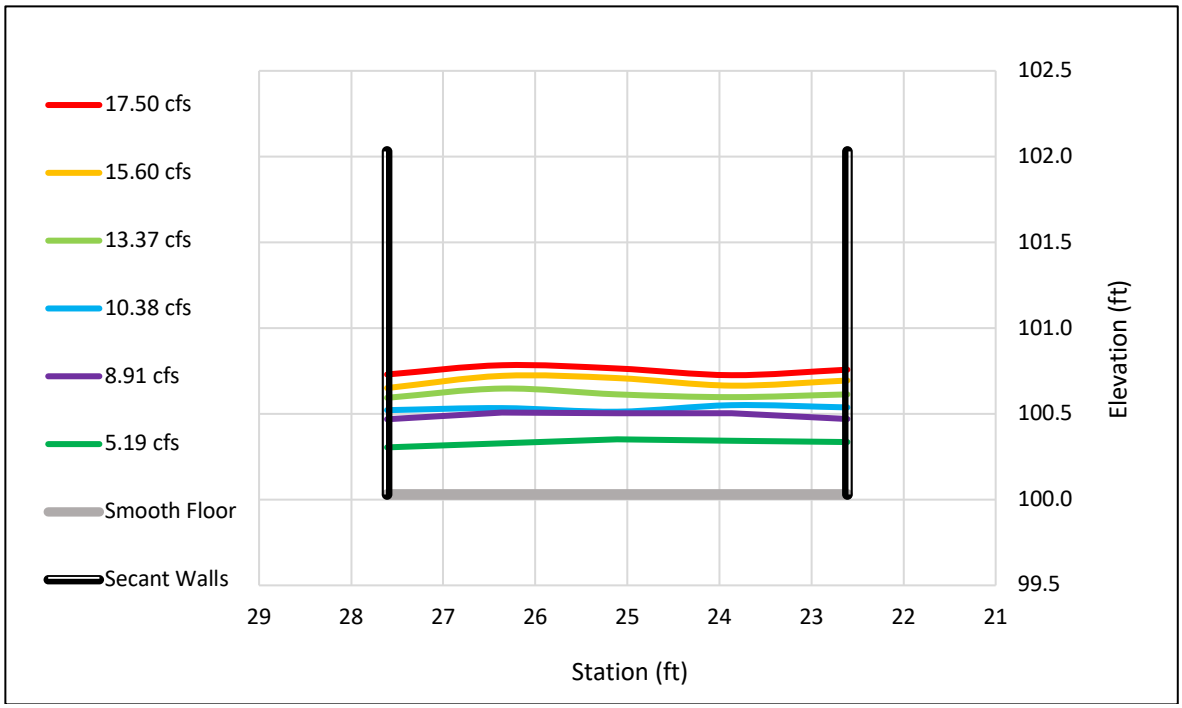

Fig. E18. STA 21 cross-section: System C, tangent wall configuration

System D, Smooth Walls

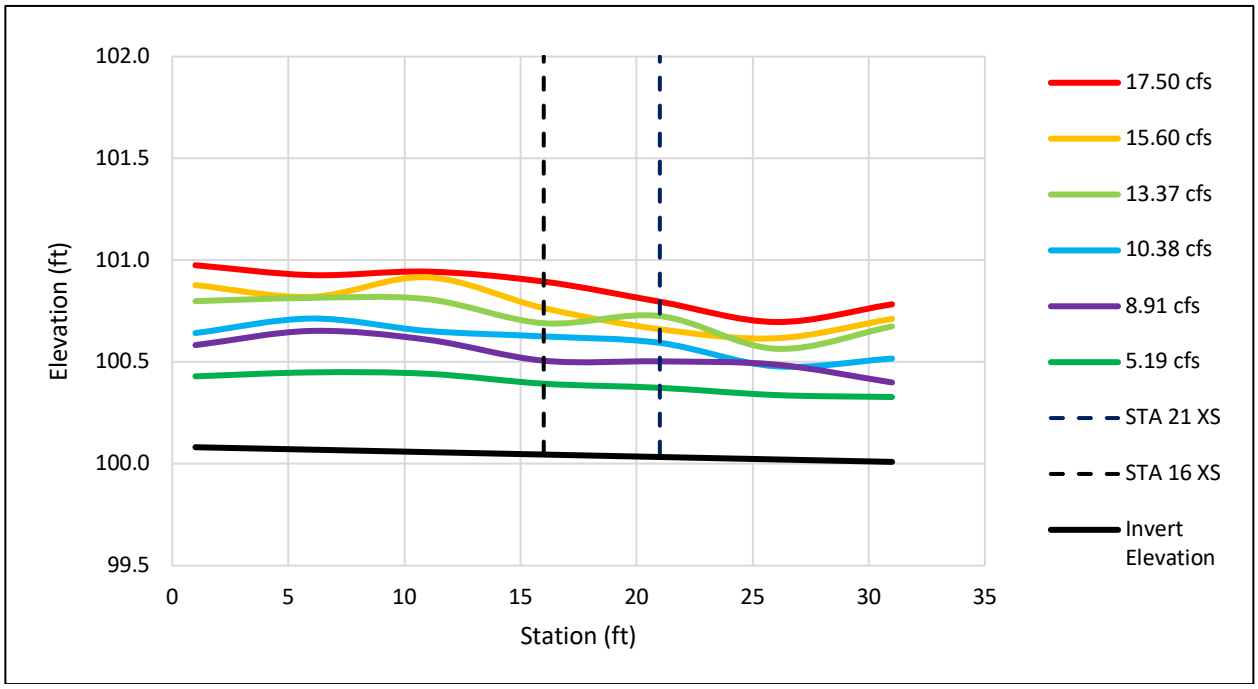

Fig. E19. Cross-sectioned averaged water surface profiles: System D, smooth wall configuration

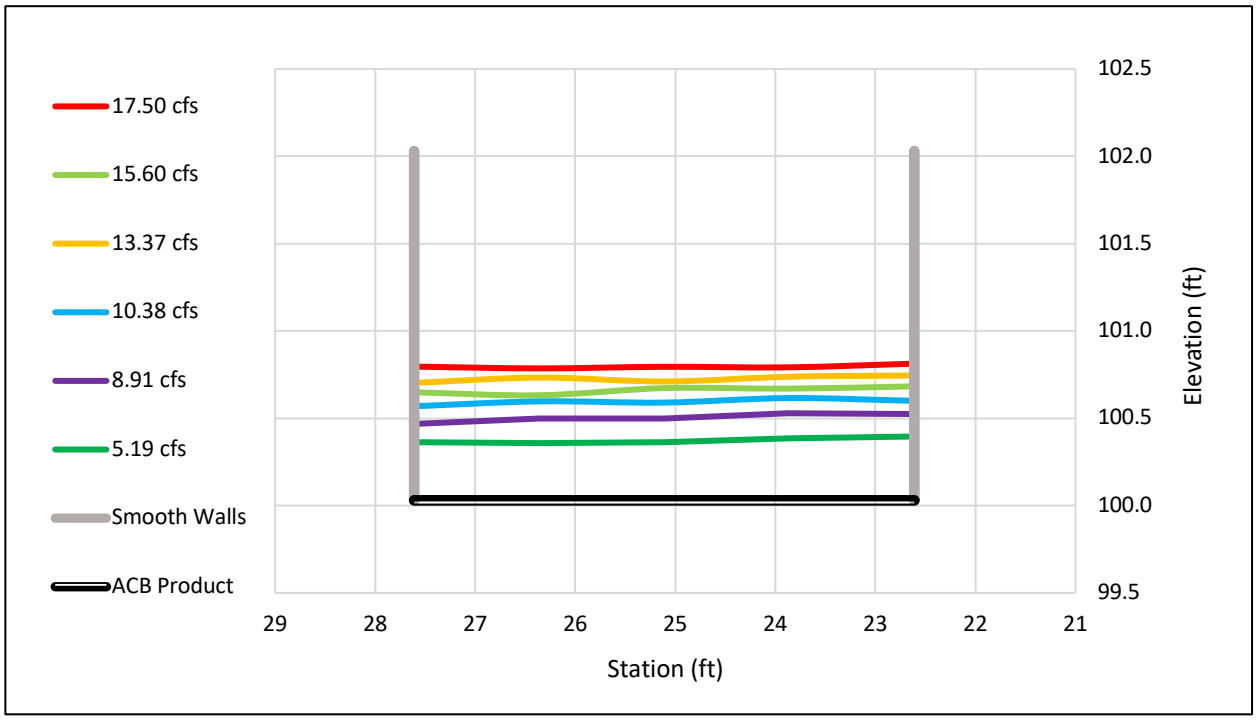

Fig. E20. STA 21 cross-section: System D, smooth wall configuration

System D, Mixed Walls

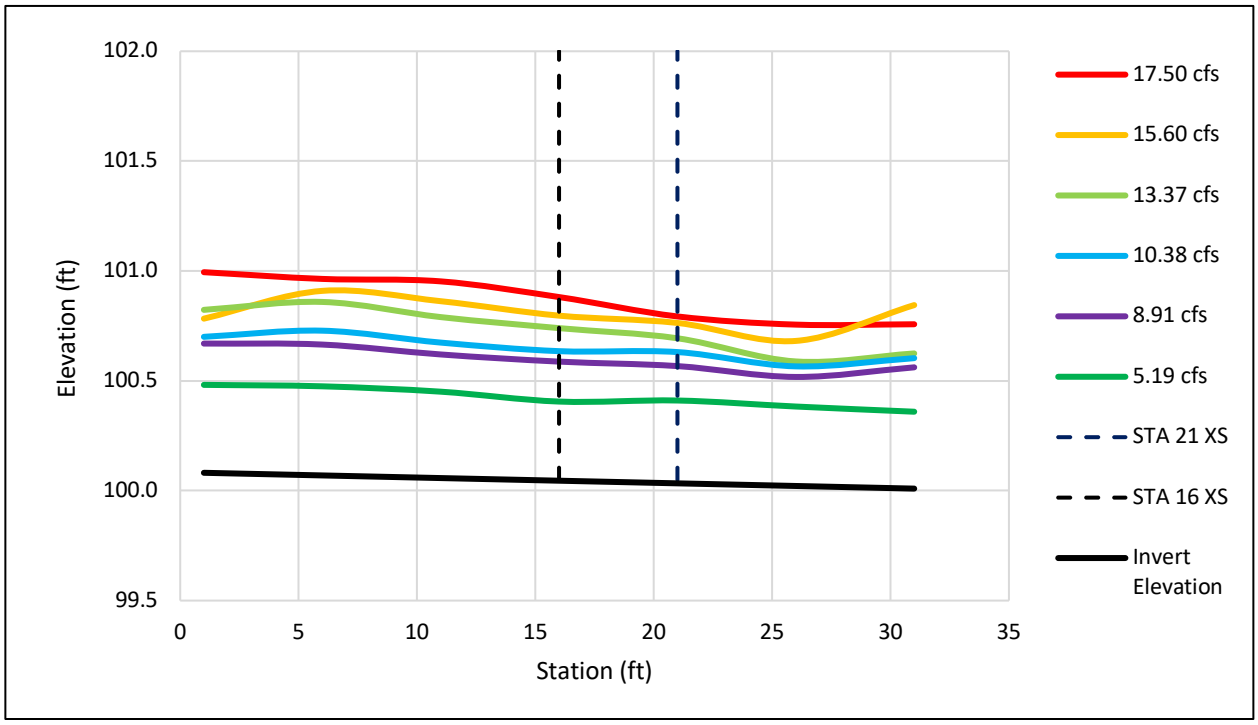

Fig. E21. Cross-sectioned averaged water surface profiles: System D, mixed wall configuration

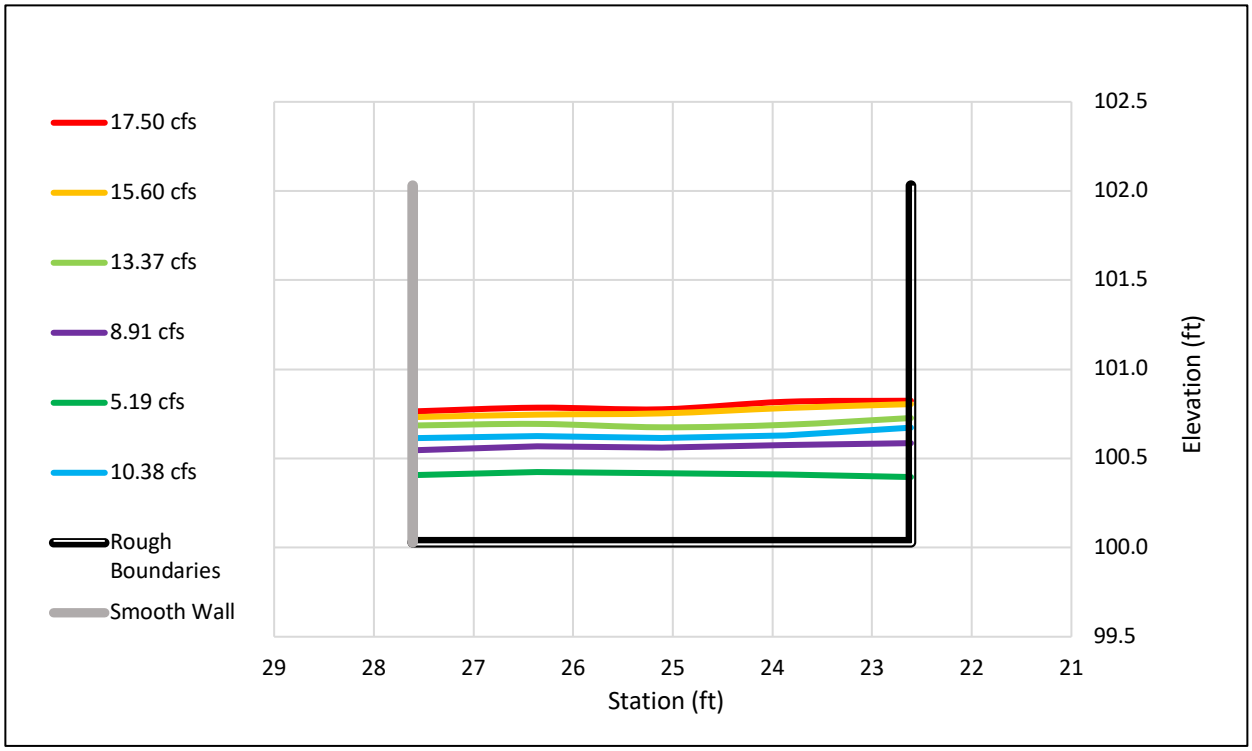

Fig. E22. STA 21 cross-section: System D, mixed wall configuration

System D, Tangent Walls

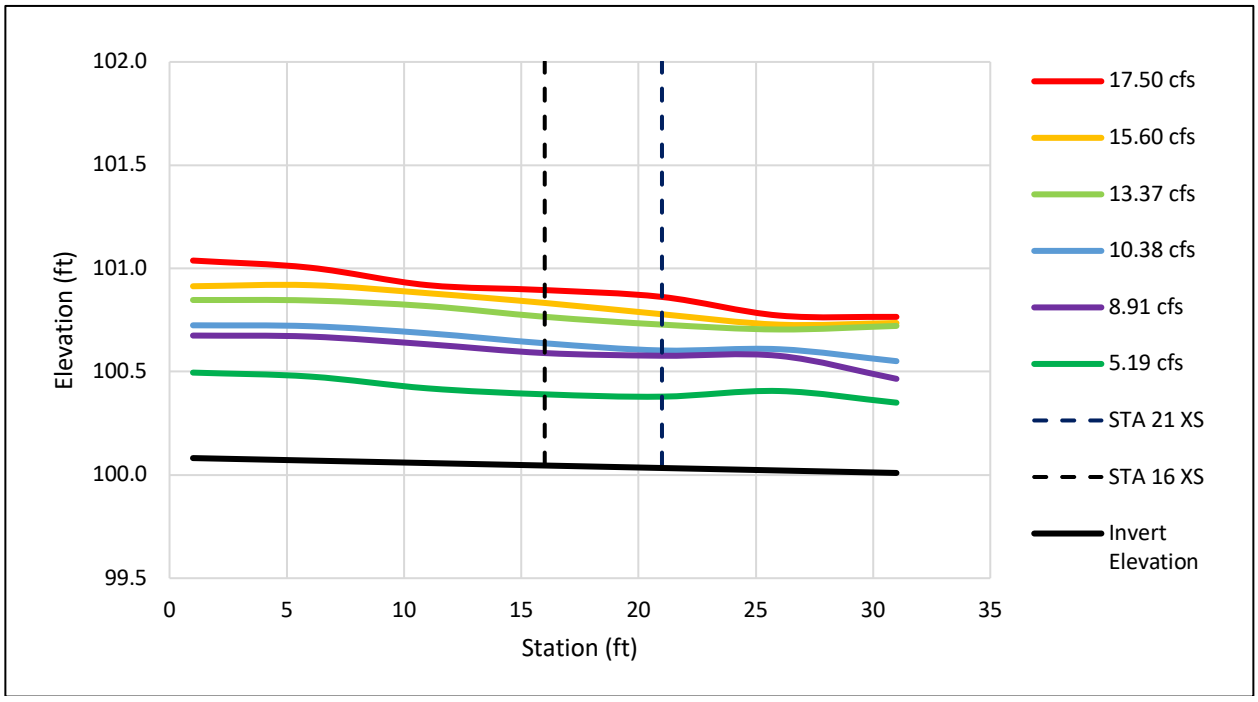

Fig. E23. Cross-sectioned averaged water surface profiles: System D, tangent wall configuration

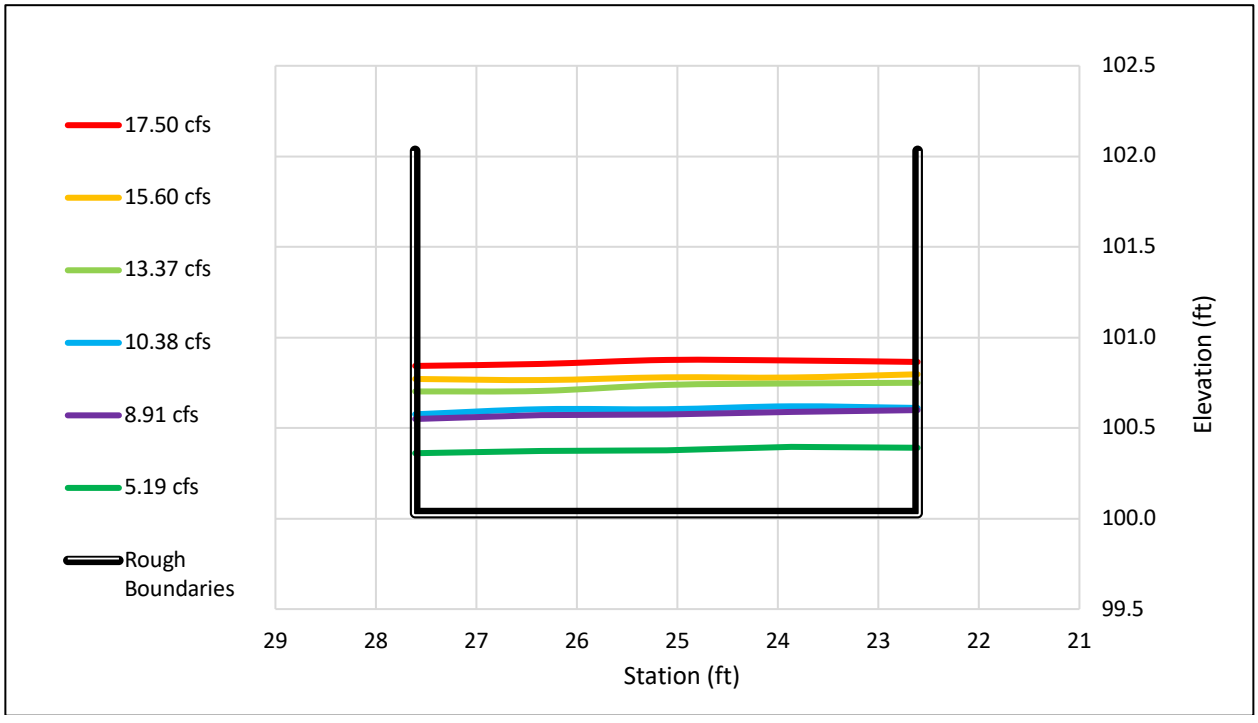

Fig. E24. STA 21 cross-section: System D, tangent wall configuration

LIST OF ABBREVIATIONS

ACB	Articulated concrete block
AECOM	Sub-contractor on the Rio Puerto Nuevo Project
AEP	Annual Exceedance Probability
ATHENA	ATHENA Engineering-Environmental, primary contractor on the Rio Puerto Nuevo Project
CFD	Computational fluid dynamics
CSU	Colorado State University's Hydraulics Laboratory
LTC	Channel left, the left side of the channel when looking downstream
M:P	ratio of model to prototype scales
NE	Northeast
RPN	The Rio Puerto Nuevo project
RTC	Channel right, the right side of the channel when looking downstream
SPS	Scour protection system
STA	Station number
SUFA	A scaled unit flowrate physical modeling approach
USACE	U.S. Army Corps of Engineers
WSE	Water-surface elevation